technische universität
dortmund

PhD Dissertation

Application-Specific Microwave Resonator Development:
Addressing the Challenges of Modern Electron Paramagnetic Resonance.

Jason W. Sidabras

Supervised by:
Prof. Dieter Suter: TU Dortmund
Prof. Wolfgang Lubitz: MPI-CEC

May 7, 2020

Abstract

Electron paramagnetic resonance (EPR) is a spectroscopic technique to study the interaction between free electrons and the local molecular environment. Over the past 60 years, EPR instrumentation and methodology has been developed to study, for example, the structure and dynamics of proteins, chemical reactions of organic-based radicals, transition-metal chemistry, catalytic reactions, electron transfer processes, and metallo-enzymes. Because of these past developments, EPR has become a powerful tool for chemists and physicists alike.

However, there remain several challenges in modern EPR that can be addressed by the development of application-specific microwave resonators. Three challenges are investigated: (i) improving the homogeneity of the magnetic flux density profile incident on a sample volume for applications to pulse EPR at Q-band frequencies (35 GHz); (ii) enhancing the sensitivity of EPR in the THz-bandgap (100 GHz to 1 THz frequency range; 3.34-33.36 cm^{-1} energy range) to improve the detection of thin films with the use of a resonant meta-materials; and (iii) improving the absolute sensitivity at X-band frequencies (9.5 GHz) for the study of protein single-crystals with volumes less than 85 nl. First, the introduction of a uniform field re-entrant TE_{01U} cavity at Q-band frequencies provides a 10 mm region-of-interest with a microwave field uniformity of 98%. The homogeneous field increases the microwave conversion factor by 60%. This design implements a waveguide H-type T-junction coupler with inductive obstacles to improve the coupling efficiency. The resonator is tested with a standard sample and shown to significantly improve the excitation profile for pulse EPR. Second, an investigation of the interaction between a split-ring resonator meta-material surface and a protein sample is presented as a way to increase the EPR signal for sub-THz frequencies. Data is collected using Frequency-Domain Fourier-Transform THz-EPR in the energy range of 11-18 cm^{-1}. The interaction of the EPR signal with a meta-material resonating at 14 cm^{-1} is modeled with a lumped-circuit transmission-line. It was found that both inductive and capacitive coupling is required to fully understand this complex system. From this analysis, a factor of 4 in the EPR signal is shown for an active sample height of 24 μm. Next, the absolute sensitivity at X-band frequencies has been increased up to a factor of 30 compared to commercial resonators by the implementation of a self-resonant micro-helix. This 0.4 mm inner diameter helix provides a resonator efficiency of 3.2 $mT/W^{1/2}$ corresponding to a $\pi/2$ pulse of 20 ns with an incident power of only 20 mW in a volume of 85 nl. This geometry is measured to have an absolute spin sensitivity of 64×10^6 Spins/G in 50 minutes of measurement time. Finally, the self-resonant micro-helix is used to obtain, for the first time, the angular dependence of the EPR signal from a protein single-crystal of [FeFe]-hydrogenase in the H_{ox} state from *Clostridium pasteurianum* (CpI) with a volume of 3 nL. A signal-to-noise ratio of 290 was achieved for 4.25×10^9 spins in 8 minutes of measurement time. Full g-tensor analysis was successfully performed and an orientation of the principal axes is discussed. With the excellent signal-to-noise ratio, data was also collected on the same protein crystal using an ESEEM/HYSCORE pulse sequence.

In total, this work pushes the state-of-the-art in EPR instrumentation allowing for new methodology development and broadening the applications available to chemists and physicists.

Zusammenfassung

Elektronenspinresonanz (ESR oder auch EPR) ist eine spektroskopische Technik zur Untersuchung der Wechselwirkung zwischen freien Elektronen und deren lokaler molekularer Umgebung. In den letzten 60 Jahren wurden EPR-Instrumente und -Methoden entwickelt, um beispielsweise die Struktur und Dynamik von Proteinen, chemische Reaktionen organischer Radikale, Übergangsmetallchemie, katalytische Reaktionen, Elektronentransferprozesse und Metalloenzyme zu untersuchen. Aufgrund dieser Entwicklungen hat sich die EPR zu einem leistungsstarken Werkzeug für Chemiker und Physiker entwickelt.

Jedoch verbleiben in der modernen EPR noch einige Herausforderungen, die durch die Entwicklung von anwendungsspezifischen Mikrowellenresonatoren adressiert werden können. In dieser Dissertation werden drei Herausforderungen adressiert: (i) Verbesserung der Homogenität des magnetischen Flussdichteprofils im Probenvolumen für Anwendungen mit gepulster EPR bei Q-Band-Frequenzen (35 GHz); (ii) Erhöhung der Empfindlichkeit in dem THz-Bandgap (100 GHz bis 1 THz Frequenzbereich; 3,34-33,36 cm^{-1} Energiebereich) zur Verbesserung der Detektion von dünnen Schichten unter Verwendung eines resonanten Metamaterials; und (iii) Verbesserung der absoluten Empfindlichkeit bei X-Band-Frequenzen (9,5 GHz) für die Untersuchung von Protein-Einkristallen mit Volumina unter 30 nl. Die Einführung eines homogenen Feld "re-entrant" TE_{01U} Resonators für Q-Band-Frequenzen bietet einen 10 mm Bereich mit einer Mikrowellenfelduniformität von 98%. Das homogene Feld erhöht den Mikrowellenkonversionsfaktor um 60%. Dieses Design verwendet einen H-Typ Wellenleiter mit einem T-Übergangskoppler mit induktiven Störungen um die Kopplungseffizienz zu verbessern. Der Resonator wurde mit einer Standardprobe getestet und zeigt eine signifikante Verbesserung des Anregungsprofiles für gepulste EPR. Zweitens wurde eine Untersuchung der Wechselwirkung zwischen der Meta-Materialoberfläche eines Spaltringresonators und einer Proteinprobe als Möglichkeit zur Erhöhung des EPR-Signals für Sub-THz-Frequenzen vorgestellt. Die Daten wurden mit Hilfe von Fourier-transformierter THz-EPR in der Frequenzdomäne im Energiebereich von 11-18 cm^{-1} gesammelt. Die Wechselwirkung zwischen dem EPR-Signal und einem Metamaterial mit einer Resonanz bei 14 cm^{-1}, wird mit einer lumped-circuit transmission-line modelliert. Es wurde festgestellt, dass für das vollständige Verständnis dieses komplexen Systems sowohl eine induktive als auch eine kapazitive Kopplung erforderlich ist. Bei einer Probenhöhe von 24 μm wurde eine Verbesserung des EPR-Signals um den Faktor 4 erreicht. Anschließend wurde die absolute Empfindlichkeit bei X-Band-Frequenzen gegenüber kommerziellen Resonatoren durch die Implementierung einer selbstresonanten Mikrohelix um den Faktor 30 erhöht. Diese Helix mit einem 0,4 mm Innendurchmesser bietet einen Resonatorwirkungsgrad von 3,2 $mT/W^{1/2}$, was einem 20 ns $\pi/2$-Puls bei einer Leistung von nur 20 mW bei einem Volumen von 85 nl entspricht. Schließlich konnte mit dieser selbstresonanten Mikrohelix erstmals die Winkelabhängigkeit des EPR-Signals eines Proteineinkristalls der [FeFe]-Hydrogenase im H_{ox} Zustand aus *Clostridium pasteurianum* (CpI) mit einem Volumen von 3 nL erhalten werden. Eine vollständige g-Tensoranalyse wurde erfolgreich durchgeführt und die Orientierung der Hauptachsen ermittelt. Mit dem ausgezeichneten Signal-Rausch-Verhältnis wurden auch Daten mit ESEEM/HYSCORE-Pulssequenzen an demselben Proteineinkristall gesammelt.

Insgesamt bringt diese Arbeit den Stand der Technik in der EPR-Instrumentierung voran, was die Entwicklung neuer Methoden und eine Erweiterung der Anwendungen in Chemie und Physik ermöglicht.

Acknowledgements

This work could not have been realized without the many people who have given me their support, mentorship, and guidance throughout this adventure. I would first like to thank Prof. Wolfgang Lubitz for his mentorship and invitation to the Max Planck Institute for Chemical Energy Conversion. This opportunity has been personally and professionally energizing; from the studying of single-crystals of enzymes to adventures in Europe. I would like to thank Prof. Dieter Suter for being my promoter and supervisor at TU Dortmund. This has been a very fruitful collaboration and I look forward to working together in the future. I would like to also thank Dr. Edward J. Reijerse for his supervision and our many discussions. His input to this work has been invaluable. Finally, I would like to thank Dr. Alexander Schnegg for his mentorship and the EPR Research Group for countless discussions. I would especially like to thank Markus Teucher for help with the German translation of my abstract.

This work has been funded by the Horizon 2020 Marie Skłodowska-Curie Actions Fellowship (ActEPR; Grant No. 745702) and the Max Planck Institute.

I would like to thank the following people for their various contributions to this body of work.

- Chapter 3:
  - Stephan Syring and Udo Klar at the Max Planck Institute for Chemical Energy Conversion and Sebastian Planckert at Max Planck Institute for Kohlenforschung for their skillful manufacturing.
- Chapter 4:
  - Dr. Ryszard Narkowicz for the initial design and optimization of the SRR geometries.
  - Anatoly Firsov for fabricating the the SRRs geometry using an electron microscope at Helmholtz-Zentrum Berlin.
  - Drs. Joscha Nehrkorn and Karsten Holldack for performing the FD-FT THz experiments.
- Chapters 5 and 6:
  - Within the group of Prof. Thomas Happe, Drs. Jifu Duan and Martin Winkler for growing [FeFe]-hydrogenase crystals from *Clostridium pasteurianum* (CpI) in the H_{ox} state.
  - Within the group of Prof. Athina Zouni, Dr. Rana Hussein for growing the photosystem II complex crystals from *Thermosynechococcus elongatus*.
  - Dr. Maria Chrysina from the Max Planck Institute for Chemical Energy Conversion for guidance on photosystem II spectra.
  - Michael Reus for the photosystem II BBY particles sample and the UV-VIS measurements.

Of course, none of this would be possible without the support of my family throughout my academic career. I give my undying gratitude to my wife, Emily, who has kept me grounded while providing a loving home. And to my daughter, Juniper, who's smile and curiosity inspires me to push further.

List of Publications

Scientific Publications resulting from this work:
See Appendix A for full *Curriculum Vitae*.

1. **J. W. Sidabras**, T. Sarna, R. R. Mett, J. S. Hyde, *Uniform field loop-gap resonator and rectangular TE_{U02} for aqueous sample EPR at 94 GHz*, J. Magn. Reson. 282 (2017) 129–135.
2. **J. W. Sidabras**, E. J. Reijerse, W. Lubitz, *Uniform field re-entrant cylindrical TE_{01U} cavity for pulse electron paramagnetic resonance spectroscopy at Q-band*, Appl. Magn. Reson. 48 (11) (2017) 1301–1314.
3. J. S. Hyde, **J. W. Sidabras**, R. R. Mett, *Uniform field resonators for EPR spectroscopy: A review*, Cell Biochem. Biophys. 76 (1-2) (2018) 1–12.
4. **J. W. Sidabras**, J. Duan, M. Winkler, T. Happe, R. Hussein, A. Zouni, D. Suter, A. Schnegg, W. Lubitz, E. J. Reijerse, *Improving Electron Paramagnetic Resonance Sensitivity for nano-Liter Volume Single-Crystals Using a Self-Resonant micro-Helix.*, Sci. Adv., 10 (5) (2019), eaay1394.

Contents

List of Figures

List of Tables

Acronyms

Acronym	Description
Experiments:	
EPR	electron paramagnetic resonance
CW	continuous wave
ESE	electron spin echo
ESEEM	electron spin echo envelope modulation
HYSCORE	hyperfine sub-level correlation
NARS	non-adiabatic rapid scan
RS	rapid scan
ELDOR	electron-electron double resonance
EDNMR	ELDOR-detected nuclear magnetic resonance
ENDOR	electron nuclear double resonance
Units:	
GHz	10^9 Hz
G	Gauss
mT	miliTessla (10 G)
V	Volt
A/m	Ampere per meter
mW	10^{-3} Watt
Resonators:	
$\mathbf{H}_1$	microwave magnetic field; $\mathbf{H}_1 = \mathbf{H}e^{-i\omega t}$
$\mathbf{B}_0$	static magnetic field; $\mathbf{B}_0 = \mu_0\mathbf{H}_0$
$\mathbf{B}_1$	microwave magnetic flux density; $\mathbf{B}_1 = \mu_0(\mathbf{M}_0 + \mathbf{H}_1)$
ϵ_0	free-space permittivity; 8.854×10^{-12} Farad per meter
ϵ_r	dielectric permittivity; $\epsilon = \epsilon_0\epsilon_r$; $\epsilon_r = \epsilon_r' + i\epsilon_r''$
μ_0	free-space permeability; $4\pi \times 10^{-7}$ Henry per meter
μ_r	dielectric permeability; $\mu = \mu_0\mu_r$; $\mu_r = 1 + M$
$\mathbf{M}_0$	time-varying magnetic suceptibility vector; $M = \lvert\mathbf{M}_0\rvert$
X-band	8-12 GHz; 9.5 GHz nominal
Q-band	27-40 GHz; 34 GHz nominal
W-band	75–110 GHz; 94 GHz nominal
UF	uniform field
LGR	loop-gap resonator
TE	transverse electric
TEM	transverse electric and magnetic; plane wave
SRR	split-ring resonator
SRRs	split-ring resonator array
PMR	planar micro-resonator
AWG	arbitrary-waveform generator
Samples:	
BDPA	α,γ-bisdiphenylene-β-phenylallyl
PS	polystyrene
LiPC	lithium phthalocyanine
CpI	[FeFe]-hydrogenase from *Clostridium pasteurianum*
BBY particles	Berthold, Babcock, and Yocum sample preparation (Ref. 5.23)
$Y_D^\bullet$	photosystem II tyrosine D radical

1. Introduction

Electron paramagnetic resonance (EPR) is a spectroscopic technique to probe the interactions of unpaired electrons to the surrounding molecular environment. EPR has been employed to gain information on, for example, the structure and dynamics of proteins, organic-based radicals, transition metals, radical reactions, electron transfer processes, and metallo-enzymes. As a magnetic resonance technique, EPR requires an incident microwave magnetic field perpendicular to a static magnetic field.[1.1] Sensitivity is greatly enhanced by the use of microwave cavities, where the sample can be placed in a region of strong microwave magnetic field while minimizing electric field losses as illustrated in Fig. 1.1. These resonators have been developed to be general-purpose and are commercially available. However, many opportunities exist in instrumentation development for improvement to the quality of EPR data and to extend the applicability of EPR to samples that cannot currently be studied.

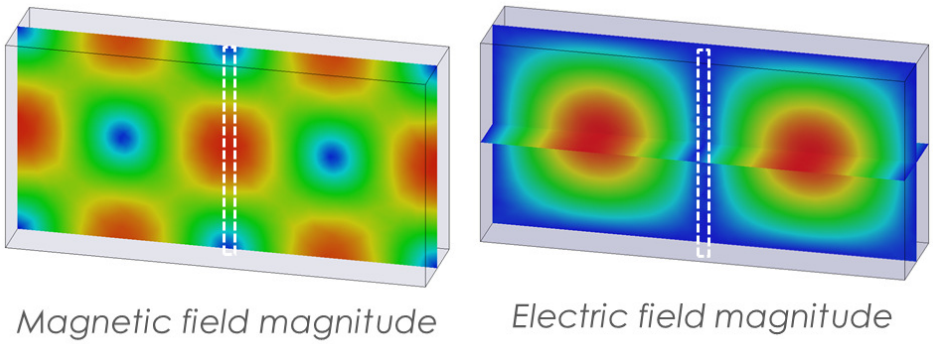

Figure 1.1.: The electric and magnetic field is shown for a standard TE_{102} rectangular cavity. The placement of the sample is indicated by the white dashed area.

This work focuses on the development of application-specific microwave resonators to solve three challenges of modern EPR spectroscopy. Specifically, the three challenges investigated in this dissertation are tp: (i) Improve the microwave magnetic field homogeneity for pulse EPR at Q-band frequencies; (ii) Enhance the sensitivity of thin-film samples in the THz-bandgap by the implementation of meta-materials; (iii) Improve the absolute sensitivity at X-band frequencies for the study of protein single-crystals with volumes less than 30 nl.

Improving the microwave magnetic field homogeneity for pulse EPR at Q-band frequencies. With the inclusion of arbitrary waveform generators to modern EPR spectrometers, it has become increasingly important to have control over the excitation profile of the sample.[1.2, 1.3] The excitation profile becomes crucial as the pulse sequences become more complex[1.4–7] or when performing spin-spin distance measurements with radicals of different saturation profiles.[1.8] Typically, a cosine dependence of the magnetic field along the sample axis exists, for example, in the conventional cylindrical TE_{102} cavity shown in Fig. 1.1. As such, the sample experiences different excitation profiles which can limit the sensitivity and quality of pulse data. This is improved by the implementation of loop-gap resonators, but these geometries required smaller samples that limit concentration sensitivity. Herein, geometries that bridge

the gap between cavities and loop-gap resonators are explored. By improving of the homogeneity of the microwave magnetic field[1.9] and increasing the resonator bandwidth, an enhancement for frozen solution pulse EPR experiments is demonstrated. Such experiments are used to determine the principal values of the g-tensor or, using ELDOR-detected NMR (EDNMR), ESEEM, and/or HYSCORE spectroscopies, access hyperfine and quadrupole principal values of coupled nuclei.[1.10]

Enhancing the sensitivity of thin-film samples in the THz-bandgap by the implementation of meta-materials. Performing EPR at extreme microwave frequencies (up to 1 THz; THz-bandgap) requires high concentrations of samples since single-mode cavities are not geometrically feasible due to manufacturing and sample handling constraints. Usually, samples are formed into pellets and placed in the instrument for measurement.[1.11] For many samples, such as powder or high concentrations of frozen proteins, this treatment is acceptable. However, for thin-films of paramagnetic materials, such as the study of metal-oxides for electronic and photonic devices, this is not feasible.[1.12] This investigation of meta-materials at THz-bandgap frequencies was driven by this need.

Herein, the meta-material consists of an array of split-ring resonators that cover the surface of a 12 mm diameter quartz glass. The meta-material removes the cross-sectional geometry constraints which are dictated by the wavelength of the frequency allowing for more sample, and therefore more EPR signal, at extremely high microwave frequencies. The use of meta-materials at THz frequencies has been previously studied from a context of strong- and weak-coupling between the spin resonance and frequency-dependent meta-material characteristics.[1.13–15] However, these studies do not have an interest in the EPR signal and only seek to use the spin transitions to study light-matter interactions. In this work, we use the frequency-domain Fourier-transform EPR experiment to measure the interactions between the meta-material and EPR signal. A lumped-circuit transmission-line model describing the system was formulated to reproduce the complex interactions between the magnetic susceptibility of the sample and the frequency-dependent meta-material. Such interactions become increasingly important as the resonant probe geometry volume approaches the sample volume and in multi-wavelength probe designs found at higher frequencies.[1.16]

Improving the absolute sensitivity at X-band frequencies for the study of protein single-crystals with volumes less than 30 nl. Absolute sensitivity remains a challenge in EPR spectroscopy. This is especially true at X-band frequencies (9.5 GHz) where the majority of commercial EPR systems operate. By increasing the absolute sensitivity for sample volumes less than 30 nl a spectrocsopist could perform multi-frequency EPR using the same sample at X-band and high frequencies, such as W-band (94 GHz).

This work focuses on the application of single-crystal EPR to protein crystals which are severely size limited by the availability of only small crystals. Crystal volumes are in the nanoliter to sub-nanoliter ranges, which are typical for X-ray crystallography diffraction studies but cannot be used in EPR due to lack of sensitivity. Typically, high-frequency EPR is utilized when the volume of a sample is limited.[1.16] Although commercially available, high-frequency spectrometers are not readily available in most laboratories.

As a direct application, the resonant geometry developed here is employed to study [FeFe]-hydrogenase in the stable catalytic intermediate of H_{ox} in protein single-crystals with dimensions less than 3 nl. By studying proteins in single-crystals, the angular

dependencies of the magnetic parameters can be obtained. These angular dependencies help build a complete picture of the chemical structure and function of the active site of an enzyme.[1.17–19]

This dissertation is compiled in the following way. In Chapter 2, the basic understanding of EPR and general concepts for this work is introduced. Each main chapter is self-contained with an introduction, methods, results, and conclusion section. In chapter 3, a uniform field re-entrant TE_{01U} is investigated and experimental measurements are provided. Chapter 4 is concerned with thin-film samples in the 100 GHz to 1 THz frequency range (3.34-33.36 cm^{-1} energy range; THz-bandgap) and the implementation of meta-material surfaces. An analytical transmission-line model is proposed to describe the interaction of the meta-material surface and sample. Experimental measurements and analytical calculations are compared. Chapter 5 introduces the self-resonant microhelix for protein single-crystal studies and Chapter 6 uses this novel resonator to study the metallo-enzyme [FeFe]-hydrogenase in the stable catalytic intermediate of H_{ox} in protein single-crystals with a volume less than 3 nl.

CHAPTER 1. REFERENCES

[1.1] J. Weil, J. Bolton, Electron Paramagnetic Resonance: Elementary Theory and Practical Applications, Wiley, 2007.

[1.2] A. Doll, G. Jeschke, Fourier-transform electron spin resonance with bandwidth-compensated chirp pulses, J. Magn. Reson. 246 (2014) 18–26.

[1.3] N. Wili, G. Jeschke, Chirp echo Fourier transform EPR-detected NMR, J. Magn. Reson. 289 (2018) 26–34.

[1.4] S. Milikisyants, F. Scarpelli, M. G. Finiguerra, M. Ubbink, M. Huber, A pulsed EPR method to determine distances between paramagnetic centers with strong spectral anisotropy and radicals: The dead-time free RIDME sequence, J. Magn. Reson. 201 (1) (2009) 48–56.

[1.5] F. D. Breitgoff, J. Soetbeer, A. Doll, G. Jeschke, Y. O. Polyhach, Artefact suppression in 5-pulse double electron electron resonance for distance distribution measurements, Phys. Chem. Chem. Phys. 19 (2017) 15766–15779.

[1.6] A. Doll, G. Jeschke, EPR-correlated dipolar spectroscopy by Q-band chirp sifter, Phys. Chem. Chem. Phys. 18 (2016) 23111–23120.

[1.7] F. D. Breitgoff, K. Keller, M. Qi, D. Klose, M. Yulikov, A. Godt, G. Jeschke, UWB DEER and RIDME distance measurements in Cu(II)–Cu(II) spin pairs, J. Magn. Reson. 308 (2019) 106560.

[1.8] A. Meyer, J. J. Jassoy, S. Spicher, A. Berndhäuser, O. Schiemann, Performance of PELDOR, RIDME, SIFTER, and DQC in measuring distances in trityl based bi- and triradicals: Exchange coupling, pseudosecular coupling and multi-spin effects, Phys. Chem. Chem. Phys. 20 (2018) 13858–13869.

[1.9] J. S. Hyde, J. W. Sidabras, R. R. Mett, Uniform field resonators for EPR spectroscopy: A review, Cell Biochemistry and Biophysics 77 (1) (2019) 3–14.

[1.10] J. Harmer, G. Mitrikas, A. Schweiger, Advanced Pulse EPR Methods for The Characterization of Metalloproteins, Springer New York, 2009, pp. 13–61.

[1.11] J. Nehrkorn, K. Holldack, R. Bittl, A. Schnegg, Recent progress in synchrotron-based frequency-domain fourier-transform THz-EPR, J. Magn. Reson. 280 (2017) 10–19.

[1.12] K. Dyrek, M. Che, EPR as a tool to investigate the transition metal chemistry on oxide surfaces, Chem. Rev. 97 (1) (1997) 305–332.

[1.13] A. Schneider, A. Shuvaev, S. Engelbrecht, S. O. Demokritov, A. Pimenov, Electrically excited inverse electron spin resonance in a split-ring metamaterial resonator, Phys. Rev. Lett. 103 (2009) 103907.

[1.14] G. Boero, G. Gualco, R. Lisowski, J. Anders, D. Suter, J. Brugger, Room temperature strong coupling between a microwave oscillator and an ensemble of electron spins, J. Magn. Reson. 231 (2013) 133–140.

[1.15] G. Scalari, C. Maissen, D. Turčinková, D. Hagenmüller, S. De Liberato, C. Ciuti, C. Reichl, D. Schuh, W. Wegscheider, M. Beck, J. Faist, Ultrastrong coupling of the cyclotron transition of a 2d electron gas to a THz metamaterial, Science 335 (6074) (2012) 1323–1326.

[1.16] O. Grinberg, L. Berliner, Very High Frequency (VHF) ESR/EPR, Biological Magnetic Resonance, Springer US, 2004.

[1.17] C. Geßner, O. Trofanchuk, K. Kawagoe, Y. Higuchi, N. Yasuoka, W. Lubitz, Single crystal EPR study of the Ni center of NiFe hydrogenase, Chem. Phys. Lett. 256 (4) (1996) 518–524.

[1.18] O. Trofanchuk, M. Stein, C. Geßner, F. Lendzian, Y. Higuchi, W. Lubitz, Single crystal EPR studies of the oxidized active site of [NiFe] hydrogenase from Desulfovibrio vulgaris Miyazaki F, J. Biol. Inorg. Chem. 5 (1) (2000) 36–44.

[1.19] S. Foerster, M. Stein, M. Brecht, H. Ogata, Y. Higuchi, W. Lubitz, Single crystal EPR studies of the reduced active site of [NiFe] Hydrogenase from Desulfovibrio vulgaris Miyazaki F, J. Am. Chem. Soc. 125 (1) (2003) 83–93.

2. Theory and Experimental Methods

2.1. EPR spectroscopy

In this section, the underlying theoretical and practical principles of the EPR experiment are discussed as it relates to the experiments performed in this work.

2.1.1. Spin Hamiltonian

The complete Hamiltonian $\mathcal{H}_0$ of a molecular system is very complex. All of the space and spin coordinates of electrons and nuclei would be included in the complete Hamiltonian, such that,

$$\mathcal{H}_0|\Psi\rangle = \mathbf{E}|\Psi\rangle \tag{2.1}$$

where the wave function $|\Psi\rangle$ describes how the molecular system is propagated over time, known as the time-dependant Schrödinger equation. Since EPR measures the time-invariant ground states, it is sufficient to describe only the interactions of the atomic system energy contained in the Hamiltonian. These energy states $\mathbf{E}$ are further simplified by the phenomenologically derived spin Hamiltonian operator $\hat{\mathcal{H}}$. Then the time-dependant Schrödinger equation only includes the spin states of the system.[2.1, 2.2]

The spin Hamiltonian comprises of the superposition of the magnetic and electric properties of the molecular system, such that,

$$\hat{\mathcal{H}} = \hat{\mathcal{H}}_{ze} + \hat{\mathcal{H}}_{hfi} + \hat{\mathcal{H}}_{nz} + \hat{\mathcal{H}}_{nqi} + \hat{\mathcal{H}}_{zfs}, \tag{2.2}$$

where the electron Zeeman interaction $\hat{\mathcal{H}}_{ze}$, the hyperfine interaction $\hat{\mathcal{H}}_{hfi}$, the nuclear Zeeman interaction $\hat{\mathcal{H}}_{nz}$, and, for nuclei with $I > 1/2$, the electric-nuclear quadrupole interactions $\hat{\mathcal{H}}_{nqi}$. The zero-field splitting term $\hat{\mathcal{H}}_{zfs}$, is characterized by energy differences of the degenerate states without an applied static magnetic field.

In this formulation, the static magnetic field $\mathbf{B}_0$ was assumed to be along the z axis and denote the transpose of a tensor with a 'T'. Except in cases of zero-field splitting, it was also assumed that the electron Zeeman interaction is the largest interaction followed by the hyperfine interaction, nuclear Zeeman, electric quadrupole.

Zeeman interactions

When a static magnetic field is applied to a molecular system with angular momentum, the angular momentum aligns in such a way that a Boltzmann distribution is formed. This removes the degeneracy of the electron magnetization $\mathbf{M}_s$ manifold, splitting the energy levels, illustrated in Fig. 2.1 as the initial splitting. For an electron spin of $S = 1/2$, the initial energy levels are split into $\mathbf{M}_s = |+\frac{1}{2}\rangle, |-\frac{1}{2}\rangle$ for spin-up and spin-down, respectively. Both the electron $\hat{\mathcal{H}}_{ze}$ and nuclear $\hat{\mathcal{H}}_{nz}$ Zeeman interactions occur when a static magnetic field $\mathbf{B}_z$ is applied.

The electron Zeeman interaction is defined by

$$\hat{\mathcal{H}}_{ze} = \beta_e \mathbf{B}_z^{\mathrm{T}} \cdot \mathbf{g} \cdot \mathbf{S}$$

where β_e is the Bohr magneton, the transpose of the static magnetic field $\mathbf{B}_z^{\mathrm{T}}$, the vector operator $\mathbf{S} = [\mathbf{S}_x\ \mathbf{S}_y\ \mathbf{S}_z]$ is the spin operator of the angular momentum of the electron.

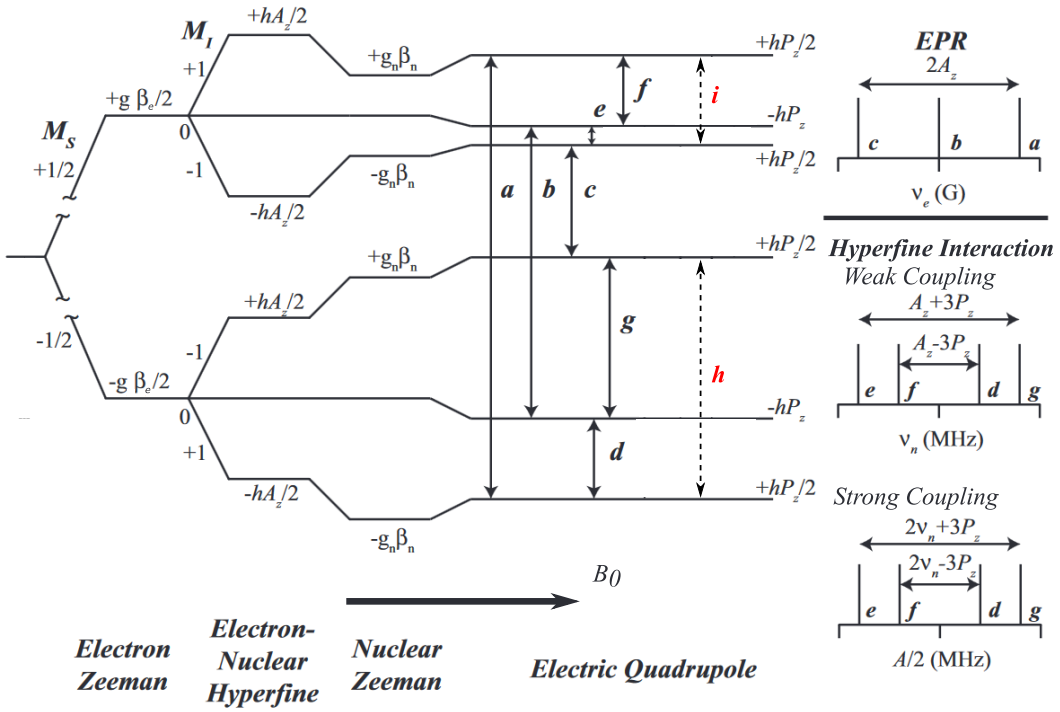

Figure 2.1.: Energy diagram example of a spin system with $S = 1/2$, $I = 1$, and first-order quadrupole interactions. The transitions **a**, **b**, and **c** are EPR transitions. The nuclear hyperfine-interaction transitions are marked as **d**, **e**, **f**, and **g**. The transitions shown as dashed lines are semi-forbidden "double quantum" $\Delta M_I = \pm 2$ transitions and marked in red as marked as **h** and **i**. Modified with permission from Fig. 2 of Ref. [2.3].

An unpaired electron in a vacuum has an isotropic spin with angular momentum. It is then the interaction of an electron with other electrons and nuclear spins and how those atoms distribute the electron that gives rise to different components of the spin Hamiltonian.[2.4, 2.5] This "pushing" and "pulling" of the electron by spin-orbit coupling leads to anisotropic **g**. The matrix **g** is what is known as the g-tensor and is a spatial distribution of the angular momentum of the electron. The g-tensor is typically made diagonal and discussed in terms of the g_x, g_y, and g_z principal components, where the magnitude is denoted as g_{iso}. EPR resonance occurs as a result of the incident energy matching the energy difference of the electron Zeeman levels.

Deviations from a free-electron can be used to obtain information on the local environment. Since these processes are non-cooperative, we can separate the free-electron from all the other contributions

$$\mathbf{g} = g_e\mathbf{1} + \Delta\mathbf{g},$$

where **1** is the identity matrix and $\Delta\mathbf{g}$ includes isotropic atomic interaction terms as well as second-order spin-orbit coupling terms. The interaction between the electron spin and the atomic orbitals of the molecule arise due to the magnetic moment of the electron.[2.6] The electron Zeeman $\hat{\mathcal{H}}_{ze}$ interaction is then a perturbation of the free electron in the ground state.

For systems when the electron interacts with intrinsic or surrounding nuclei with a

nuclear spin I_k, the Nuclear Zeeman effect is added to $\hat{\mathcal{H}}$ as

$$\hat{\mathcal{H}}_{nz} = -\beta_n \sum_{k=1}^{m} g_{n,k} \mathbf{B}_z^{\mathrm{T}} \cdot \mathbf{I}_k,$$

where β_n is the nuclear magneton, the transpose of the static magnetic field $\mathbf{B}_z$ is marked with a 'T', the vector operator $\mathbf{I}_k = [\mathbf{I}_x \ \mathbf{I}_y \ \mathbf{I}_z]$ is the spin operator of the angular momentum of the nuclei. The summation of the nuclear contributions are represented by the index k for each m nucleus that interacts with the electron. Each nucleus has a distinct nuclear $g_{n,k}$-value and angular momentum $\mathbf{I}_k$ and is assumed to be isotropic. The visualization of the nuclear Zeeman effect is illustrated as a perturbation on the electron-nuclear hyperfine interaction shown in Fig. 2.1.

Nuclear-Electron Interactions

Since EPR is the measurement of how a valence (unpaired) electron interacts with the surrounding environment, information on the surrounding nuclei is possible if these nuclei have an inherent nuclear spin **I**. Such nuclei include, for example, ^{1}H, ^{2}H, ^{14}N, ^{15}N, ^{57}Fe, and ^{13}C, which can be synthetically incorporated into the system to gain more information than the natural abundance of some of the atoms.[2.3, 2.7, 2.8]

Hyperfine Interactions The hyperfine interactions are defined as the coupling between the paramagnetic site and the surrounding nuclei. This can be broken up into two distinct parts, the isotropic Fermi contact interaction, a_{iso}, and the electron-nucleus magnetic dipole-dipole coupling. The hyperfine interactions can be expressed as

$$\hat{\mathcal{H}}_{hfi} = \mathbf{S}^{\mathrm{T}} \cdot \mathbf{A} \cdot \mathbf{I}_k = a_{iso} \mathbf{S}^{\mathrm{T}} \cdot \mathbf{I}_k + \mathbf{S}^{\mathrm{T}} \cdot \mathbf{T} \cdot \mathbf{I}_k \tag{2.3}$$

for each of the interacting nuclei k, there exists such an interaction. The Fermi contact is proportional to electron spin density at the nucleus. At a sufficient distance (>0.26 nm), the spacial tensor **T** can be described by

$$\mathbf{T} = \frac{\mu_0}{4\pi\hbar} \frac{1}{r^3} g_n \beta_n \beta_e g_i (3 r_i r_j - \delta_{ij}) \qquad (i, j = x, y, z), \tag{2.4}$$

where the x, y, and z-components of the hyperfine tensor are treated independently.[2.7] Illustrated in Fig. 2.1 is the nuclear-electron hyperfine interaction assuming only the isotropic component of interaction. In frozen solution, this isotropic component is broadened by the distribution of the frequency components defined by **T**. Only single-crystal EPR spectroscopy can truly obtain the full hyperfine-tensor information for systems with anisotropic hyperfine interactions **T** by measuring the total hyperfine interaction **A**.

Electric-Nuclear Quadrupole Interactions The electric-nuclear quadrupole interaction only exists for nuclei with a spin I greater than 1/2 and is caused by electric field gradients due to the interaction of the electron with the quadrupole coupling. This coupling can be described as the second moment of the nuclear angular momentum. This can be rationalized since the nuclear Zeeman interaction is assumed to be isotropic, while the second moment (gradient) is a measurement of the deviation from isotropic angular momentum.[2.6] One can learn about the nature of the chemical bonding and the delocalization of the electron if the interaction between the nuclear quadrupole coupling and electron is known.[2.9]

The electric-nuclear quadrupole interaction is described by the Hamiltonian

$$\hat{\mathcal{H}}_{nqi} = \hat{\mathbf{I}}^{\mathrm{T}} \cdot \mathbf{P} \cdot \hat{\mathbf{I}} \tag{2.5}$$

where

$$\mathbf{P} = P_{||} \begin{bmatrix} \eta_Q - 1 & 0 & 0 \\ & \eta_Q - 1 & 0 \\ & & 2 \end{bmatrix} \tag{2.6}$$

and the value

$$P_{||} = \frac{3eQ}{4I(2I-1)} \frac{\partial^2 V}{\partial z^2} = \frac{3P_z}{2} \tag{2.7}$$

where $\frac{\partial^2 V}{\partial z^2}$ is the electric-field gradient seen by the nucleus and $|e|Q$ describes the electric shape of the nucleus and is directly determined by the type of nucleus and, here, η is defined as the rhombicity of the electric gradient calculated by $(Px - Py)/P_z$ when $|P_z| \geq |P_y| \geq |P_x|$.[2.4, 2.10] The final EPR spectrum is a combination of all of these effects yielding a change in the Boltzmann population at the static magnetic field position illustrated in Fig. 2.1 as arrows marked **a**, **b**, and **c** and plotted as a transition stick diagram in the top right.

The hyperfine interactions that are measured with some double-resonance experiments are indicated in Fig. 2.1 as the arrows marked **d**, **e**, **f**, and **g**. However, when performing hyperfine spectroscopy the semi-forbidden "double quantum" (DQ) transitions need to be understood. In Fig. 2.1, these transitions are shown as dashed lines and marked in red as **h** and **i**. The DQ transitions are a second-order effect on the electric-nuclear quadrupole interactions and can be calculated by

$$\nu_{\alpha,\beta}^{DQ} = 2\sqrt{\left(\nu_I \pm \frac{a}{2}\right)^2 + \left(\frac{e^2qQ}{4h}\right)(3+\eta)}, \tag{2.8}$$

where a is the hyperfine coupling at the nuclei of interest.[2.7] This splitting further complicates the interpretation of the data. However, when measured in single crystals the double-quantum cross peaks can be used to assign nuclei throughout the rotation.

Multiple Electron Interactions

Zero-field Splitting For many unpaired electrons with strong coupling, an effective spin greater than 1/2 ($S_{eff} > 1/2$) is formed. When this occurs, there exists an internal interaction that splits the energy levels of the ground state with no applied external field. This interaction, named zero-field splitting, is defined as

$$\hat{\mathcal{H}}_{zfs} = \mathbf{S}^{\mathrm{T}} \cdot \mathbf{D} \cdot \mathbf{S} \tag{2.9}$$

where the zero-field splitting tensor $\mathbf{D}$ is a traceless symmetric interaction from close spin-orbital coupling between two or more electrons. The zero-field splitting is especially important in molecular magnets, where it is the direct characterization of the magnetization caused by the interactions of electrons as magnetic monopoles.[2.11] With very large values of D, the EPR transition energies can only become excited with high-field–high-frequency EPR methods.[2.12]

2.2. On the use of Magnetic Field and Flux Density

The EPR literature uses the magnetic field $\mathbf{H}$ and magnetic flux density $\mathbf{B}$ interchangeably as "magnetic field". It is somewhat disingenuous to state that the relationship of the magnetic field and magnetic flux density is simply related by the free-space permeability

μ_0. The focus of this section is to define the usage in this dissertation by following the nomenclature of Jackson of Ref. [2.13] so that

$$\mathbf{B} = \mu_0(\mathbf{M_0} + \mathbf{H}), \tag{2.10}$$

where the SI units for $\mathbf{B}$ is measured in Tesla, while $\mathbf{H}$ is calculated in Ampere per meter. The magnetic susceptibility $\mathbf{M_0}$ becomes relevant when the time-varying magnetic flux density $\mathbf{B}$ is incident on a material, such as a sample. For brevity, the time-varying magnetic flux density is defined as

$$\mathbf{B}_1 = \mathbf{B}e^{-i\omega t} \tag{2.11}$$

where ω is the frequency of interest (radians per second). It is the magnetic flux density that is incident on the sample defined by the magnetic field profile of the microwave resonator. As anticipated, the magnetic susceptibility is material-specific and is proportional to the magnetic moment of the material. In a macroscopic sense, it is the perturbation of this magnetic moment that is measured in EPR. For experimental methods, this is described in detail in Section 2.5 and used extensively in the formulation of Chapter 4.

From Maxwell's equations, the magnetic field is calculated by the curl of the magnetic vector potential which, in a vacuum, describes the relationship of the applied currents to the geometry and boundary conditions.[2.13] In this dissertation when a microwave resonator is discussed, it is the magnetic field profile that is calculated and plotted. However, it is the magnetic flux density that interacts with the sample and is the experimentally measurable quantity. This is because the magnetic flux density is the mechanical torque that is applied to the magnetic moment of the material.

This distinction is constant throughout the dissertation. If the quantity is measurable and interacts with the sample, it must be described in terms of the magnetic flux density $\mathbf{B}_1$, while calculated profiles are described in terms of magnetic field $\mathbf{H}_1$.

Finally, the static magnetic field is simply referred to as $\mathbf{B}_0$ with units of milliTesla (10^{-1} Gauss[1]) since this field is not time-varying. A static magnetic field is the only instance where the dual "magnetic field" nomenclature is correct when referring to $\mathbf{B}$.

2.3. Crystal Orientations and Molecular Frames

In this section, the basic understanding of crystal orientations and how to relate them to the EPR experiment is discussed.

Laboratory System Frame The Laboratory system frame [$\mathbf{L}_1$ $\mathbf{L}_2$ $\mathbf{L}_3$] is illustrated in Fig. 2.2 as the blue coordinate system. The laboratory system frame represents the physical coordinates of the EPR laboratory. The laboratory system frame is defined with the static magnetic field ($\mathbf{B}_0$) oriented along the L_1-axis, while the microwave magnetic flux density ($\mathbf{B}_1$) is along the L_3-axis.

Crystal Frame The crystal frame [**a b c**] is defined with respect to the laboratory frame. When the crystal is inserted into the resonator, the crystal orientation is typically unknown. The crystal frame rotation can be defined by a set of Euler angles. Herein the nomenclature of the EasySpin simulation package is used.[2.15] The three Euler angles (α, β, γ) define the rotation around defined axes of the current frame. The first angle α

[1] In modern EPR literature the use of mT is now favored over G for compatability to SI units.

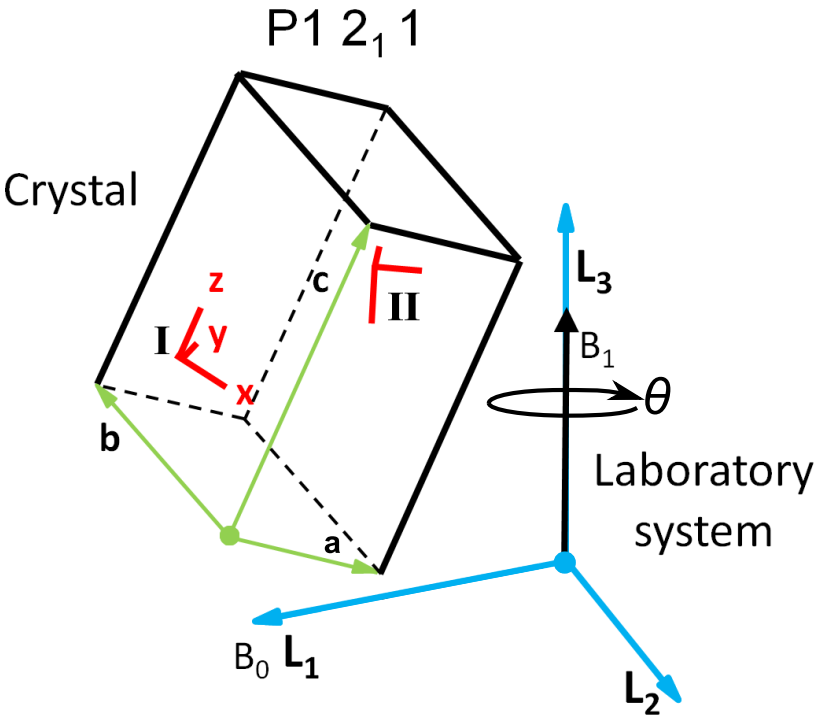

Figure 2.2.: Relation of the Laboratory system frame [$\mathbf{L}_1$ $\mathbf{L}_2$ $\mathbf{L}_3$] to the crystal frame [**a** **b** **c**] and the molecular frame [**x** **y** **z**]. The molecular frame at Site I and Site II are related the crystal symmetry. The P1 2_1 1 crystal symmetry depicted here is occurs in CpI [FeFe]-hydrogenase PDB ID: 4XDC.[2.14] used in Chapter 6.

is a rotation around the z-component, defined by

$$Rot_z[\theta] = \begin{bmatrix} Cos[\theta] & -Sin[\theta] & 0 \\ Sin[\theta] & Cos[\theta] & 0 \\ 0 & 0 & 1 \end{bmatrix} \tag{2.12}$$

and the second angle β is a rotation around the new y-component denoted y', defined by

$$Rot_y[\theta] = \begin{bmatrix} Cos[\theta] & 0 & Sin[\theta] \\ & 1 & 0 \\ -Sin[\theta] & 0 & Cos[\theta] \end{bmatrix} \tag{2.13}$$

and finally the angle γ is another rotation around the new z-component denoted z''. This is aptly named the zyz convention. This transformation can be performed directly by calculating the rotation matrix, such that

$$Rot_{zyz}[\alpha, \beta, \gamma] = Rot_{z''}[\gamma] \cdot Rot_{y'}[\beta] \cdot Rot_z[\alpha], \tag{2.14}$$

and applying it to the coordinates of the crystal frame

$$\begin{bmatrix} \tilde{x}_{\mathrm{L1}} & \tilde{x}_{\mathrm{L2}} & \tilde{x}_{\mathrm{L3}} \\ \tilde{y}_{\mathrm{L1}} & \tilde{y}_{\mathrm{L2}} & \tilde{y}_{\mathrm{L3}} \\ \tilde{z}_{\mathrm{L1}} & \tilde{z}_{\mathrm{L2}} & \tilde{z}_{\mathrm{L3}} \end{bmatrix} = Rot_{zyz}[\alpha, \beta, \gamma] \cdot \begin{bmatrix} a_1 & a_2 & a_3 \\ b_1 & b_2 & b_3 \\ c_1 & c_2 & c_3 \end{bmatrix}. \tag{2.15}$$

Using Eqn. 2.15, the crystal frame [**a** **b** **c**] is rotated with respect to the laboratory frame [$\mathbf{L}_1$ $\mathbf{L}_2$ $\mathbf{L}_3$].

Molecular Frame The molecular frame relates the measured atomic structure from X-ray crystallography diffraction experiments to the crystal frame. In Fig. 2.2, the molecular frame is represented by the red coordinate systems sites labeled I and II (Site I and Site II). This frame is arbitrary and is defined by the spectroscopist. The frame consists of a rectangular coordinate system and is defined with a set origin. For EPR, the origin is chosen to be where a majority of the spin density is expected to reside. This can be aided by quantum chemical calculations. The illustration of Fig. 2.2 is depicting P1 2_1 1 crystal symmetry where a second axis (Site II) is defined by a rotation and translation in the direction of the **b**-axis, see below.

During crystallization, an asymmetric unit may form. An asymmetric unit is where two or more enzymes bind together to form a sub-unit cell that is rotated and translated, as a whole, within the crystal symmetry. These sub-units must be consistent within the entire volume to obtain good X-ray crystallography diffraction data. Since each one of the enzymes produces an EPR signal the asymmetric unit must be taken into account. This is done by defining a second (or more) molecular frame per site. Again, the X-ray crystallography diffraction data provides the sub-unit geometry and a rectangular coordinate system is defined.

Every frame that gives rise to the EPR signal is derived from the molecular frame.

g-Tensor Frame The g-tensor frame is an approximation in the rectangular coordinate system to the relationship of the g_x, g_y, and g_z components of the g-tensor. This rectangular coordinate system is defined from a rotation from the chosen molecular frame. For this reason, it is important to choose the molecular frame to have an origin where the majority of spin density resides. In EasySpin, the g-tensor frame is represented as Euler angles or rotation matrices.

A-Tensor and Quadrupole Frames The A-tensor frame is, in rectangular coordinates, the relationship of the total hyperfine-interaction A_x, A_y, and A_z components to the molecular frame. While the quadrupole frame represents the relationship of $P_{||}$ to the molecular frame.

Similar to the g-tensor, they are defined from a rotation from the chosen molecular frame. In EasySpin, the A-tensor and quadrupole frames can be represented as Euler angles or rotation matrices.

Crystal Symmetry In general, the crystal symmetry can be described by Euler angle rotation and a spacial translation.[2.16] From the vector $\mathbf{x}$ a copy to the "equivalent position" $\tilde{\mathbf{x}}$ is formed at the rotated $R_{zyz}[\alpha, \beta, \gamma]$ and translated $\mathbf{t}$ position in the crystal, described by

$$\tilde{\mathbf{x}} = R_{zyz}[\alpha, \beta, \gamma] \cdot \mathbf{x} + \mathbf{t}. \tag{2.16}$$

For the P1 2_1 1 symmetry, it has a $[\tilde{a},\ \tilde{b},\ \tilde{c}]$ of $[-a,\ b+1/2,\ -c]$. This can be performed with a rotation matrix and translation defined by

$$\begin{bmatrix} \tilde{a} \\ \tilde{b} \\ \tilde{c} \end{bmatrix} = \begin{bmatrix} -1 & 0 & 0 \\ 0 & 1 & 0 \\ 0 & 0 & -1 \end{bmatrix} \cdot \begin{bmatrix} a \\ b \\ c \end{bmatrix} + \begin{bmatrix} 0 \\ 1/2 \\ 0 \end{bmatrix}, \tag{2.17}$$

and places the enzyme at Site II. The crystal symmetry can be taken into account in the EasySpin simulations where the duplication and rotation of the molecular frame is automatically generated.

For the case of the CpI [FeFe]-hydrogenase from PDB ID 4XDC,[2.14] the enzymes crystallize into a P1 2_1 1 symmetry and each site contains an asymmetric sub-unit consisting of two enzymes. Two molecular frames are defined and the P1 2_1 1 crystal symmetry duplicates the asymmetric unit from Site I to Site II, illustrated in Fig. 2.2. For EPR,

each molecular frame per asymmetric unit gives rise to an EPR signal. Therefore, for CpI [FeFe]-hydrogenase from PDB ID 4XDC, there will exist four total EPR signals per unit cell, see Chapter 6.

The quality of the protein single-crystal is important to both the characteristics of the acquired EPR signal and the consistency of the fit for the molecular frame. Crystals grown from proteins can suffer from mosaicity, which is a crystalline state where a single crystal may be broken into blocks of unit cells that are disassociating from the whole crystal. However, mosaicity is only a perturbation on the whole crystal and is not yet poly-crystalline, where the unit cells have formed a semi-random orientation.

Mosaicity can affect both the X-ray crystallography diffraction data and the EPR signal. Such mosaicity effects are apparent in the X-ray crystallography diffraction data by limits imposed on the spatial resolution of the electron density map.[2.17] Depending on the severity, the EPR signal will be broadened which reduces the overall signal-to-noise ratio. These effects may be reduced by annealing techniques.[2.18]

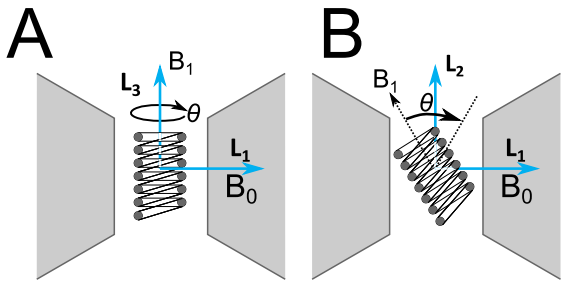

Figure 2.3.: Shown are the two rotation planes available for crystal rotation in the self-resonant micro-helix of Chapter 5. A) A full 180 degree rotation is available when the $\mathbf{B}_1$ is along the L_3-axis. B) A second plane is available where the $\mathbf{B}_1$ is along the L_2-axis. A rotation in this plane is limited by a sinusoidal dependence of the EPR signal.

Crystal Rotation To obtain a magnetic resonance rotation pattern, the crystal must be rotated with respect to $\mathbf{B}_0$, illustrated in Fig. 2.3A. This is currently performed by rotating the entire resonator probe around the L_3-axis. If a second plane is needed, the angle can be modified by orientating the $\mathbf{B}_1$ along the L_2-axis, illustrated in Fig. 2.3B by using a 90° bend. This secondary plane of rotation is limited since the EPR signal is reduced as $\mathbf{B}_1$ becomes parallel to $\mathbf{B}_0$. With a good signal-to-noise ratio, EPR can be collected over a 120 degree rotation in this plane.

2.4. Finite-element modeling Simulations

Commercially available electromagnetic finite-modeling software provides a suite in which boundary conditions, sources, and dielectric properties are combined to solve Maxwell's equations in a CAD-like environment. In this dissertation, finite-element modeling is used to design, understand, and optimize microwave resonators. Here, an introduction to Ansys Electromagnetics Suite (Pittsburgh, PA, USA; version 19.4; High Frequency Structure Simulator (HFSS)) and a practical exercise will be developed.

Ansys HFSS employs "driven-mode" and "eigenmode" solving domains. The "eigenmode" solver uses Maxwell's equations in their variational form to find the lowest energy states of a structure given its boundary conditions and electromagnetic material properties.[2.19, 2.20] This lowest energy state, or eigenvalue, is then used to calculate the

eigenvectors of the structure, yielding a wave solution. The eigenvalue problem assumes that both the differential equations and the boundary conditions are homogeneous. There is no source exciting the mode of interest. This becomes very important in geometries where the modes of the system are not known. In Ansys Electronics Desktop, solutions are normalized by the electric field (1 V/m) or to the stored electric energy.

The "driven-mode" solves the non-homogeneous Maxwell's equations. Practically, one must devise a coupling system in "driven-mode" and, in this work, impedance matching considerations are implemented to maximize power transfer to the resonator. The "driven-mode" provides outputs similar to a vector network analyzer and is typically normalized to an input power of 1 W.

Signal Calculations and Resonator Comparisons. A method to obtain the EPR signal has been formulated and is reproduced here.[2.21] This method uses the fields calculated in Ansys HFSS, accessed by the "Field Calculator", to determine a normalized EPR signal under saturating or nonsaturating conditions. This calculation can be performed using eigenmode or driven-mode methods and the scripts for Ansys HFSS are found in Appendix B.[2]

For a matched reflection cavity and a voltage-sensitive detector, Feher expressed the microwave EPR signal as

$$S \propto \chi'' \eta Q P^{1/2} \qquad \text{[V]}, \tag{2.18}$$

where χ'' is the imaginary part of the magnetic susceptibility which represents the magnitude of the absorption spectrum, η is the filling factor, Q is the unloaded Q_0-value with a sample, and P is the incident microwave power.[2.22] The signal is proportional to volts when the system is critically coupled and calculated at microwave resonance. When comparing resonators, we assume the sample has the same concentration for an arbitrary volume and, as such, the rf magnetic susceptibility χ'' is simply proportional to frequency. This assumption is used to incorporate the Boltzmann factor to resonator comparisons (i.e. temperature or frequency differences).

The Q-value of the system can be calculated by the ratio of the total stored energy of the resonator by the power losses per cycle. Such that

$$Q = \frac{\omega U_m}{P_l}, \tag{2.19}$$

where ω is the microwave resonance frequency in radians per second, U_m is the stored magnetic energy, and P_l is the power losses in the cavity walls and sample. At resonance, the magnetic and electric stored energy are equal.[2.23] However, the magnetic stored energy is chosen for simplicity when dealing with a geometry where there are different dielectric volumes. Electric stored energy includes the relative permittivity ϵ_r accounted for in each volume, while magnetic stored energy includes the relative permeability μ_r. In this formulation we assume to be "on magnetic resonance" and, therefore, are not measuring the change in the relative permeability. Consequently, only the free-space permeability μ_0 is needed. Therefore the magnetic stored energy is

$$U_m = \frac{\mu_0}{2} \int \mathbf{H}_1 \cdot \mathbf{H}_1^* dV \qquad \text{[W]}, \tag{2.20}$$

where $\mathbf{H}_1$ is the microwave magnetic field in all space (V) including the sample.

[2]All codes and HFSS files can be found at https://github.com/jsidabras/HFSSTutorial/.

The filling factor is defined as the ratio of the magnetic flux density energy in the sample that gives rise to an EPR signal to the microwave magnetic field energy in all space. This can be calculated as

$$\eta = \frac{\int \mathbf{B}_{1r} \cdot \mathbf{B}_{1r}^{*} dV_s}{\int \mathbf{B}_1 \cdot \mathbf{B}_1^{*} dV}, \tag{2.21}$$

where $\mathbf{B}_{1r}$ is one component of the clockwise (or counter clockwise) rotational component of the linearly polarized flux density $\mathbf{B}_1$ perpendicular to the static magnetic field in the sample volume (V_s).[2.13] In magnetic resonance, the spin system is coupled to either the right-handed or left-handed (clockwise or counter clockwise) polarization of the magnetic flux density.[2.2]

A linearly polarized wave can be decomposed into two in-phase circular components. From Ref. [2.13], an expression for the right-handed (+) or left-handed (−) component of the magnetic flux density can be derived, such that

$$\mathbf{B}_{1\pm} = \mathbf{B_1} \cdot \frac{\hat{\mathbf{y}} \pm i\hat{\mathbf{z}}}{\sqrt{2}} \qquad [\mathrm{T}], \tag{2.22}$$

where the static magnetic field B_0 is in the $\hat{\mathbf{x}}$ direction. In cavity resonators the left- and right-handed components are equal. However, open structures, systems with complex dielectric properties, and multiple wavelengths within the sample could exhibit elliptical polarization. This results in different magnitudes and field profiles for the two components. The component of the magnetic flux density that interacts with the sample during resonance is the amplitude of Eqn. 2.22, therefore, the magnitude of the microwave magnetic flux density in the (right-handed) rotating frame is the amplitude of $\mathrm{Re}(\mathbf{B}_{1+}\epsilon_+ e^{-iwt})$ such that

$$\mathbf{B}_{1r} = \frac{|\mathbf{B}_{1+}|}{\sqrt{2}} \qquad [\mathrm{T}]. \tag{2.23}$$

Herein, this formulation was only applied to systems that exhibit linear polarization in the sample (Chapter 3 and 5) and other methods were relied upon to approximate the EPR signal in cases where multiple wavelengths are involved (Chapter 4).

The power loss in the system is broken up into two distinct types: dielectric losses and Ohmic losses on the surfaces of conductors. For a bulk conductor, the power dissipated on the surface can be calculated as

$$P_{lw} = \frac{R_s}{2} \int \hat{\mathbf{n}} \times \mathbf{H} \cdot \mathbf{H}^{*} dS_w \qquad [\mathrm{W}] \tag{2.24}$$

where $\hat{\mathbf{n}}$ is normal to the conductor surface (S_w). The resistance of the surface is calculated by the real part of the surface impedance, defined as

$$Z_s = \sqrt{\frac{\omega\mu_0}{2\sigma}}(1 - i) \tag{2.25}$$

where σ is the conductivity of the metal surface. The power dissipated in a dielectric can be calculated by

$$P_{ld} = \frac{\omega\epsilon_0\epsilon_r''}{2} \int \mathbf{E} \cdot \mathbf{E}^{*} dV_d \qquad [\mathrm{W}], \tag{2.26}$$

where the imaginary part of the dielectric permittivity ($\epsilon_r = \epsilon_r' - i\epsilon_r''$) is integrated over the dielectric volume V_d.[2.13, 2.24] The total power loss of the system is the summation

of all the power losses of the conductors and n is the number of dielectrics which may include the sample, sample tube, and other plastics and ceramics such that

$$P_l = P_{lw} + \sum_{i=1}^{n} P_{ld_i} \qquad \text{[W]}. \tag{2.27}$$

The power loss in the system for the sample, resonator walls, and sample holder end sections is defined as P_s, P_w, and P_e, respectively, in the scripts of Appendix B. The calculations for P_s and P_e rely on the constants *ImDiSam* and *ImDiHold* which are set to the imaginary part of the relative permittivity constant ϵ_r''.

From Eqn. 2.18 the signal can be calculated by substituting the appropriate equations. Two EPR signal conditions can be calculated: signal unsaturable (Su; Unsat.) and signal saturable (Ss; Sat.). In continuous-wave experiments, signal unsaturable is defined as the EPR signal at constant incident power, while signal saturable is defined as the EPR signal at a constant magnetic flux density at the sample.[2.21, 2.25] A saturable sample can be calculated by normalizing to the magnetic flux density and computing

$$S_s = \frac{\chi''\omega}{10^4 P_l^{1/2} \mathrm{Max}|\mathbf{B}_{1r}|} \int \mathbf{B}_{1r} \cdot \mathbf{B}_{1r}^* dV_s \qquad \text{[V]}. \tag{2.28}$$

The unsaturable sample can be calculated by normalizing to the power and computing

$$S_u = \frac{\chi''\omega}{P_l} \int \mathbf{B}_{1r} \cdot \mathbf{B}_{1r}^* dV_s \qquad \text{[V]}. \tag{2.29}$$

The efficiency parameter Λ_{max}, as introduced by Hyde *et al.*[2.25], is defined as

$$\Lambda_{max} = \frac{1}{10} \frac{\mathrm{Max}|\mathbf{B}_{1r}|}{P_l^{1/2}} \quad [\mathrm{mT/W^{1/2}}], \tag{2.30}$$

where $\mathrm{Max}|\mathbf{B}_{1r}|$ is the maximum magnitude of $\mathbf{B}_{1r}$ in the sample (typically in the center of the cavity) and is assumed to be uniform over the sample volume.[2.25] The scalar converts Gauss into milliTesla.

To better assess the resonator efficiency when $\mathbf{B}_{1r}$ is not uniform, an average over the sample volume is calculated,

$$\Lambda_{ave} = \frac{1}{10} \frac{\int \sqrt{\mathbf{B}_{1r} \cdot \mathbf{B}_{1r}^*} dV_s}{P_l^{1/2} V_t} \quad [mT/W^{1/2}], \tag{2.31}$$

where V_t is the total volume of the sample. The average resonator efficiency, which takes into account the $\mathbf{B}_{1r}$ profile along the sample volume, is the measurable value when a nutation experiment is performed.

Finally, the Λ_{ave}-to-Λ_{max} ratio can be used as a metric to quantify the uniformity of the resonator.[2.26] The B_1 profile uniformity (in percent) is defined by

$$\Delta B_1 = \frac{|\Lambda_{max} - \Lambda_{ave}|}{\Lambda_{max}} \times 100\%. \tag{2.32}$$

2.5. Experimental Measurement of EPR Spectra

The EPR experiments performed in this work are as follows:

Continuous-wave EPR.

The continuous-wave (CW) EPR experiment measures the sample using a constant microwave B_1 at a fixed frequency (ω) incident on the sample and slowly sweeping B_0. As the resonance condition is met, when the incident energy ($E = \hbar\omega$) is equal to the Zeeman splitting, the angular momentum is perturbed and an absorption of the energy is recorded.[3]

At the macro-scale view, the absorption of the microwaves cause a change in the permeability of the sample through a perturbation of the magnetic susceptibility M,

$$\mu_r(\omega) = \mu_0(1 + M) = \mu_0(1 + 4\pi\eta\chi(\omega)), \tag{2.33}$$

where η is the filling factor from Eqn. 2.21 which describes the flux-linkage efficiency between the applied microwave magnetic field and the sample and $\chi(\omega)$ is the complex time-dependant magnetic susceptibility.[2.27] For a simple Lorenzian-shaped spectrum, the magnetic susceptibility is

$$\chi(\omega) = \frac{(\omega_0 - \omega)T_1}{1 + (\omega_0 - \omega)^2T_2^2 + \gamma^2B_{1r}T_1T_2} - i\frac{1}{1 + (\omega_0 - \omega)^2T_2^2 + \gamma^2B_{1r}T_1T_2}, \tag{2.34}$$

where T_1 and T_2 are the spin-spin and spin-lattice relaxation times, respectively, ω_0 is the frequency of resonance as ω is swept, B_{1r} is the microwave magnetic field perpendicular to $\mathbf{B}_0$ (Eqn. 2.23 and γ is an isotropic gyromagnetic ratio.[2.2]

Assuming a simple lumped-circuit resonance consisting of an inductor L_R (which contains the sample) in series with a resistor R_R in parallel with a capacitance C_R. The capacitor is chosen so the tank circuit resonates at the frequency $\omega_R^2L_RC_R = 1$. The detector is placed across the capacitor, measuring the voltage.

The inductance can be described by

$$L_R = \mu_rL_0 = \mu_0(1 + M)L_0 = \mu_0(1 + 4\pi\eta\chi)L_0, \tag{2.35}$$

where the permeability of the sample consists of the freespace μ_0 and $4\pi\chi$ is the magnetic susceptibility M, modified by the filling factor η.[2.23] Although χ is a function of the incident microwave frequency $\chi(\omega)$, it is omitted for brevity. The resonant tank-circuit resistance and inductance can be further simplified such that

$$R_R + i\omega L_R = (R_R + 4\pi\omega L_0\eta\chi'') + i(1 + 4\pi\eta\chi')\omega L_0 \tag{2.36}$$

where ω is the frequency of operation and resonance occurs in the neighborhood of $(\omega_0 - \omega)^2$.[2.27] The change in magnetic permeability within a resonator is small compared to the microwave inductance and causes only a perturbation in the operating frequency (dispersion; χ') and losses (absorption; χ''). The resonator impedance is matched to the bridge, called "critical coupling", where the interference of the incoming standing-wave voltage cancels the outgoing reflections. At critical coupling, no voltage is detected at

[3] In order to relate this to a real spectrum, we say this happens "in the neighborhood" of resonance ω_0 and assume the linewidth is caused by a general broadening from the spin-spin relaxation time. This assumes homogeneous broadening, as opposed to inhomogeneous broadening. For example, broadening from hyperfine interactions, environmental deviations, etc.

the diode. However, in the neighborhood of resonance, the change in the tank-circuit resistance is directly measured as a change in the reflection coefficient.

In the CW experiment, the static magnetic field is modulated by $B_0 + B_m \mathrm{Cos}[2\pi f_m t]$, typically at a modulation frequency f_m of 100 kHz, and is collected using a phase-sensitive detector.[2.10] If the modulation is small, the signal is derivative-like.[2.28] As the modulation amplitude B_m is increased, the signal increases proportionally until the modulation amplitude approaches the intrinsic line-width of the sample where a broadening occurs. Choosing between signal and signal purity is known as the line-height–line-width compromise and is discussed in Ref. [2.29].

The modulated reflection coefficient changes are recorded on a detector diode connected to the phase-sensitive detector. When the frequency is held constant, as is typically done with automatic frequency control (AFC), an absorption spectrum is obtained.[2.30] A dispersion signal can be obtained by the frequency control feedback voltage or directly detected by a quadrature microwave channel. Continuous-wave is the standard EPR experiment.

Non-adiabatic and Adiabatic Rapid Scan.

With modern digital signal processing and fast analog-to-digital converters, the CW experiment has recently been improved upon. The non-adiabatic rapid scan (NARS)[2.31–35] and adiabatic rapid scan (RS)[2.36–40] methods collect real and imaginary EPR spectra (pure-absorption and pure-dispersion) using magnetic field ($\mathbf{B}_0 + \mathbf{B}_m$) or microwave frequency sweeps without the need for a phase-sensitive detector. Both rapid scan methods produce data that can be post-processed with pseudo-modulation to compare to the conventional first-derivative EPR spectrum using a moving difference (MDIFF) pseudo-modulation.[2.34] The non-adiabatic rapid scan (NARS) experiment uses a static field sweep fast enough to overcome $1/f$ noise but remains in thermal equilibrium (slow passage), while adiabatic rapid scan sweeps the static field fast enough that the spin system does not return to thermal equilibrium before it is excited again (rapid passage).[2.41]

Specifically, the rapid passage regime satisfies the equation

$$\frac{|\mathbf{B}_{1r}|}{dB_0/dt} \ll \sqrt{T_1 T_2} \tag{2.37}$$

where the magnitude of the magnitude microwave magnetic field $\mathbf{B}_{1r}$, as previously defined in Eqn. 2.23, and the change in static magnetic field B_0 must be much less than the geometric mean of the spin-lattice relaxation time T_1 and spin-spin relaxation time T_2. The adiabatic regime is defined as

$$\gamma |\mathbf{B}_{1r}|^2 \gg \frac{dB_0}{dt}, \tag{2.38}$$

where γ is the the gyromagnetic ratio in MHz/mT. Conversely, the non-adiabatic regime is defined as

$$\gamma |\mathbf{B}_{1r}|^2 \ll \frac{dB_0}{dt}. \tag{2.39}$$

These conditions are defined in Weger's work on passage effects and define the shape of the EPR signal.[2.41]

The advantage of the non-adiabatic rapid scan experiment is the signal-to-noise improvement of collecting pure-absorption EPR spectra, while adiabatic rapid scan can further improve the continuous-wave and NARS experiment by changing the effective microwave magnetic field at the sample. This allows for an increase of microwave power,

and thus, an increase in EPR signal for saturable signals.[2.36] It should be noted that the excitation of a spin packet goes through a continuum of passage from the steady-state CW experiment to the non-adiabatic rapid scan to adiabatic rapid scan, and finally to the free-induction decay pulse.

While the non-adiabatic rapid scan method can be implemented on commercial pulse bridges with no hardware changes, it does require some technical expertise.[2.40] However, to perform adiabatic rapid scan experiments on protein samples, custom current drivers are needed to increase the swept field amplitude. For simplicity, in this work, only the non-adiabatic rapid scan experiment has been implemented.

Electron Spin Echo Pulse.

The field-swept two-pulse electron spin-echo (ESE) experiment uses a $\pi/2-\tau-\pi$ pulse sequence. A $\pi/2$-pulse is defined as enough microwave power to tip the magnetization of a spin packet into the M_x-M_y plane. Such a pulse is applied Over a time τ, the magnetization dephases into the x-y-plane, where an applied π-pulse inverts the magnetization. After τ seconds the spin packet becomes coherent and an echo is formed. The echo is recorded, where the intensity is a function of the magnetic susceptibility absorption χ'' (Eqn. 2.34) interacting with the resonator. The echo is proportional to the absorption of the spins at a single static field position. The static field is stepped and a whole spectrum is acquired.[2.42] For systems with little nuclei interaction, the ESE experiment will mimic the pure absorption spectrum of the CW experiment. This is the standard pulse sequence to collect an EPR spectrum, and the pulse sequence is illustrated in Fig. 2.4.

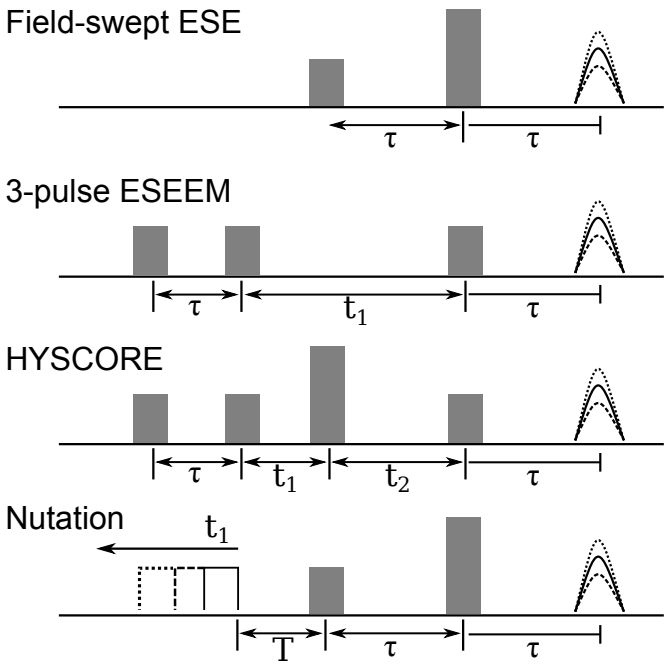

Figure 2.4.: The pulse EPR sequences used in this work. Field-swept electron spin echo (ESE) is performed over a series of field steps, recording the entire spectrum. Electron Spin Echo Envelope Modulation (ESEEM) and Hyperfine Sublevel Correlation (HYSCORE) are performed at a single field position. The nutation experiment is used in this work to determine the efficiency parameter Λ_{ave}.

Specifically, the signal from a microwave pulse is derived from the reciprocity principle of electromagnetics.[2.43] The initial magnitude of the magnetization can be described as $\mathbf{M} = M_0\mathbf{B}_z$, where M_0 is the dc bulk magnetization. When $\mathbf{B}_{1r}$ is applied, the bulk magnetization takes the form of the magnetic susceptibility of Eqn. 2.34. If the excitation coil is the same as the pickup coil, after a $\pi/2$-pulse is applied, and electromotive force (emf) is induced on the coil such that

$$\xi = -\int \frac{\partial \mathbf{B}_{1r} \cdot \mathbf{M}}{\partial t} dV_s, \tag{2.40}$$

which is transferred to a voltage across the tank-circuit capacitance. The voltage, assuming a homogeneous $\mathbf{B}_{1r}$ and a unit volume, is such that

$$V_0 = -4\pi\eta \int \frac{\partial \mathbf{B}_{1r} \cdot \mathbf{M}}{\partial t} dV_s = -4\pi\eta \frac{\partial \phi}{\partial t}, \tag{2.41}$$

where $\partial\phi/\partial t$ is the time-varying magnetic flux, which includes the permeability defined in Eqn. 2.33.[2.27, 2.43, 2.44] The final output to the receiver is multiplied by the Q-value of the tank circuit, which transforms the voltage proportional to the stored energy of the circuit.[2.23] The formulation of V_0Q can be related directly to the parameters defined by Feher in Eqn. 2.18, where the applied microwave magnetic field is held constant in order to provide a $\pi/2$-pulse, as defined by the saturable signal conditions of Eqn. 2.28.

The voltage V_0 decays exponentially with the spin-lattice relaxation time T_2 and, within the decay envelope, exists the magnetization dephasing from the x-y-plane. The signal directly after a $\pi/2$-pulse is known as the free induction decay (FID) and it is this dephasing that is refocused after time τ to form the echo in the ESE experiment. Therefore, the experimental parameter τ must be chosen to allow for sufficient ring-down of the tank-circuit, but not so long as the signal V_0 has decayed beyond detection.

ESEEM and HYSCORE.

The Electron spin echo envelope modulation (ESEEM) experiment has a pulse sequence of $\pi/2-\tau-\pi/2-t_1-\pi/2$. The three-pulse variation of ESEEM (3P-ESEEM) pulse sequence is illustrated in Fig. 2.4. ESEEM is capable of resolving hyperfine and quadrupole interactions of the electron to neighboring nuclei. It is complementary to electron-nuclear double resonance experiments (ENDOR).[2.3, 2.7, 2.8, 2.42]

The 3P-ESEEM signal used in this work arises from the semi-forbidden transitions between the different M_s manifolds ($\pm|\frac{1}{2}\rangle$; Fig. 2.1), but within the same M_I manifold. This nuclear coherence mixing is directly probed by the dephasing that is occurring at time τ which is allowed to mix for time t_1.

Unlike the two-pulse ESEEM signal, the 3P-ESEEM does not obtain the sum and differences of the modulating frequencies, potentially simplifying analysis. However, a drawback of the 3P-ESEEM method is the dependence of the signal on the τ chosen. Known as "τ-suppression" occurs because of the time at which the coherence mixing $\pi/2$-pulse starts could be at a null of the nuclear modulation frequency.[2.42] This effect can be minimized by summing a series of 3P-ESEEM measurements at different τ values.

Two regimes of hyperfine coupling exist, denoted as strong $a_{iso}/2 < \nu_n$ and weak $a_{iso}/2 > \nu_n$ coupling, depicted in the bottom-right inset of Fig. 2.1. The modulating resonance frequency ν_n is related to the nuclei by the nuclear Zeeman energy $-g_n\beta_nB_0/\hbar$. The tensor information is directly observed from the summation of the hyperfine and quadrupole interactions of Eqns. 2.3 and 2.5. Using an ESEEM experiments, the modulation frequencies $2\nu_n \pm 3P_z$ for strong coupling and $a_{iso} \pm 3P_z$ for weak coupling (Fig. 2.1

d, **e**, **f**, **g**) are directly observed. In addition, the double-quantum peaks (Fig. 2.1 **h**, **i**) are observed at the frequencies $\nu^D Q_{\alpha,\beta}$ described by Eqn. 2.8. The modulation depth observed in the time-domain trace is dictated by

$$k(\theta) = \mathrm{Sin}^2(2\theta) = \left(\frac{B_\theta}{\nu_I}\nu_\alpha\nu_\beta\right)^2 \tag{2.42}$$

where θ is the angle between the non-isotropic electron-nuclear hyperfine tensor $\mathbf{T}$ of Eqn. 2.4 and the static magnetic field $\mathbf{B}_z$. When either $\mathbf{T}$ is zero or $\mathbf{B}_z$ is aligned with a principal axis, the modulation depth is reduced to zero.

The hyperfine sublevel correlation (HYSCORE) experiments add an additional pulse to the 3-Pulse ESEEM. A $\pi/2-\tau-\pi/2-t_1-\pi-t_2-\pi/2$ pulse sequence results in an echo τ seconds after the last $\pi/2$ pulse. The values for t_1 and t_2 are swept to form a 2D experiment at a fixed static magnetic field position. The HYSCORE experiment allows for the separation of overlapping modulation frequencies found in large anisotropic hyperfine systems. Additionally, HYSCORE separates the strong $a_{iso}/2 < \nu_n$ and weak $a_{iso}/2 > \nu_n$ coupling regimes into the (−,+) quadrant and (+,+), respectively. The use of HYSCORE allows for a visual representation of the different modulating frequencies such that the ν_n or $a_{iso}/2$ can be read directly from the graph.

Although HYSCORE is a useful tool for visualization and human-aided analysis, a set of ESEEM spectra are typically simulated for fitting and following orientation dependant single crystal data to obtain the full hyperfine-tensor.[2.45]

Nutation.

The nutation experiment is performed at a field position of maximum EPR signal and a perturbation pulse is added to the electron spin-echo experiment such that a pulse sequence of t_1-pulse$-\mathrm{T}-\pi/2-\tau-\pi$ if formed. The t_1-pulse is varied resulting in a perturbation on the electron spin echo experiment at a fixed field. The variation is a function of the tip angle of the spin-system and can be related to the microwave magnetic field $\mathbf{B}_1$ incident on the sample. In resonators with inhomogeneous fields, the average of $\mathbf{B}_{1r}$ is measured and is directly comparable to Λ_{ave} of Eqn. 2.31.

The Rabi oscillation frequency f_{rab} produced in a nutation experiment can be determined by

$$f_{rab} = \frac{\gamma B_{1r}}{2\pi}, \tag{2.43}$$

where γ is the gyromagnetic ratio and B_{1r} is the magnetic flux density incident on a sample. If the incident $\mathbf{B}_{1r}$ was homogeneous, a single frequency would be produced. However, for cavities with non-uniform $\mathbf{B}_{1r}$ a distribution of frequencies is generated and can be assessed by the Fourier transform of the Rabi oscillations.

CHAPTER 2. REFERENCES

[2.1] M. Levitt, Spin Dynamics: Basics of Nuclear Magnetic Resonance, Wiley, 2008.

[2.2] A. Abragam, The Principles of Nuclear Magnetism, Clarendon Press, 1961.

[2.3] G. E. Cutsail, J. Telser, B. M. Hoffman, Advanced paramagnetic resonance spectroscopies of iron–sulfur proteins: Electron nuclear double resonance (ENDOR) and electron spin echo envelope modulation (ESEEM), Biochim. Biophys. Acta - Mol. Cell Res. 1853 (6) (2015) 1370–1394.

[2.4] A. Abragam, B. Bleaney, Electron Paramagnetic Resonance of Transition Ions, Oxford Press, 2012.

[2.5] J. Harriman, Theoretical Foundations of Electron Spin Resonance, Academic Press, 1978.

[2.6] J. Griffith, The Theory of Transition-Metal Ions, Cambridge University Press, 1964.

[2.7] S. Van Doorslaer, E. Vinck, The strength of EPR and ENDOR techniques in revealing structure–function relationships in metalloproteins, Phys. Chem. Chem. Phys. 9 (2007) 4620–4638.

[2.8] J. Harmer, G. Mitrikas, A. Schweiger, Advanced Pulse EPR Methods for the Characterization of Metalloproteins.

[2.9] C. H. Townes, B. P. Dailey, Determination of electronic structure of molecules from nuclear quadrupole effects, J. Chem. Phys. 17 (9) (1949) 782–796.

[2.10] J. Weil, J. Bolton, Electron Paramagnetic Resonance: Elementary theory and Practical Applications, Wiley, 2007.

[2.11] A.-L. Barra, L.-C. Brunel, D. Gatteschi, L. Pardi, R. Sessoli, High-frequency EPR spectroscopy of large metal ion clusters: From zero field splitting to quantum tunneling of the magnetization, Accounts of Chem. Research 31 (8) (1998) 460–466.

[2.12] J. Nehrkorn, B. M. Martins, K. Holldack, S. Stoll, H. Dobbek, R. Bittl, A. Schnegg, Zero-field splittings in metHb and metMb with aquo and fluoro ligands: A FD-FT THz-EPR study, Mol. Phys. 111 (18-19) (2013) 2696–2707.

[2.13] J. Jackson, Classical Electrodynamics, Wiley, 1975.

[2.14] J. Esselborn, N. Muraki, K. Klein, V. Engelbrecht, N. Metzler-Nolte, U.-P. Apfel, E. Hofmann, G. Kurisu, T. Happe, A structural view of synthetic cofactor integration into [FeFe]-hydrogenases, Chem. Sci. 7 (2016) 959–968.

[2.15] S. Stoll, A. Schweiger, EasySpin, a comprehensive software package for spectral simulation and analysis in epr, J. Magn. Reson. 178 (1) (2006) 42–55.

[2.16] S. Hovmöller, C. Taylor, Rotation Matrices and Translation Vectors in Crystallography, University College Cardiff Press, 1981.

[2.17] T. L. Blundell, L. N. Johnson, Protein Crystallography, Academic Press, 1976.

[2.18] S. Kriminski, C. L. Caylor, M. C. Nonato, K. D. Finkelstein, R. E. Thorne, Flash-cooling and annealing of protein crystals, Acta Cryst. D 58 (3) (2002) 459–471.

[2.19] M. Sadiku, Numerical Techniques in Electromagnetics, Second Edition, Taylor & Francis, 2000.

[2.20] J. Jin, The Finite Element Method in Electromagnetics, Wiley, 2015.

[2.21] J. S. Hyde, J. W. Sidabras, R. R. Mett, Resonators for multifrequency EPR of spin labels, in: S. K. Misra (Ed.), Multifrequency Electron Paramagnetic Resonance: Theory and Applications, Wiley-VCH Verlag GmbH & Co. KGaA, 2011, Ch. 5.2, pp. 244–269.

[2.22] G. Feher, Sensitivity considerations in microwave paramagnetic resonance absorption techniques, Bell Syst. Tech. J. 36 (2) (1957) 449–484.

[2.23] S. Ramo, J. Whinnery, T. Van Duzer, Fields and Waves in Communication Electronics, Wiley, 1984.

[2.24] R. Harrington, Time-harmonic Electromagnetic Fields, McGraw-Hill, 1961.

[2.25] J. S. Hyde, W. Froncisz, Loop-gap resonators, in: A. J. Hoff (Ed.), Advanced EPR: Applications in Biology and Biochemistry, Elsevier, 1989, pp. 277–306.

[2.26] J. W. Sidabras, T. Sarna, R. R. Mett, J. S. Hyde, Uniform field loop-gap resonator and rectangular TE_{U02} for aqueous sample EPR at 94 GHz, J. Magn. Reson. 282 (2017) 129–135.

[2.27] R. Schumacher, Introduction to Magnetic Resonance: Principles and Applications, W. A. Benjamin, 1970.

[2.28] J. S. Hyde, M. Pasenkiewicz-Gierula, A. Jesmanowicz, W. E. Antholine, Pseudo field modulation in EPR spectroscopy, Appl. Magn. Reson. 1 (3) (1990) 483.

[2.29] G. Eaton, S. Eaton, D. Barr, R. Weber, Quantitative EPR, Springer Vienna, 2010.

[2.30] C. Poole, Electron Spin Resonance: a Comprehensive Treatise On Experimental Techniques, Interscience Publishers, 1967.

[2.31] A. W. Kittell, theodore G. Camenisch, J. J. Ratke, J. W. Sidabras, J. S. Hyde, Detection of undistorted continuous wave (CW) electron paramagnetic resonance (EPR) spectra with non-adiabatic rapid sweep (NARS) of the magnetic field, J. Magn. Reson. 211 (2) (2011) 228–233.

[2.32] A. W. Kittell, E. J. Hustedt, J. S. Hyde, Inter-spin distance determination using L-band (1–2 GHz) non-adiabatic rapid sweep electron paramagnetic resonance (NARS EPR), J. Magn. Reson. 221 (2012) 51–56.

[2.33] A. W. Kittell, J. S. Hyde, Spin-label CW microwave power saturation and rapid passage with triangular non-adiabatic rapid sweep (NARS) and adiabatic rapid passage (ARP) EPR spectroscopy, J. Magn. Reson. 255 (2015) 68–76.

[2.34] J. S. Hyde, B. Bennett, A. W. Kittell, J. M. Kowalski, J. W. Sidabras, Moving difference (MDIFF) non-adiabatic rapid sweep (NARS) EPR of copper(II), J. Magn. Reson. 236 (11) (2013) 15–25.

[2.35] Z. Yu, T. Liu, H. Elajaili, G. A. Rinard, S. S. Eaton, G. R. Eaton, Field-stepped direct detection electron paramagnetic resonance, J. Magn. Reson. 258 (2015) 58–64.

[2.36] J. P. Joshi, J. R. Ballard, G. A. Rinard, R. W. Quine, S. S. Eaton, G. R. Eaton, Rapid-scan EPR with triangular scans and fourier deconvolution to recover the slow-scan spectrum, J. Magn. Reson. 175 (1) (2005) 44–51.

[2.37] M. Tseitlin, T. Czechowski, R. W. Quine, S. S. Eaton, G. R. Eaton, Background removal procedure for rapid scan EPR, J. Magn. Reson. 196 (1) (2009) 48–53.

[2.38] D. G. Mitchell, R. W. Quine, M. Tseitlin, S. S. Eaton, G. R. Eaton, X-band rapid-scan EPR of nitroxyl radicals, J. Magn. Reson. 214 (2012) 221–226.

[2.39] D. G. Mitchell, M. Tseitlin, R. W. Quine, V. Meyer, M. E. Newton, A. Schnegg, B. George, S. S. Eaton, G. R. Eaton, X-band rapid-scan EPR of samples with long electron spin relaxation times: A comparison of continuous wave, pulse and rapid-scan EPR, Mol. Phys. 111 (18-19) (2013) 2664–2673.

[2.40] J. Möser and K. Lips and M. Tseytlin and G.R. Eaton and S.S. Eaton and A. Schnegg, Using rapid-scan EPR to improve the detection limit of quantitative EPR by more than one order of magnitude, J. Magn. Reson. 281 (2017) 17–25.

[2.41] M. Weger, Passage effects in paramagnetic resonance experiments, Bell Labs Tech. J. 39 (4) (1960) 1013–1112.

[2.42] A. Schweiger, G. Jeschke, Principles of Pulse Electron Paramagnetic Resonance, Oxford University Press, 2001.

[2.43] D. Hoult, R. Richards, The signal-to-noise ratio of the nuclear magnetic resonance experiment, J. Magn. Reson. 213 (2) (2011) 329–343.

[2.44] C. Slichter, Principles of Magnetic Resonance, Springer Berlin Heidelberg, 1978.

[2.45] J. J. Shane, P. A. A. W. van der Heijden, E. J. Reijerse, E. de Boer, An ESEEM investigation of single crystals and powders of copper-dopedl-histidine hydrochloride monohydrate, App. Magn. Reson. 6 (3) (1994) 427–454.

3. Uniform Field Re-Entrant TE_{01U} Cavity at Q-band Frequencies.

With the introduction of uniform field (UF) resonators for Electron Paramagnetic Resonance (EPR) spectroscopy, a cavity can be designed to have a microwave magnetic flux (B_{1r}; Eqn. 2.23) uniform over a region-of-interest by the implementation of properly designed end sections.[3.1–4] Most importantly, the region-of-interest is not limited by the wavelength; allowing for larger sample volumes to increase the concentration sensitivity of the resonator. However, as the length of the region-of-interest is increased, the resonator efficiency is lowered due to the reduction of stored energy density within the cavity volume for a fixed input power. By extending the uniform field concept to loop-gap resonators,[3.5] it became possible to design resonators with both high efficiency and uniform field distributions.[3.6] Yet, as higher frequency loop-gap resonators (LGR) are designed, the sample loop diameter must be significantly reduced to lower inductance and/or the number of gaps must be increased to lower capacitance.[3.6–8] The sample loop diameter imposes a limit on the capillary size and sample volume, potentially limiting concentration sensitivity. This limit is not present in typical cavities, such as the cylindrical TE_{011} with a capillary sample, where a broad sample volume optimum exists.[3.9]

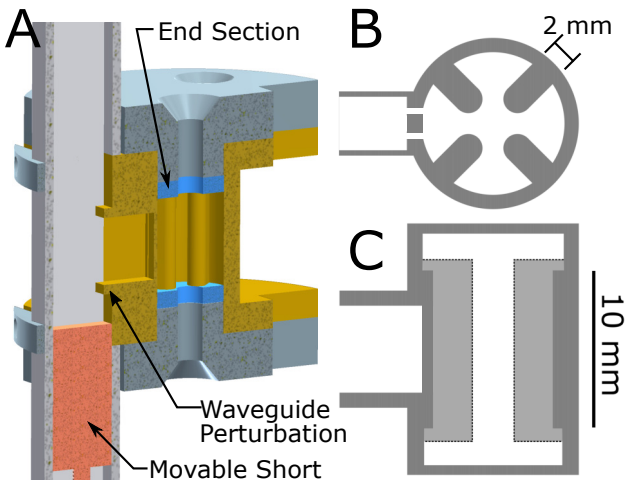

Figure 3.1.: A) Half-structure resonator assembly CAD drawing showing the brass resonator (gold), brass end plates (grey), Rexolite end-sections (blue), and copper waveguide (light grey). The waveguide H-type T-junction coupler with inductive obstacles (waveguide perturbation) and brass movable short is also illustrated. The re-entrant geometry is further detailed in B) the top view, showing the re-entrant fins and dual-slot iris, and C) the side view, showing the 10 mm uniform field region-of-interest.

One solution to increase the stored energy density in a UF TE_{01U} is to place a dielectric insert into the cavity. A simulated design of a dielectric UF cavity at X-band frequencies (9.5 GHz) was introduced by Mett *et al.* as a way to increase EPR sensitivity without

A significant portion of this chapter is from J. W. Sidabras, E. J. Reijerse, W. Lubitz, Appl. Magn. Reson. 48 (11) (2017) 1301–1314. and is reproduced under the CC-BY license.

creating an overly-large cavity.[3.10] The use of dielectric tubes improves the stored energy density in the region-of-interest but may exhibit significant frequency dependence with different experimental temperatures.[3.11] This temperature dependence limits the versatility of a UF cavity.

In this work, a UF re-entrant cylindrical TE_{01U} cavity at Q-band frequencies (34 GHz) for pulse EPR spectroscopy is introduced, illustrated in Fig. 3.1. Re-entrant geometries are defined as waveguide structures where perturbations are placed in regions of a large electric field to lower the cut-off frequency of the waveguide and increase the stored energy density of the cavity.[3.12, 3.13] In a cylindrical waveguide, for a fixed cut-off frequency, the diameter of the waveguide is decreased as the re-entrant perturbations are extended into the electric field. If a re-entrant cavity is made by placing a shorted top/bottom on the waveguide and the resonant frequency is held constant, the stored energy density of the cavity would increase as the re-entrant perturbations are increased. When sufficiently close, the re-entrant perturbations behave like plate capacitors. An LGR can be considered a highly re-entrant waveguide operating at cut-off. It is the geometric space between cavities and LGRs that the re-entrant geometry explores.

In the present design, four 2 mm re-entrant fins were extended into a UF cylindrical TE_{01U} cavity, shown in Fig. 3.1B, and the UF region-of-interest was elongated to 10 mm (λ_g for a TE_{01} mode is 10.2 mm), shown in Fig. 3.1C. This geometry provides an enhanced efficiency, increased EPR signal, and a uniform B_{1r} field along the sample volume.

In general, UF resonators exhibit several advantages compared to traditional cavities. Typically a cavity geometry has a cosine dependence of B_{1r} in the direction of propagation in the waveguide. With a UF resonator, a region-of-interest is designed to be uniform and can be extended beyond a half wavelength. Uniform field resonators (i) provide better quantitative measurements reducing the need to calibrate the resonator B_{1r} profile[3.14]; (ii) allow the region-of-interest to be extended to provide a larger sample volume, increasing the EPR concentration sensitivity; (iii) can perform reliable continuous-wave (CW) saturation studies[3.15] and more reliable T_1 measurements using saturation recovery; (iv) can be used in pulse experiments with the need for coherent pulses, such as ESEEM/HYSCORE, DEER[3.16] and ELDOR-detected NMR[3.17]); and (v) provides uniform excitation for arbitrary-waveform generator (AWG) shaped inversion pulses[3.18, 3.19] and frequency sweeps.[3.20]

Additionally, an H-type T-junction waveguide coupler with inductive obstacles was designed to couple from the transmission waveguide to the resonator, shown in Fig. 3.1A. The introduction of the inductive obstacles increases the dynamic range of a movable short coupler while reducing the frequency shift during matching. A dual-slot iris was employed to lower the stored energy density of the iris and minimize B_{1r} perturbations along the sample volume.[3.6]

The resonator assembly was fabricated and tested both on the bench and with EPR experiments. Experimental bench test measurements of the resonator characteristics are provided and compared to computer simulations. The B_1 profile was measured on the bench using the method of perturbing spheres. [1]

[1] The perturbing sphere methodology measures B_1 directly by measuring the difference in frequency as the sphere moves through the resonator. To measure the B_{1r}, an EPR experiment is needed. We assume the majority of the magnetic field vector is along the sample and B_{1r} is equivalent to B_1.

3.1. Methods

Finite-element simulations were performed on a Fujitsu workstation with dual eight-core Xeon E5-2640 2.60 GHz processors with 15 MB of L2 Cache per chip and 124 GB of system DDR4 RAM. A RAM drive was set up with 16 GB of RAM. The temporary directory and simulation files were stored in the RAM drive to reduce hard-drive bottlenecks. This system has been optimized for simulations with new versions of ANSYS (Canonsburg, PA, USA) High Frequency Structure Simulator (HFSS; v. 18.2) and can take advantage of all sixteen CPUs during finite-element modeling matrix solving. The operating system was Windows 7 64-bit. The eigenmode and driven-mode solvers were used and typical simulation times were 15 minutes. All simulations were performed around 34 GHz.

EPR signal intensity and resonator efficiency values (Λ_{max} Eqn. 2.30; Λ_{ave} Eqn. 2.31) were calculated using ANSYS HFSS[3.21] and tabulated for comparison with typical resonator geometries, such as the cylindrical TE_{011} cavity.[3.22] Two EPR signal conditions are calculated: signal unsaturable (Su; Eqn. 2.29) and signal saturable (Ss; Eqn. 2.28). A 2.8 mm OD and 1.8 mm ID quartz capillary with ice sample ($\epsilon_r = 3.17 - i0.0035$[3.23]) was used in the simulations.

After the resonator geometry was designed, it was transferred to the 3D CAD software tool AutoDesk Inventor Professional, where the manufacturing details and geometric dimensions and tolerances were added. The model makers at the Max Planck Institutes for Chemical Energy Conversion and Kohlenforschung (Mülheim, Germany) performed the fine-mechanics tooling and die-sink electric discharge machining (EDM) manufacturing needed to fabricate the assembly. The prototype UF re-entrant cylindrical TE_{01U} cavity was fabricated from brass for the resonator body and end-caps. The end-sections were manufactured out of Rexolite plastic.[2]

Resonator characteristics, such as the frequency measurements, Q_0-value, over-coupling profiles, and sample frequency shifts, were performed on an Agilent 8722ES (now Keysight Technologies; Santa Rosa, CA, USA) vector network analyzer. A 2.8 mm OD and 1.8 mm ID quartz capillary (Vitrocom; Mountain Lakes, NJ, USA) was filled with polystyrene (PS) and a small (0.5 mm diameter) metallic probe was used as the test sample for the method of perturbing spheres. The method of perturbing spheres measures the increase in the microwave frequency as the metallic probe is stepped through the cavity volume. The size of the metallic sphere was chosen so the overall frequency shift was less than 100 MHz.

To further test the B_{1r} field uniformity, a nutation experiment was performed on a Bruker E580 spectrometer with a home-built transceiver accessory operating at Q-band with 10 W of total incident power available. The nutation experiment consists of an initial preparation pulse of varying length (τ_n), fixed delay (t_1 of 5000 ns), and a two-pulse detection. The pulse length τ_n was stepped by 4 ns over 2048 steps and a two-pulse detection echo was recorded.[3.16] The two-pulse detection echo was configured with a 60 ns and 120 ns pulse with a delay t_2 of 300 ns. The scheme is shown in Fig. 2.4. The sample consisted of 0.1% α,γ-Bisdiphenylene-β-phenylallyl (BDPA) by weight in polystyrene (PS) and was placed in a 2.8 mm OD and 1.8 mm ID quartz capillary. Two samples were used: The first sample geometry extended the entire length of the cylindrical TE_{011} and re-entrant TE_{01U} cavity length. The second sample geometry was

[2]Geometric STL files are provided at the Act-EPR website: *http://www.act-epr.org/data.*

a 9.5 mm sample to place in the 10 mm region-of-interest of the UF re-entrant TE_{01U} cavity.

3.2. Uniform Field Design

General Design Principles.

Advances in UF resonator design have been recently reviewed.[3.24] In this section, the underlying understanding behind uniform field resonators will be described.

Here, the cylindrical waveguide is introduced where the two-dimensional wave equation describes the transverse electric (TE) modes that propagate along the $\pm z$-direction, such that

$$(\bigtriangledown_t^2 + \beta_{mn}^2)\mathbf{H}_z = 0, \tag{3.1}$$

where $\bigtriangledown_t^2$ is the time-independent Laplacian and β_{mn}^2 is the wavenumber. The microwave magnetic field $\mathbf{H}_z$ is set by the scalar solution of the transverse components in the ρ and ϕ coordinates for a time-varying electromagnetic field $e^{-i\omega t}$. Illustrated in Fig. 3.2 is a cylindrical waveguide with a radius of a, and the propagation constant can be expressed as a function of the roots of the derivative of the Bessel function of the first kind, such that

$$\beta_{mn}^2 = \beta_0^2 - \beta_\rho^2 = \beta_0^2 - \left(\frac{J'_{mn}}{a}\right)^2, \tag{3.2}$$

where J'_{mn} is the n-th zero in the first-derivative of the Bessel function $J_m(x)$ and β_0 is the free-space propagation constant $\omega\sqrt{\epsilon_r\mu_r}$. When β_{mn} is set to zero and solved for the frequency the "cut-off" condition can be calculated, such that

$$f_c = \frac{1}{2\pi\sqrt{\epsilon_r\mu_r}}\frac{J'_{mn}}{a} \qquad \text{[Hz]}. \tag{3.3}$$

For the TE_{01} mode, the J'_{01} is approximately 3.832. For simplicity, it is assumed that there is no perturbation from the coupling iris. When the operating frequency f is greater than f_c and the waveguide is infinitely long, the electromagnetic wave will propagate,

$$\mathbf{H}_z = e^{\pm i\beta_{01}z}, \tag{3.4}$$

in the $\pm z$-direction and the wavelength in the waveguide λ_g is

$$\lambda_g = \frac{2\pi}{\beta_0\sqrt{1-(f_c/f)^2}} \qquad \text{[m]}. \tag{3.5}$$

This is illustrated in Fig. 3.2A as the magnitude of the microwave magnetic field ($H_1 = |\mathbf{H}_z|$) plotted along the axis of the geometry. As the operating frequency increases the propagating wavelength approaches the free-space wavelength.[3.25]

By adding end caps to a waveguide a boundary condition is imposed on the TE_{01} propagating mode which forces the tangential electric field to zero. The boundary condition results in a cosine dependence of the H_1 (equivalently B_{1r} along the sample in an EPR experiment) within the cavity, illustrated in Fig. 3.2B. With proper dimensions, a TE_{011} cavity is formed. In EPR, a sample is placed in the maximum H_1 where the operating frequency (X-band, Q-band, etc) is the frequency of the cavity.

In the cylindrical waveguide, if the operating frequency f is below the cut-off frequency f_c, the propagation constant becomes imaginary. The wave no longer propagates and,

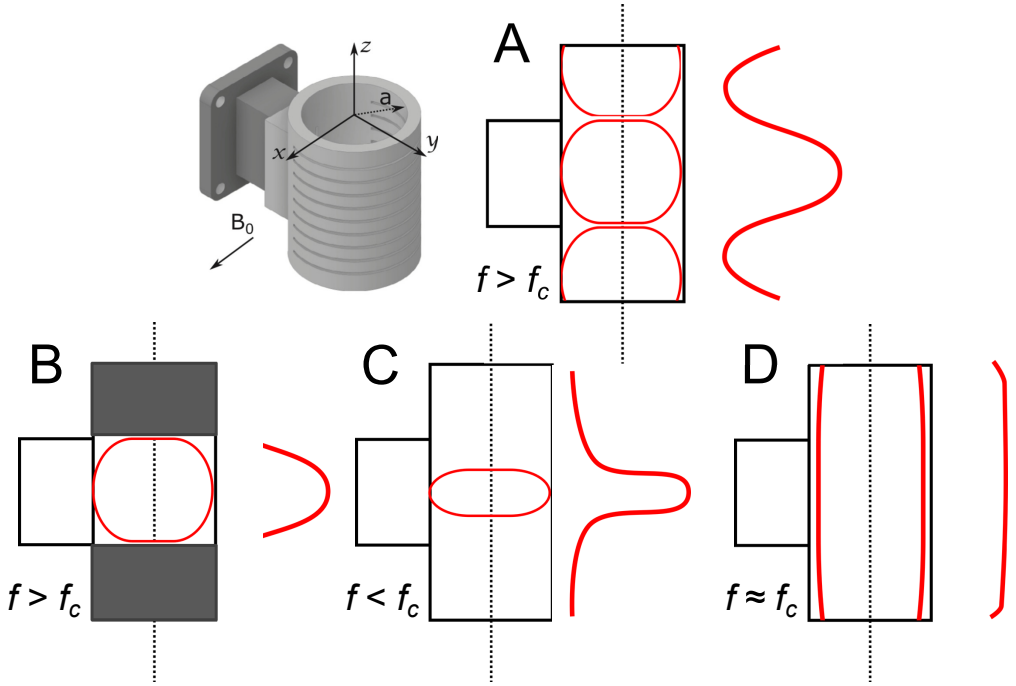

Figure 3.2.: Waveguide modes relative to the cut-off frequency. A cylindrical waveguide with a radius of a is coupled to a rectangular waveguide, geometry shown. The static magnetic field B_0 is indicated in the x-direction. A) When the operating frequency f is greater than the cut-off frequency f_c propagation occurs in the $\pm z$-direction. B) When conducting end caps are added, a cavity is created. C) If the operating frequency is less than the cut-off frequency ($f < f_c$) an evanescent mode is formed. D) When the operating frequency approaches the cut-off frequency ($f \approx f_c$) the wavelength becomes infinite, resulting in a uniform field.

instead, $\mathbf{H}_z$ of Eqn. 3.4 becomes evanescent with a reduction that is proportional to the propagation constant.

Of interest is when the operating frequency approaches the cut-off frequency ($f \approx f_c$). In this case, the wavelength approaches infinity as described by Eqn. 3.5. Under this condition is where uniform field resonators operate. Three characteristics describe the electromagnetic wave in the waveguide at cut-off. First, the wavelength is infinite and, assuming no dampening, the field is strictly uniform in the $\pm z$-direction for an infinitely-long waveguide. Second, the propagation constant is zero indicating no dispersion or phase velocity. This implies that a resonator with a uniform field active-region longer than a wavelength will not have a propagation time and the whole geometry will act as a single-mode cavity. Finally, a strictly uniform field in the waveguide occurs only when the operating frequency is at the cut-off frequency ($f = f_c$). Any deviation from this equality will result in either a bowed ($f > f_c$) or a concave ($f < f_c$) field profile.

The characteristic impedance of a cylindrical waveguide TE_{01} is defined by

$$Z_{01} = \frac{\beta_0 \sqrt{\mu_r/\epsilon_r}}{\beta_{01}} = \frac{\beta_0 \sqrt{\mu_r/\epsilon_r}}{\beta_0 \sqrt{1-(f_c/f)^2}} \qquad [\Omega] \tag{3.6}$$

and, therefore, when ($f = f_c$) the impedance approaches infinity. When the waveguide becomes a finite-length, the reflections from the open end-section causes the formation

of other modes which degrade the uniform field. If end sections are placed at fixed points along the z-axis, a TE_{01n} mode will form at a frequency dictated by the characteristic equation

$$\omega_{01n} = \frac{1}{\sqrt{\mu_r \epsilon_r}} \sqrt{\left(\frac{2\pi n}{h}\right)^2 + \left(\frac{J'_{01}}{a}\right)^2} \qquad \text{[rad/s]}, \tag{3.7}$$

where h is the height of the resonator and n is the number of half wavelengths that are formed.

To maintain the properties of the uniform field and to satisfy Maxwell's equations for a finite-length waveguide, the end sections must maintain an infinite characteristic impedance. An infinite characteristic impedance is likened to an "open" circuit. For a TE_{01} mode, the "open" circuit is a perfect-magnetic boundary condition. It is this condition must be matched to the central section.

Three matching methods were shown to produce this effect: i) over-sized end-sections above cut-off, ii) re-entrant metallic structures that add capacitance to the end-section, and iii) dielectric end-sections of length $\lambda/4$ placed at each shorted end. All end-section types present an rf open impedance boundary condition to the central cut-off section. These methods are illustrated in Fig. 3.3.

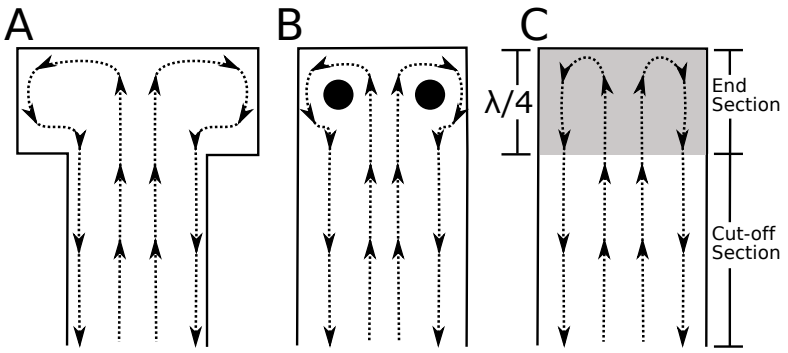

Figure 3.3.: Illustrations of three methods for creating uniform fields in cavities. Region-of-interest at cut-off is matched to A) an over-sized section, B) a re-entrant end-section with capacitive posts (black circles), C) a dielectric section of length $\lambda/4$ placed at a shorted end. Magnetic field vectors are illustrated with dotted lines.

Each method creates an end-section that transfers the characteristic impedance of a "short" to an "open". One drawback of the uniform field resonator is the frequency dependence of the whole structure. While designing a uniform field resonator, all perturbations must be accounted for, such as the sample, sample holder, end-section dielectrics, iris, and conductivity of the cavity walls. All factors modify the cut-off frequency and are taken into account within the finite-element modeling simulations. Typically uniform field resonators are designed for a range of samples where the non-uniformity is quantified within a dielectric constant range.

3.2.1. Re-Entrant TE_{01U} Cavity Design

The cylindrical TE_{011} cavity is a standard cavity for Q-band systems. The high Q_0-value and sample volume make it a good general-purpose resonator. However, for pulse experiments, the H_1 field variation is 50.9% over the cavity volume. The normalized H_1 field for a cylindrical TE_{011} cavity is shown in Fig. 3.4 as a dashed line. In a TE_{011}

cavity, when a 90- or 180-degree pulse is applied, a significant portion of the spins in the sample volume is either over or under excited.

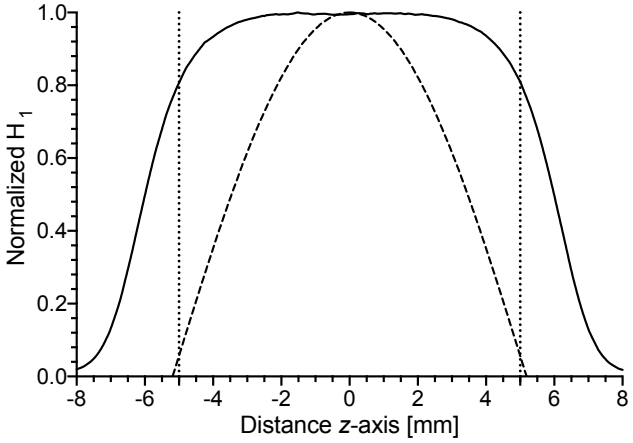

Figure 3.4.: Ansys HFSS simulation showing normalized magnetic field H_1 down the axis of the cylindrical re-entrant TE_{01U} (solid) compared to the magnetic field down the axis of the cylindrical TE_{011} cavity (dashed). Dotted lines mark the region-of-interest of the cylindrical re-entrant TE_{01U} cavity.

If a UF cylindrical TE_{01U} cavity was designed with oversized end-sections (Fig. 3.3A) and a region-of-interest of 10 mm, as described in Refs. [3.1] and [3.2], the H_1 variation over the cavity volume is reduced to 20%. However, the overall Λ_{max} is reduced by 39% compared to a TE_{011} cavity, due to the decrease in stored energy density in the entire cavity volume. The decrease in stored energy density is caused by the uniform field cavity being geometrically bigger. By introducing re-entrant fins, shown in Fig. 3.1B, where the electric field is concentrated, shown in 3.5A, results in a Λ_{max} decrease of 11% but an overall Λ_{ave} increase of 59.6%. The calculated resonator characteristics of the proposed UF re-entrant TE_{01U} cavity was compared to a TE_{011} and UF cylindrical TE_{01U} cavity with oversized end-sections are found in Table 3.1.

Table 3.1.: Ansys HFSS simulated resonator characteristics.

Geometry	Cyl. TE_{011} D/L=1	UF Cyl. TE_{01U}	UF TE_{01U} Re-Entrant
Frequency	34.3	34.5	34.1
Q_0-Value	13000	5900	1880
Signal, S_u	1	0.73	1.06
Signal, S_s	1	0.83	1.18
Λ_{max} [mT/W$^{1/2}$]	1.06	0.65	0.94
Λ_{ave} [mT/W$^{1/2}$]	0.52	0.52	0.83
ΔB_{1r}	50.9%	20%	11.7%

Using Ansys HFSS, a UF re-entrant TE_{01U} cavity was designed by the following procedure: (i) An eigenmode solution of the central section with a sample was simulated with a perfect magnetic field boundary condition. This provides the resonant frequency of the central section at cut-off with a sample. (ii) The region-of-interest was extended to 10 mm and Rexolite end sections were added to the simulation at a nominal height. (iii)

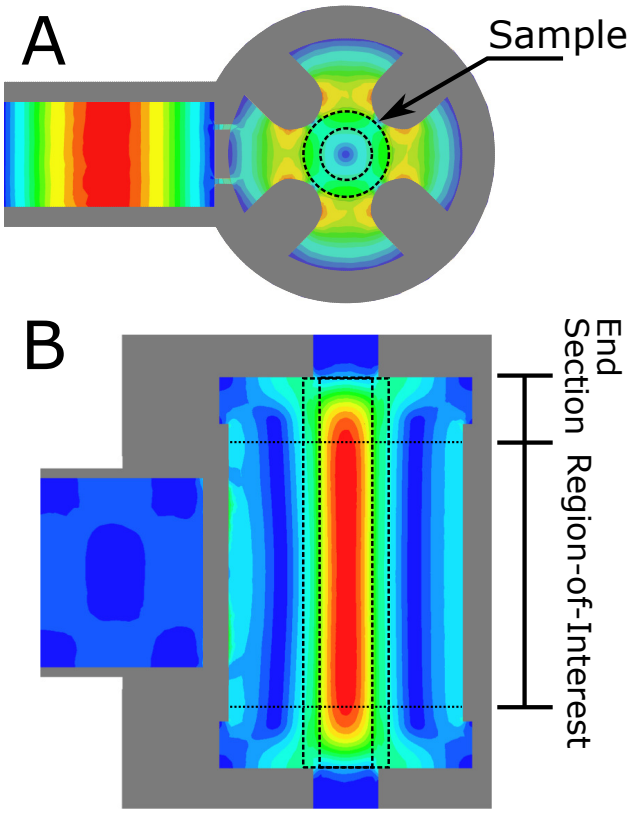

Figure 3.5.: Ansys HFSS simulation showing the magnitude of the microwave A) electric and B) magnetic fields of the uniform field re-entrant cylindrical TE_{01U} cavity. Each iris is 0.2 mm wide and extends over the entire waveguide length.

The end sections were varied until the eigenfrequency matches the cut-off frequency. (iv) An iris was introduced and the end sections are adjusted to accommodate the frequency shift. (v) Once completed, the resonator was imported into AutoDesk Inventor and prepared for fabrication.

By properly matching the end sections, a uniform H_1 field can be realized, illustrated in Figs. 3.5B. The normalized H_1 field profile is shown in Fig. 3.4 as a solid line. In the 10 mm region-of-interest, the simulated B_{1r} field profile was 98% uniform.

As shown in Fig. 3.1C, the re-entrant fins do not extend fully into the end section region. This design choice causes the end section to be electrically larger (shorter wavelength, λ_g) and reduces the end-section size needed to produce the matching criteria for the region-of-interest. As shown in Fig. 3.6, the roll-off in the current design is steeper compared to a TE_{01U} cavity with oversized end-sections designed from Fig. 3.3A. Decreasing the roll-off region of the resonator minimizes the sample volume that is excited by non-uniform fields.

3.2.2. Dual-Slot Iris Design

A dual-slot iris was designed to couple the UF re-entrant TE_{01U} cavity. The use of dual-slot iris reduces B_{1r} perturbations due to the stored energy density in the iris. For UF resonators, the dual iris also reduces coupling to higher-order modes that may exist because of the large length of the region-of-interest.[3.6] The size of a single capacitive

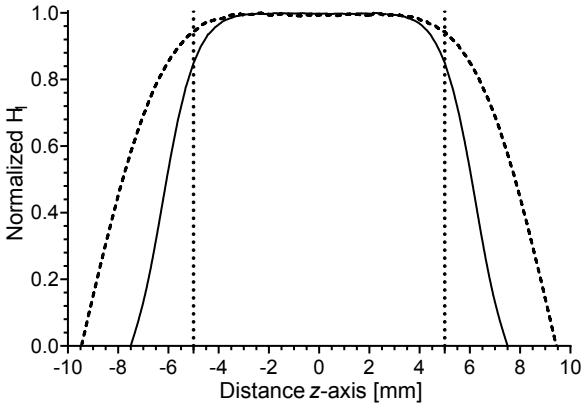

Figure 3.6.: Ansys HFSS simulation showing normalized H_1 field of the cylindrical re-entrant TE_{01U} (solid) compared to a TE_{01U} cavity with oversized end-sections depicted in Fig. 3.3A (dashed). Dotted lines mark the region-of-interest of the cylindrical re-entrant TE_{01U} cavity.

iris needed to couple the resonator was 0.45 mm. A dual-slot iris, each iris was 0.2 mm thick, was used to achieve the same coupling. The geometry is shown in Fig. 3.1A and 3.1C and the electric field profile in Fig. 3.5A.

3.3. Results

The Q_0-value of the UF cavity was measured to be 1330 with a distilled water ice sample at a frequency of 33.95 GHz. Additionally, the frequency shift of the re-entrant TE_{01U} cavity as the match was adjusted from critically coupled (-45 dB) to over-coupled (-9 dB) was 6.96 MHz, consistent with simulations of Fig. 3.8C.

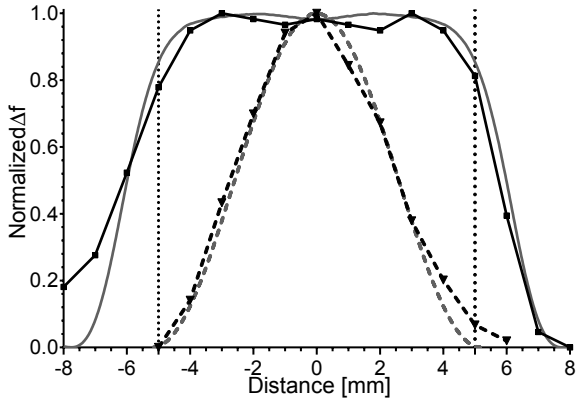

Figure 3.7.: Method of perturbing spheres showing the normalized Δf along the axis of the cylindrical re-entrant TE_{01U} (solid) compared to the cylindrical TE_{011} cavity. Dotted lines mark the region-of-interest of the cylindrical re-entrant TE_{01U} cavity. Comparison to Ansys HFSS simulations are shown in grey.

The change in frequency due to the presence of a small metallic probe is shown in Fig. 3.7. Measurements of the UF re-entrant TE_{01U} cavity are shown as a solid line and

match well with simulations. For comparison, measurements of the cylindrical TE_{011} are presented as a dashed line. The profiles here should be compared to the Ansys HFSS simulations of Fig. 3.4, shown as gray for convenience.

3.3.1. Waveguide H-type T-junction Coupler with Inductive Obstacles

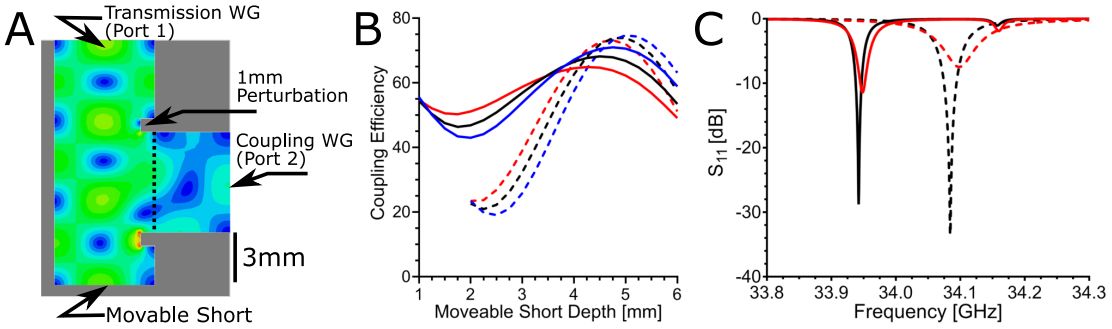

Figure 3.8.: A) Waveguide H-type T-junction coupler geometry with perturbations showing the transmission waveguide, coupling waveguide, and movable short. B) Ansys HFSS simulations showing the coupling efficiency without (solid) and with 1 mm perturbations (dashed) for three frequencies (33.5, 34, and 34.5 GHz, red, black, blue, respectively). C) Simulations showing the reflection coefficient S_{11} without (solid) and with 1 mm perturbations (dashed) at depths of 3.5 mm and 5 mm of the movable short (coupled and over-coupled; black and red). Operating frequency is 34.09 GHz.

For the resonator assembly to fit in a 40 mm diameter cryostat, an H-type T-junction coupler was implemented with a sliding short matching system. This sliding short impedance matching design is typical for a Q-band TE_{011} cavity and provides a robust coupling method for room temperature to sub-10 K measurements.[3.22] Typically coupling to a TE_{011} cavity is performed by introducing an iris to the H-plane sidewall of the transmission waveguide. However, due to the oversized end-sections, a coupling waveguide of 5.07 mm length is introduced perpendicular to the transmission waveguide, illustrated in Fig. 3.8A.

Three features describe an H-Type T-junction coupler: (i) The H-type T-junction coupler is similar to the H-arm of a magic-Tee coupler.[3.12, 3.13] (ii) The coupling waveguide was at least $\lambda_g/2$ in length. (iii) To maximize coupling, an "inductive obstacle" on the sub-wavelength H-type T-junction was introduced to the transmission waveguide. The "inductive obstacle", described by Ref [3.13] as a "Window Formed by One Obstacle", was introduced to the H-plane around the coupling waveguide and extends 1 mm into the transmission waveguide, illustrated in Fig. 3.8A. This inductive obstacle creates a favorable geometry for electric field coupling and increases coupling efficiency.

Plotted in Fig. 3.8B is the simulated coupling efficiency transmission can be calculated using an overlap integral[3.26] of the two electric fields. The overlap integral was calculated by

$$\eta = \frac{\left|\int E_t \cdot E_c^* dA\right|^2}{\int |E_t|^2 \, dA \int |E_c|^2 \, dA}, \tag{3.8}$$

where $E_t \cdot E_c^*$ represents the electric field coupling over the waveguide interface area

between the electric field of the transmission waveguide (E_t) and the coupling waveguide (E_c) at the interface area A, shown as a dotted line in Fig. 3.8A.

The coupling efficiency between port 1 at the transmission waveguide and port 2 at the coupling waveguide is shown in Fig. 3.8B, where the coupling efficiency without the waveguide perturbations (solid) and with 1 mm perturbations (dashed) is plotted. Three frequencies (33.5, 34, and 34.5 GHz, light grey, black, dark grey, respectively) were used to show the frequency dependence. Lower coupling efficiency under-couples the resonator. In simulation, the resonator was critically coupled when the movable short was around 3.5 mm depth at 34 GHz and maximum over-coupling occurs at 5 mm. The waveguide H-type T-junction coupler with the perturbation illustrates a more "dynamic range" in coupling for the same distance and a flatter response for maximum over-coupling with a 1 GHz frequency range. To produce the same coupling range without the waveguide perturbations the iris must be 25% larger. A larger iris leads to inhomogeneity of the H_1 field around the iris and in the region-of-interest.

The UF re-entrant TE_{01U} cavity was designed to be over-coupled. Shown in Fig. 3.8C is the effect of the movable short on the reflection coefficient S_{11} of the UF re-entrant TE_{01U} with a range of coupling positions (3.5 and 5 mm, coupled and over-coupled). The resonator microwave frequency shift with coupling is reduced form 14.4 MHz to 8.2 MHz using the H-type T-junction coupler with perturbations. Lower microwave frequency pulling occurs due to a reduction in the stored energy density in the region of the coupler.

Additionally, for the same resonator geometry, there was a 145 MHz shift in operating frequency from its eigenfrequency of 34.1 GHz due to the impedance of the coupler without the perturbations. The coupler without perturbations has more stored energy density and more reactance, consistent with the understanding of coupling systems with frequency dependence.[3.27] This causes a shift in the real part of the microwave frequency to compensate for the imaginary part of the assembly reactance and makes the assembly more frequency-dependent.

3.3.2. Experimental Results

Shown in Fig. 3.9 are the data from the nutation experiment. Dotted lines represent the center of the nutations, while dashed lines show 50% signal markers. The cylindrical TE_{011} cavity data was taken with the BDPA sample extending the entire cavity length and plotted in Fig. 3.9A. For a 120 ns π-pulse the power was set to 2.5 W. In Fig. 3.9B, the UF re-entrant TE_{01U} cavity with the BDPA sample extending the entire cavity length is shown. For a 120 ns π-pulse the power was set to 5 W. A second sample with 9.5 mm length was centered in the UF re-entrant TE_{01U} cavity region-of-interest. Experimental nutation data are plotted in Fig. 3.9C and for a 120 ns π-pulse the power was set to 5 W.

Nutation experiments show good results in terms of increased sensitivity and uniformity of the H_1 field. The nutations using the UF re-entrant TE_{01U} cavity with the sample extending the entire length show clear improvements over the data from the cylindrical TE_{011} cavity, shown in Fig. 3.9A and 3.9B, respectively.

The UF re-entrant TE_{01U} cavity with the 9.5 mm sample only in the region-of-interest, shown in Fig. 3.9C, show that the nutations were further extended and the initial off-set was further minimized. These data show the advantages of uniform field cavities. Three differences of note are: (i) The signal-to-noise ratio was improved by at least 40% and the initial offset was reduced by 50%. (ii) The first-order linear background subtraction was not adequate for the cylindrical TE_{011} cavity. A higher-order background exists

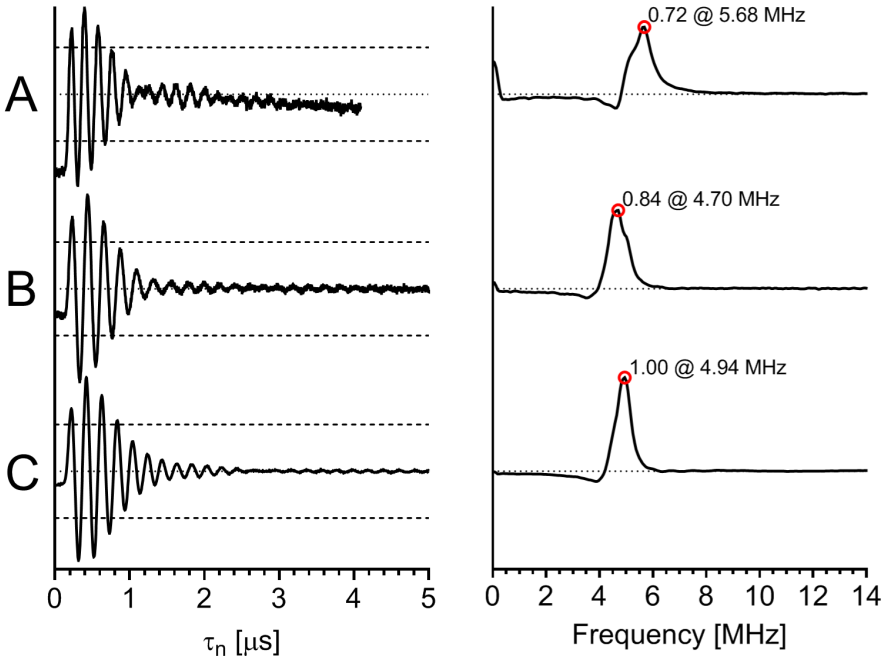

Figure 3.9.: Nutation experiment on a BDPA sample performed using the A) cylindrical TE_{011} cavity, the uniform field re-entrant TE_{01U} cavity B) with the sample extending the entire length and C) with a 9.5 mm sample centered in the region-of-interest. Pulse lengths were 120 ns for π-pulse and the preparation pulse length was stepped 4 ns. Dotted lines show the nutation center, while dashed lines show 50% signal markers. The real part of the Fourier transform of the nutation experiment is shown on the left with the peak amplitude and corresponding frequency marked.

that cannot be easily corrected. (iii) A nutation signal phase-inversion was exhibited in Fig. 3.9A at 1200 ns and another at 2400 ns, while only one inversion at 2800 ns was noticeable in Fig. 3.9B. This oscillatory phase-inversion has been experimentally determined to be due to inhomogeneity of B_{1r}, seemingly at the top and bottom of the resonator. The nutation signal phase-inversion was shown to be minimized in Fig. 3.9C, but can be deliberately increased by moving the sample outside of the region-of-interest.

Also shown in Fig. 3.9 is the real part of the Fourier transform of the data. In this display, the broadening of the peak is determined partly by the inhomogeneity of B_{1r}.[3.16] It was clear that the UF re-entrant TE_{01U} cavity with the sample centered in the region-of-interest (Fig. 3.9C) has the sharpest feature. The intensity at 0 MHz shown prominently in Fig. 3.9A and reduced in Fig. 3.9B is directly caused by the inhomogeneity of the magnetic field. The majority of this component was removed in Fig. 3.9C.

3.4. Discussion

Dielectric loading variations due to different samples change the cut-off frequency of the region-of-interest, and thus, the uniformity condition of the resonator. Shown in Fig. 3.10 is the simulated microwave magnetic flux squared (B_{1r}^2) profile of the UF re-entrant cylindrical TE_{01U} cavity for a range of dielectric constants (ϵ_r ranges from 1 to 5 in integer steps, with a loss tangent of 0.005) for a fixed Rexolite end section

geometry. The microwave magnetic field squared was used to highlight the differences and is proportional to the EPR signal. The frequency shifted due to the change in the real part of the dielectric from 1 to 5. The frequencies 34.492, 34.206, 33.910, 33.592, 33.264 GHz, ϵ_r from 1 to 5 respectively, which affects the cut-off and homogeneity of B_{1r}.

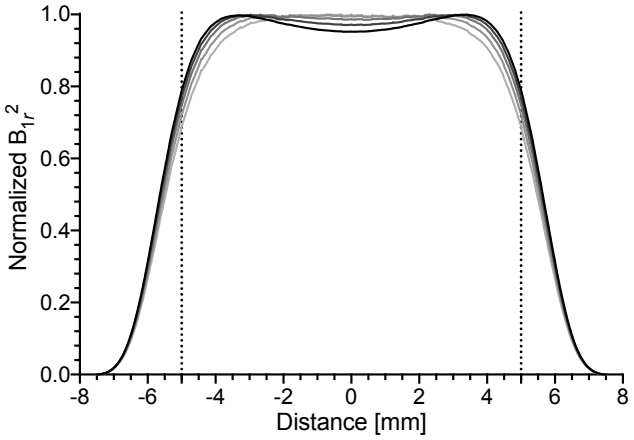

Figure 3.10.: Ansys HFSS simulations of the microwave magnetic field squared (B_{1r}^2) along the axis of the UF re-entrant cylindrical TE_{01U} cavity for a range of dielectrics. The dielectric constant, ϵ, is varied from 1 to 5 (dark to light) with a fixed end section geometry. Dotted lines mark the region-of-interest of the cylindrical re-entrant TE_{01U} cavity. The microwave magnetic field squared is used to highlight the differences and is proportional to the EPR signal.

The Λ_{ave} of the UF re-entrant TE_{01U} resonator was lower than expected from simulations by about 40%. This was mostly due to the Q_0-value being lower than expected. The lowering of the Q_0-value was due to the construction of the prototype resonator out of brass and higher losses in the Rexolite plastic than anticipated. Gold plating the resonator body and experimenting with different plastics would be advantageous.

Higher stored energy density in the coupling and iris region makes the system more frequency-dependent. The increased frequency dependence of the H-type T-junction coupler without inductive perturbations was shown to have a large effect on the coupling efficiency, shown in Fig. 3.8. The frequency dependence is significantly reduced by adding the inductive perturbations. Additionally, by extending the iris over the entire length of the waveguide H-plane, a long-slot iris is created.[3.27] The long-slot iris exhibits lower stored energy density than a resonant iris or inductive hole and minimizes H_1 field perturbations in the region-of-interest. By splitting the long-slot iris to a dual-slot iris, the stored energy density and frequency dependence was further reduced. In general, the reduction of stored energy density outside of the resonator reduces the frequency dependence when tuning, matching, or changing samples. These design criteria are critical for UF resonators.

Shown in Fig. 3.11 are vector network analyzer measurements of the coupling coefficient β_c for the re-entrant TE_{01U} cavity with H-type T-junction coupler and long slot iris (solid) compared to the cylindrical TE_{011} cavity with slot iris from Ref. [3. 22]. The measurments indicated better over-coupling performance for the re-entrant TE_{01U} cavity

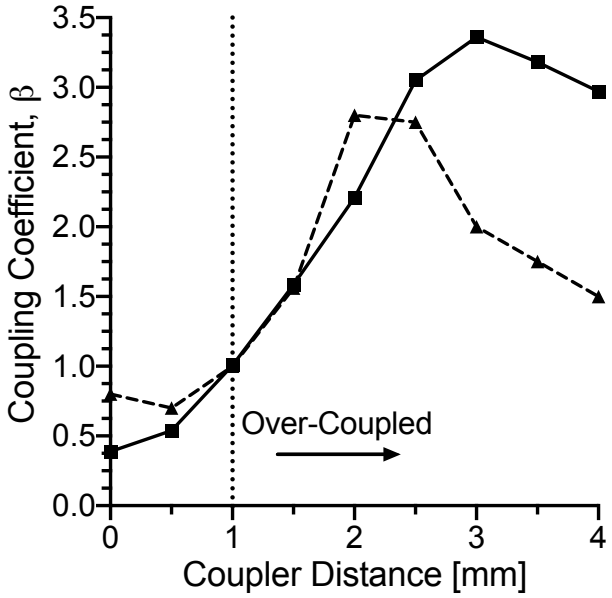

Figure 3.11.: Bench measurements on the vector network analyzer of the coupling coefficient β for the re-entrant TE_{01U} cavity with H-type T-junction coupler and long slot iris (solid) compared to the cylindrical TE_{011} cavity with slot iris from Ref. [3.22] (dashed).

which corresponds to a larger bandwidth by the equation

$$Q_L = \frac{Q_0}{\beta_c + 1}, \tag{3.9}$$

where the loaded Q-value, Q_L, is proportional to bandwidth by $1/\Delta f$.[3.12] With a lower initial Q_0 value, the re-entrant TE_{01U} cavity has a significant increase in bandwidth for comparable EPR signal. The re-entrant TE_{01U} cavity has a calculated bandwidth of approximately 110 MHz, while the cylindrical TE_{011} cavity of Ref. [3.22 has a calculated bandwidth of 46 MHz (Q_0 of 2400).

Finally, in the x- and y-direction the H_1 field exhibits some variation. A smaller inner diameter capillary (with the same outer diameter) could be used to improve this variation but will sacrifice EPR signal intensity. However, the x- and y-direction variation was already 15% better in a re-entrant geometry compared to the cylindrical TE_{011} cavity from both a "sucking-in" effect of the quartz capillary and more confined electric field profile, as shown in Fig. 3.5. The capillary geometry of 2.8 mm OD and 1.8 mm ID was chosen to be compatible with standard Q-band capillary tubes.

3.5. Conclusions

A uniform field re-entrant cylindrical TE_{01U} cavity was designed, fabricated, and tested to improve pulse EPR experiments. The microwave magnetic field was calculated and confirmed by measurements to be 88.3% uniform over the entire cavity and 98% uniform over the region-of-interest. By introducing re-entrant fins to a UF cylindrical TE_{01U} cavity, the Q-value of the re-entrant TE_{01U} cavity was lowered, but the resonator efficiency and the stored energy density was increased. This new geometry yields similar signals

as the standard cylindrical TE_{011} while increasing Λ_{ave} by approximately 60%. The increase of Λ_{ave} affects pulse EPR experiments in two ways: (i) less microwave power is needed for the same tip angle; and (ii) the majority of the sample is excited at the same tip angle.

Initial results using a brass prototype resonator have shown significantly improved data quantified by the nutation experiments. This work showed that a UF re-entrant geometry can provide an enhanced efficiency, increase EPR signal, larger bandwidth and a uniform B_{1r} along the sample volume to improve pulse EPR experiments. Future work includes a gold-plated second-generation resonator, ESEEM, HYSCORE and ELDOR-detected NMR experiments (EDNMR), and extending the UF re-entrant TE_{01U} cavity to W-band frequencies.

Uniform field resonators have several advantages for both continuous-wave and pulse EPR experiments. In continuous-wave EPR at low power, a uniform field resonator with the same active sample volume as a traditional cavity will increase the EPR signal by the ratio of the square of the B_{1r} between the cavities. However, in a traditional cavity at an incident power high enough to cause saturation, a distribution of B_{1r} exists incident on the sample. By increasing the uniformity of B_{1r} all spins along the sample length are saturated at the same value. This has direct implications for the quality of data obtained from a sample under saturation conditions. For example, saturation transfer experiments where the out-of-phase component of the phase-sensitive detector is used as an indicator of molecular motion as the sample is driven under saturation conditions.[3.28]

Uniform field resonators used in pulse experiments will not only increase the EPR signal, but time-dependent effects that may lead to complex backgrounds can be reduced. The effects of non-uniform magnetic flux density excitation are relatively unknown as the number of pulses increase in more sophisticated sequences. In general, uniform field resonators increase the quality of pulse data and reduce artifacts.

CHAPTER 3. REFERENCES

[3.1] R. R. Mett, W. Froncisz, J. S. Hyde, Axially uniform resonant cavity modes for potential use in electron paramagnetic resonance spectroscopy, Rev. Sci. Instrum. 72 (11) (2001) 4188–4200.

[3.2] J. R. Anderson, R. R. Mett, J. S. Hyde, Cavities with axially uniform fields for use in electron paramagnetic resonance. II. Free space generalization, Rev. Sci. Instrum. 73 (8) (2002) 3027–3037.

[3.3] J. S. Hyde, R. R. Mett, J. R. Anderson, Cavities with axially uniform fields for use in electron paramagnetic resonance. III. Re-entrant geometries, Rev. Sci. Instrum. 73 (11) (2002) 4003–4009.

[3.4] J. S. Hyde, R. R. Mett, W. Froncisz, J. R. Anderson, Cavity resonator for electron paramagnetic resonance spectroscopy having axially uniform field, US Patent 6,828,789 (2004).

[3.5] R. R. Mett, J. W. Sidabras, J. S. Hyde, Uniform radio fields in loop-gap resonators for EPR spectroscopy, Appl. Magn. Reson. 31 (2007) 573–589.

[3.6] J. W. Sidabras, T. Sarna, R. R. Mett, J. S. Hyde, Uniform field loop-gap resonator and rectangular $TE_t extU02$ for aqueous sample EPR at 94 GHz, J. Magn. Reson. 282 (2017) 129–135.

[3.7] J. W. Sidabras, R. R. Mett, W. Froncisz, T. G. Camenisch, J. R. Anderson, J. S. Hyde, Multipurpose EPR loop-gap resonator and cylindrical TE_{011} cavity for aqueous samples at 94 GHz, Rev. Sci. Instrum. 78 (3) (2007) 034701.

[3.8] L. Mainali, J. W. Sidabras, T. G. Camenisch, J. J. Ratke, M. Raguz, J. S. Hyde, W. K. Subczynski, Spin-label W-band EPR with seven-loop–six-gap resonator: Application to lens membranes derived from eyes of a single donor, Appl. Magn. Reson. 45 (12) (2014) 1343–1358.

[3.9] Y. E. Nesmelov, A. Gopinath, D. D. Thomas, Aqueous sample in an EPR cavity: Sensitivity considerations, J. Magn. Reson. 167 (1) (2004) 138–146.

[3.10] J. S. Hyde, R. R. Mett, EPR uniform field signal enhancement by dielectric tubes in cavities, Appl. Magn. Reson. 48 (11) (2017) 1185–1204.

[3.11] J. G. Hartnett, M. E. Tobar, J. Krupka, The dependence of the permittivity of sapphire on thermal deformation at cryogenic temperatures, Meas. Sci. Tech. 15 (1) (2003) 203–210.

[3.12] S. Ramo, J. Whinnery, T. Van Duzer, Fields and Waves in Communication Electronics, Wiley, 1984.

[3.13] N. Marcuvitz, Waveguide Handbook, Volume 10 of MIT Radiation Laboratory Series, McGraw-Hill, 1951.

[3.14] G. Eaton, S. Eaton, D. Barr, R. Weber, Quantitative EPR, Springer Vienna, 2010.

[3.15] Methods, A. of Site-directed Spin Labeling EPR Spectroscopy, Methods Cell Biol. 84 (2008) 617–658.

[3.16] A. Schweiger, G. Jeschke, Principles of Pulse Electron Paramagnetic Resonance, Oxford University Press, 2001.

[3.17] N. Cox, A. Nalepa, W. Lubitz, A. Savitsky, Eldor-detected NMR: A general and robust method for electron-nuclear hyperfine spectroscopy?, J. Magn. Reson. 280 (2017) 63 – 78.

[3.18] C. E. Tait, S. Stoll, ENDOR with band-selective shaped inversion pulses, J. Magn. Res. 277 (2017) 36–44.

[3.19] T. Bahrenberg, Y. Rosenski, R. Carmieli, K. Zibzener, M. Qi, V. Frydman, A. Godt, D. Goldfarb, A. Feintuch, Improved sensitivity for W-band Gd(III)-Gd(III) and nitroxide-nitroxide DEER measurements with shaped pulses, J. Magn. Reson. 283 (2017) 1 – 13.

[3.20] A. Doll, G. Jeschke, Wideband frequency-swept excitation in pulsed EPR spectroscopy, J. Magn. Reson. 280 (2017) 46 – 62.

[3.21] J. S. Hyde, J. W. Sidabras, R. R. Mett, Resonators for multifrequency EPR of spin labels, in: S. K. Misra (Ed.), Multifrequency Electron Paramagnetic Resonance: Theory and Applications, Wiley-VCH Verlag GmbH & Co. KGaA, 2011, Ch. 5.2, pp. 244–269.

[3.22] E. Reijerse, F. Lendzian, R. Isaacson, W. Lubitz, A tunable general purpose Q-band resonator for CW and pulse EPR/ENDOR experiments with large sample access and optical excitation, J. Magn. Reson. 214 (2012) 237–243.

[3.23] J. H. Jiang, D. L. Wu, Ice and water permittivities for millimeter and sub-millimeter remote sensing applications, Atmos. Sci. Lett. 5 (2004) 146–151.

[3.24] J. S. Hyde, J. W. Sidabras, R. R. Mett, Uniform field resonators for EPR spectroscopy: A review, Cell Biochemistry and Biophysics 77 (1) (2019) 3–14.

[3.25] R. Harrington, Time-harmonic Electromagnetic Fields, McGraw-Hill, 1961.

[3.26] M. Born, W. Wolf, Principles of Optics: Electromagnetic Theory of Propagation, Interference and Diffraction of Light, 3rd Edition, Pergamon Press, 1965.

[3.27] R. R. Mett, J. W. Sidabras, J. S. Hyde, Coupling of waveguide and resonator by inductive and capacitive irises for EPR spectroscopy, Appl. Magn. Reson. 35 (2) (2009) 285–318.

[3.28] A. H. Beth, E. J. Hustedt, Saturation transfer EPR, in: S. R. Eaton, G. R. Eaton, L. J. Berliner (Eds.), Biomedical EPR, Part B: Methodology, Instrumentation, and Dynamics, Springer US, 2005, pp. 369–407.

4. Weak Coupling of Meta-Materials with Ensemble of Electron Spins: Surface EPR Signal Enhancement in the THz Bandgap.

As the microwave frequency is increased, single-mode cavity resonators and samples become geometrically small. At even higher frequencies (>263 GHz), the further reduced dimensions prevent the fabrication of conventional resonators due to technical limitations. To increase sensitivity at higher frequencies the use of non-resonant structures, such as the so-called "bucket" sample holder, can be employed. In these non-resonant structures, the sample volume is increased to fill the bucket providing a large filling factor η with a Q_0-value effectively at unity.[4.1] However, the shape of the bucket resonator is adapted to powders or solutions filled in tubes, and is not optimal for studies of thin films or surfaces. The ability to measure thin films is crucial for the study of a variety of interesting samples, such as thin magnetic films, thin-film electronic devices, solar cells or other 2D paramagnetic samples.

The transition from volume samples, such as those in single-mode cavity resonators, to planar samples, requires a concentration of the magnetic component of the time-varying excitation field on a cross-sectional area. For example, the plane-concave Fabry-Pérot resonator, which comprises of a resonant structure with one concave mirror and one flat mirror, forms a standing-wave pattern with a maximum magnetic field on the flat-mirror surface.[4.1] Plane-concave Fabry-Pérot resonators exhibit very high Q-values and, due to the simplified geometry, can be designed to operate at frequencies higher than 200 GHz.[4.2, 4.3] However, the resonator geometry still scales with frequency and, due to standing-waves within the resonator, the filling factor can be quite low for thin films. To maximize the EPR signal intensity for thin-film samples, a resonant geometry where the cross-sectional sample area is not dependent on the operating frequency and the filling factor is maximized is required.

One solution is to create a series of single micro-resonators that can be placed in periodic sequences to form a large two-dimensional array. Despite the periodic microstructure, the incident excitation wave interacts with the surface as a bulk material.[4.4] This bulk material, called a meta-material, can be characterized by the single and periodic geometry, mutual coupling between elements, eigenfrequency, and Q_0-value. Meta-material characteristics can then be used to determine the frequency-dependent properties of the bulk material. The frequency-dependent properties of meta-materials were theoretically proposed in 1968 as materials with bulk properties that mimic frequency-dependent negative electric-permittivity $\epsilon_r(\omega)$ and magnetic permeability $\mu_r(\omega)$.[4.5] The ability to tune these properties allows a negative refraction index to be designed for perfect lensing, i.e. images with better resolution than the diffraction limit.[4.6] Unlike single-mode cavities that require the sample to be placed on an axis of maximum sensitivity, meta-materials can provide a bulk material-like enhancement of a sample at a surface.

Recently, it was found that the split-ring resonator (SRR) geometry at sub-wavelength dimensions can be placed periodically on a surface and behave as a meta-material over a broad frequency range.[4.4, 4.7, 4.8] This first realization was shown for the low GHz range,[4.7] then for around 1 THz,[4.4] and for 100 THz.[4.8] The negative $\mu_r(\omega)$ leads

to a resonance effect in the non-magnetic meta-material. Interestingly, meta-material surfaces operating in the THz region have been employed for ultra-sensitive bio-sensing due to their ability to sense small dielectric changes on a surface.[4.9] For a bio-sensing experiment, THz frequency microwave fields are incident on the meta-material and the resulting transmission is monitored for changes as bio-material passes the resonant geometry.[4.10]

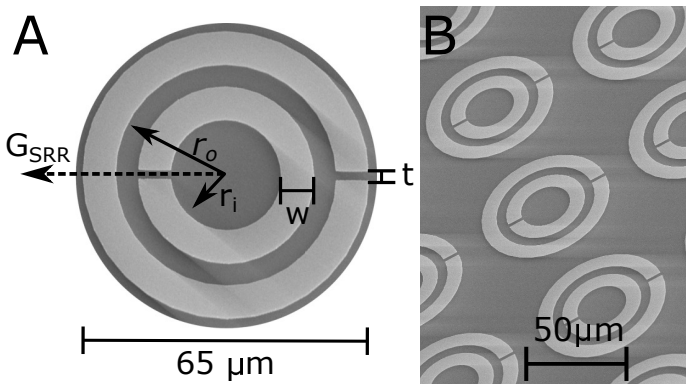

Figure 4.1.: A) Microscope image of the fabricated profile of the dual-ring split-ring resonator (SRR) on quartz glass. In this work dimensions are as follows: r_o is 25 μm, r_i is 12.5 μm, w is 7.5 μm, and t is 2 μm. The vector parallel to the gap is illustrated as G_{SRR}. B) To create a meta-metallic surface each SRR element is spaced 80 μm apart from center-to-center.

Herein, the characterization and experimental realization of a meta-material by a split-ring resonator array (SRRs) for the use of detecting EPR transitions in the 100 GHz to 1 THz frequency range (3.34-33.36 cm^{-1}; THz-bandgap) is presented. The SRRs had an operating frequency of approximately 420 GHz (14 cm^{-1}; free-space wavelength λ of 713.8 μm). A single SRR outer diameter was 65 μm, geometry shown in Fig. 4.1A. Therefore each SRR is less than 1/10th of a wavelength and was spaced 80 μm from the next resonator in a periodic fashion creating the bulk-material. The SRRs, shown in Fig. 4.1B, were placed on a quartz substrate that has an overall diameter of 12 mm providing very large surface area for an operating frequency of 420 GHz.

The results were duplicated with a lumped-circuit transmission-line analytic model. The lumped-circuit transmission-line model, unlike current literature, takes into account both inductive and capacitive coupling. This distinction is important when the interaction of magnetic resonance coincides with the resonant frequency of the SRRs.

The validity of the analytical model was established and used to further understand the interactions that arise between the meta-material and the electron-spins ensemble. Furthermore, the analytical model was used to define the system in terms of weak- and strong-coupling. Through this new understanding, the potential of meta-material arrays for resonant EPR detection at very high frequencies for thin-film samples was illustrated.

4.1. Methods

To characterize the SRRs Frequency-Domain Fourier-Transform THz-EPR (FD-FT THz EPR) experiments were employed. FD-FT EPR is a method to detect magnetic transitions in the THz-bandgap using an interferometer and bolometer detector.[4.11, 4.12] Such methods allow for broad-band detection of EPR in the frequency domain while stepping

the static magnetic field through the EPR resonance condition. Over the last decade, several other EPR instruments were built which operate at microwave frequencies in the THz-bandgap.[4.13–19] The SRRs were characterized and coupled to the electron-spin ensemble of a thin film of the high-spin Fe-ion cluster hemin. The high-spin Fe EPR signal was collected by following the feature located at the effective $g = 6$ position which passes through the frequency of the split-ring resonator as the magnetic field is increased.

Coherent broadband excitation profiles are required for FD-FT EPR experiments. However, at such frequencies, excitation power is limited (milliwatt range) and the frequency range of such sources is limited making frequency domain experiments rather impractical. To overcome these limitations, an alternative excitation and detection scheme has been developed for FD-FT EPR to be performed using a high-power broadband source, such as a coherent beam-line from the BESSY II synchrotron (Helmholtz-Zentrum Berlin; Berlin, DE). From this setup, the EPR spectrum can be ascertained with good signal-to-noise ratio making FD-FT EPR a powerful technique to obtain accurate zero-field splitting parameters.[4.12, 4.20, 4.21]

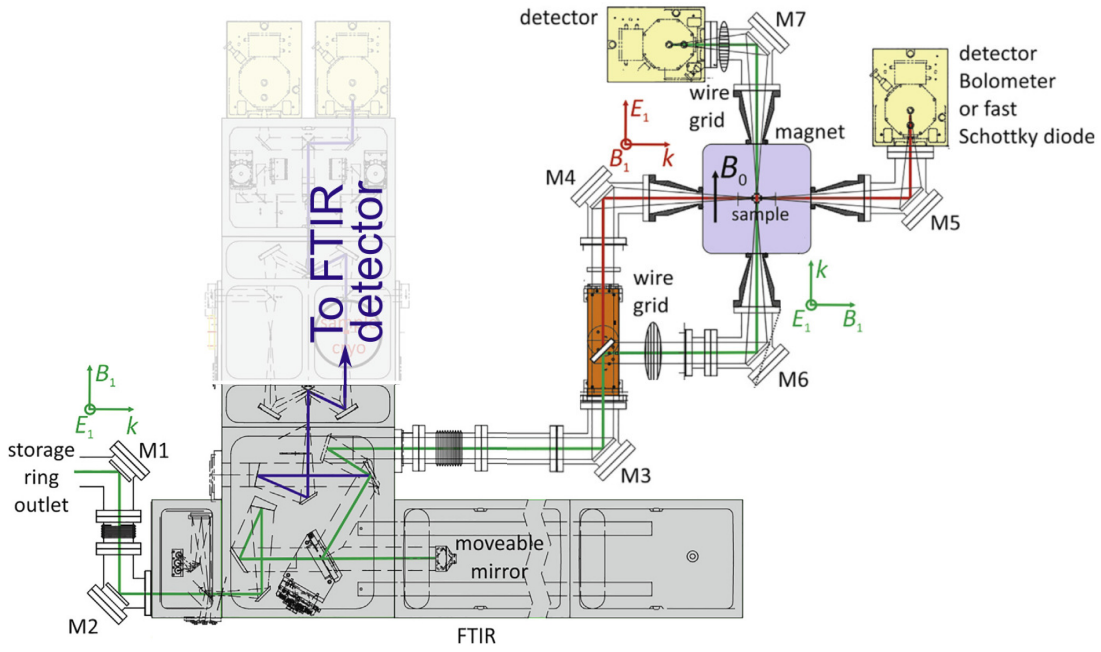

Figure 4.2.: Shown is the schematic overview of the FT-FD THz-EPR setup. The incident wave from the storage ring is sent through a series of mirrors (M1-M3) as it is guided through an FTIR interferometer setup (green line). Here, the polarization of the wave can be rotated (M4) and sent through the static magnetic field ($\mathbf{B}_0$) to M5 and a bolometer detector (red line) or reflected directly (M6) through the static magnetic field ($\mathbf{B}_0$) to M7 and a bolometer detector (green line). The sample is placed in the static magnetic field. An alternative path allows FTIR to be performed (blue line).

Frequency-Domain Fourier-Transform THz-EPR experiments in this work were performed at the synchrotron BESSY II. The experimental setup is shown in Fig. 4.2[4.11, 4.20] In short, intense and coherent broadband linearly-polarized radiation in the THz-gap was provided by the synchrotron BESSY II from the storage ring.[4.22] After passing through the interferometer of an FTIR spectrometer (movable mirror), linearly-polarized THz radiation passes a rooftop mirror which allows rotation of the THz TEM-wave

polarization to any direction perpendicular to the direction of propagation $\boldsymbol{k}$, depicted as the green or red path. Next, the THz radiation was guided through a superconducting magnet (Oxford Spectromag, ±11 T maximal field). The sample was inserted in a variable temperature Dewar (2-300 K) inside the magnet. Finally, the THz radiation was detected with a highly sensitive Si bolometer immersed in a pumped liquid-Helium bath (1.3 K). In this work, the experimental resolution was set to 0.2 cm^{-1} (max resolution: 0.0063 cm^{-1}). For each magnetic field step, a full broadband energy spectrum is collected.

The final set of FD-FT THz EPR spectra were obtained by field division of two subsequent spectra measured at a temperature of 2 K and spaced 0.2 T apart. The field division of spectra was found to produce a more reliable spectrum when comparing features with simulations.[4.11, 4.12, 4.20] The field division process is illustrated in Fig. 4.3. First, a spectrum was measured at B_0 indicated on the y-axis of Fig. 4.3, for example, 5.2 T. The collected spectrum was divided by a spectrum measured at $B_0 - 0.2$ T, for example, 5 T. In this example, the result is shown in red in Fig. 4.3. This is equivalent to a field-stepped modulation and only field-induced changes are visible. A positive deviation indicates that the absorption was stronger at $B_0 - 0.2$ T than at B_0. In the opposite case, the spectra deviate negatively. This effectively results in a "first derivative-like" spectrum.

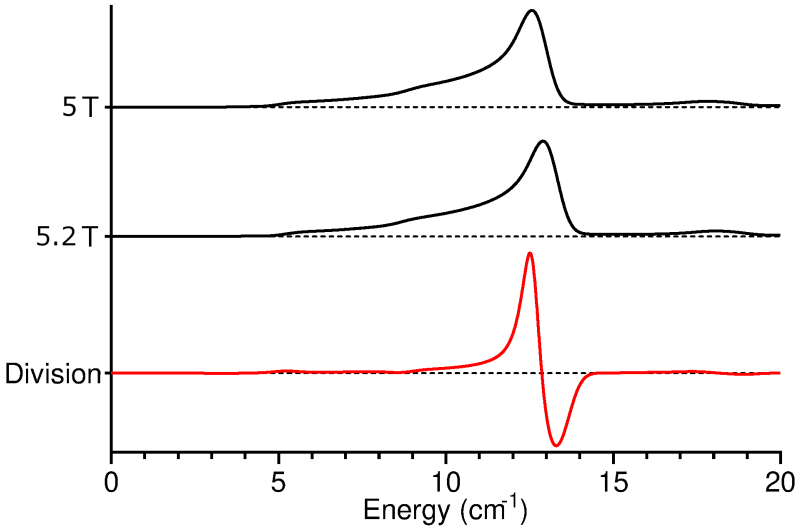

Figure 4.3.: Simulated FD-FT THz EPR spectra are shown at B_0 and $B_0 - 0.2$ T, 5.2 and 5 T. Shown in red is the spectrum after the division process is performed. The large feature around 13 cm^{-1} corresponds to the feature that is measured in this work. EasySpin calculation used $S = 5/2$, g-value of [2.05 1.95], D of 6.93 cm^{-1}, E of 0, line width 0.8 cm^{-1}, and at a temperature of 5 K.

As a test sample, hemin (Sigma-Aldrich) was dissolved in dichloromethane and coated on the SRRs. After evaporation of the solvent, the thickness of the hemin film was determined to be approximately 100 μm. Hemin contains a high-spin Fe^{III} ion ($S = 5/2$), which has a large zero-field splitting.[4.21, 4.23–25] Usually two EPR features are observed, situated at effective g-values around 6 and 2.[4.26] In this study, the EPR signal at the effective g-value of 6 was observed.

The SRRs were produced on a round quartz substrate which can be rotated in the magnet to change the orientation of the SRR relative to the incident electric field of the

THz radiation. The SRR resonator was simulated using Ansys Electromagnetics Suite (Pittsburgh, PA, USA; version 19.1; High Frequency Structure Simulator (HFSS)). Each SRR was individually modeled to obtain the electromagnetic characteristics. Nine SRRs were simulated to establish cross-coupling coefficients using the reciprocity theorem. Due to the SRR mode and geometry, minimal cross-coupling was calculated (less than 5% mutual inductance between elements).

Two experiments were needed to measure the fundamental frequency of the SRR loaded with the sample. The first experiment measures the THz TEM-wave intensity spectrum without the SRR and the second measures the intensity spectrum with the SRR coupled to the THz TEM-wave. The absorbance of the SRRs resonance was then calculated by taking the log of the ratio, such that,

$$A(\omega) = \mathrm{Log}_{10}\frac{\mathrm{I}_{\mathrm{empty}}(\omega)}{\mathrm{I}_{\mathrm{SRRs}}(\omega)}, \tag{4.1}$$

where $\mathrm{I}_{\mathrm{empty}}(\omega)$, and $\mathrm{I}_{\mathrm{SRRs}}(\omega)$, denotes spectra without and with the SRRs, respectively.

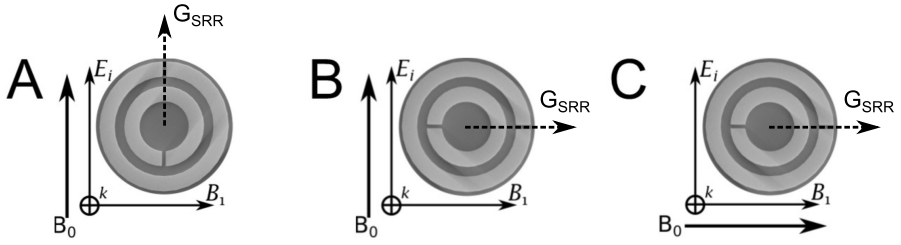

Figure 4.4.: Illustrated is the THz TEM-wave orientation relative to the SRR geometry and $\mathbf{B}_0$. Shown is A) $\mathbf{B}_1 \perp \mathbf{B}_0$ & $\mathbf{E}_i || \mathbf{G}_{SRR}$ B) $\mathbf{B}_1 \perp \mathbf{B}_0$ & $\mathbf{E}_i \perp \mathbf{G}_{SRR}$ and C) $\mathbf{B}_1 || \mathbf{B}_0$ & $\mathbf{E}_i \perp \mathbf{G}_{SRR}$.

The path was chosen such that the static magnetic field $\mathbf{B}_0$ was perpendicular to the direction of the THz wave propagation $\boldsymbol{k}$, illustrated in Fig. 4.4. Hence, the magnetic flux density ($\mathbf{B}_1$) and electric field ($\mathbf{E}_i$) component of the THz radiation can be chosen parallel or perpendicular to the static magnetic field $\mathbf{B}_0$. This allowed three experiments with different THz electric and magnetic TEM-wave orientations relative to the SRR gaps ($\mathbf{G}_{SRR}$) and static magnetic field ($\mathbf{B}_0$) to be performed. These experiments were: When the propagating $\mathbf{B}_1$ was

(A) $\mathbf{B}_1 \perp \mathbf{B}_0$ & $\mathbf{E}_i || \mathbf{G}_{SRR}$: perpendicular to the static magnetic field and the electric field was parallel to the SRR gaps. In this configuration, the SRRs resonance was inactive and only the EPR transition from the incident THz magnetic flux density can be observed. This configuration is named the "No Coupling to SRR with EPR Transition" mode.

(B) $\mathbf{B}_1 \perp \mathbf{B}_0$ & $\mathbf{E}_i \perp \mathbf{G}_{SRR}$: perpendicular to the static magnetic field and the electric field was perpendicular across the SRR gaps. In this configuration, both the incident THz flux density and the coupled flux density from the SRR excite an EPR transition. This configuration was named the "Coupling to SRR with EPR Transition" mode.

(C) $\mathbf{B}_1 || \mathbf{B}_0$ & $\mathbf{E}_i \perp \mathbf{G}_{SRR}$: parallel to the static magnetic field and the electric field was perpendicular across the SRR gaps. In this configuration, no EPR transitions occur from the THz TEM-wave. However, the SRRs resonance was coupled with

the electric field generating a $\mathbf{B}_1$ at the SRR geometry. This configuration was named the "Coupling to SRR without EPR Transition" mode.

4.2. Theory

An analytical model of the experiment was derived to better understand the complex interactions of the EPR signal with the SRR meta-material. Typically, in antenna design only magnetic[4.27] or electric[4.28] excitation would be chosen since magnetic and electric coupling counteract total mutual impedance. Because of this, to our knowledge, the use of both magnetic and electric coupling has not been employed in the literature. For antenna design, only one coupling method is necessary to properly describe the coupling of the SRR.[4.29–32] However, this is not the case when describing the SRRs in a magnetic resonance experiment. When modeling both the frequency dependence of the SRR and the frequency dependence of the magnetic resonance, both magnetic and electric coupling was needed due to non-zero magnetic field interactions (inductive) and electric field across the gap (capacitive) in the neighborhood of resonance. This is described in detail in the Mathematica (Wolfram Research, Champaign, Illinois; v.12.1) code found in Appendix C.

Fundamentally, the FD-FT EPR experiment is the measurement of the change in the magnetic susceptibility of the sample as a function of frequency for a given static magnetic field. Therefore the experiment can be modeled as a continuous-wave experiment by defining the permeability as described in Eqn. 2.33 as a function of the magnetic susceptibility $\chi(\omega)$ of Eqn. 2.34. For simplicity, the Lorentzian line-shape in the neighborhood of resonance of Eqn. 2.34 was used to mimic the feature at the effective g-value of 6. The Lorentzian line-shape reproduced the spectral features well and modeled the true line-shape here does not improve the understanding of the experiment.

Lossless transmission-line model with EPR sample. A free-space lossless transmission-line representation includes a series inductance (L_L) with the value μ_0 as $4\pi \times 10^{-7}$ [H/m] and shunt capacitance (C_L) with the value of ϵ_0 as 8.854×10^{-12} [F/m].[4.33] Therefore, the characteristic impedance of the lossless transmission, defined as

$$Z_0 = \sqrt{\frac{L_L}{C_L}} = \sqrt{\frac{\mu_0}{\epsilon_0}}, \tag{4.2}$$

has a free-space value of 376.7 Ω and assumes infinitely long propagation.

As the THz electromagnetic wave interacts with the sample and the magnetic resonance condition is met, a change in the magnetic susceptibility occurs. Since the transmission-line model incorporates a sample, the free-space μ_0 was replaced with $\mu_r(\omega)$ as defined in Eqs. 2.33 and 2.34. As the static magnetic field is swept, the trans-impedance of the wave is modified and the resulting intensity change is recorded.

Coupled Resonant Circuit with EPR sample. Since little mutual coupling occurs between single SRR geometries, it was sufficient to estimate the inductance of a single SRR and model a simplified transmission-line coupled system. The inductance of the SRR was estimated by the classic equation for the inductance of a loop of wire, such that

$$L_R(\omega) = \mu_r(\omega) a_r \left(\mathrm{Log}\left[\frac{8a_r}{a_w} \right] - 2 \right), \tag{4.3}$$

where a_r is the effective radius of the loop, and a_w is the radius of the wire.[4.33] The capacitance of the SRR (C_R) can be estimated by the resonance equation $\omega_R^2 L_R C_R = 1$,

where ω_R is the resonant frequency of the SRR in radians/s. The resistance is chosen such that the Q_0-value matches the measured SRR Q_0-value. This was calculated by

$$Q_0(\omega) = \frac{\omega_R L_R(\omega)}{R_R}. \tag{4.4}$$

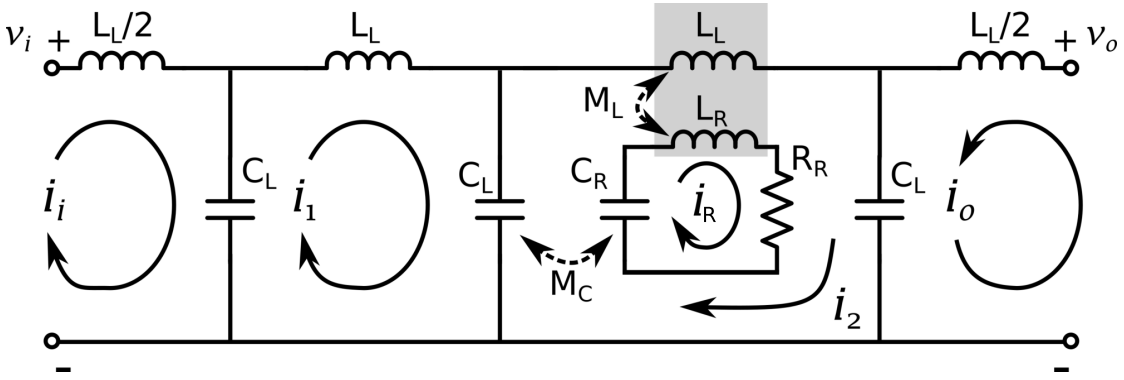

Figure 4.5.: Transmission-line lumped circuit model used to describe the SRR coupling to a plane-wave excitation. Both mutual capacitance (M_c) and mutual inductance (M_L) are used to describe the circuit. Shown in grey is the region of the circuit where magnetic resonance occurs.

Using a circuit model of a transmission line with a coupled resonant circuit, illustrated in Fig. 4.5, the current mesh equations were derived. Such that

$$i(\omega L_L/2 - \frac{1}{\omega C_L})\mathrm{i}_i + i\frac{1}{\omega C_L}\mathrm{i}_1 = v_i \tag{4.5a}$$

$$i\frac{1}{\omega C_L}(\mathrm{i}_i + \mathrm{i}_2) + i(\omega L_L - \frac{2}{\omega C_L})\mathrm{i}_1 + i\omega M_c \mathrm{i}_R = 0 \tag{4.5b}$$

$$i\frac{1}{\omega C_L}(\mathrm{i}_1 - \mathrm{i}_o) + i(\omega L_L - \frac{2}{\omega C_L})\mathrm{i}_2 + i\omega(M_c - M_L)\mathrm{i}_R = 0 \tag{4.5c}$$

$$i\frac{1}{\omega C_L}\mathrm{i}_2 + i(\omega L_L - \frac{2}{\omega C_L})\mathrm{i}_o = v_o \tag{4.5d}$$

$$i\omega(M_c)\mathrm{i}_1 + i\omega(M_L - M_c)\mathrm{i}_2 + (R_R + i\omega L_R - i\frac{1}{\omega C_R})\mathrm{i}_R = 0 \tag{4.5e}$$

where v_i and v_o is the input and output voltage and i_i and i_o is the input and output mesh currents, respectively, of the transmission-line model, while C_R is the capacitance, L_R is the inductance, and R_R is the resistance of the SRR. The mesh currents i_1 and i_2 are indicated in Fig. 4.5 within the transmission line and i_R is the mesh current within the SRR. The mutual inductance (M_L) and mutual capacitance (M_c) are defined by the coupling coefficients,

$$M_c = k_c\sqrt{C_R C_L} \quad \text{and} \tag{4.6a}$$

$$M_L = k_L\sqrt{L_R L_L}. \tag{4.6b}$$

The set of linear equations of Eqn. 4.5 were solved for the currents using Wolfram Mathematica.[1] The relationship of the currents to the voltage is used to find the open-circuit forward trans-impedance, where

$$Z_{21}(\omega) = \left.\frac{v_o}{\mathrm{i}_i}\right|_{\mathrm{i}_o=0} = \left. i\frac{(\omega L_L/2 - \frac{1}{\omega C_L})\mathrm{i}_o - \frac{1}{\omega C_L}\mathrm{i}_2}{\mathrm{i}_i}\right|_{\mathrm{i}_o=0}. \tag{4.7}$$

To mimic the FD-FT THz EPR experiment, the open-circuit forward trans-impedance $Z_{21}(\omega)$ is evaluated at two EPR resonance frequencies ω_0 from Eqn. 2.33 that are 5 GHz apart to produce two spectra for frequency division. These two frequencies in the transmission-line model represent the EPR resonance shift that occurs at two static magnetic fields as performed in the FD-FT EPR experiment. The "resonance shift" is a parameter that was varied step-wise from 1.0-2.0 to shift the spectrum between the energy range of 11-18 cm^{-1}. The transmission-line model division spectrum was calculated by,

$$S(\omega) = \frac{\left.Z_{21}(\omega)\right|_{\omega_0=\omega_a}}{\left.Z_{21}(\omega)\right|_{\omega_0=\omega_b}} - 1 \tag{4.8}$$

where $S(\omega)$ is the EPR signal and ω_a and ω_b are two EPR resonance frequencies representing the resonance shift due to a change in B_0. The pair of frequencies ω_a and ω_b are stepped across the energy range using a "resonance shift" parameter to mimic the change in the static magnetic field. In the experiment and this model, it is important to note that the SRR resonance energy (frequency) does not change when a static magnetic field is applied. Only the EPR transitions change the system as the magnetic susceptibility $\chi(\omega)$ is stepped through resonance.

Strong- and Weak-Coupling Regimes When two resonant modes interact, the resulting frequency response greatly depends on the coupling of the two systems. Specifically, the Q_0-value of the SRR and the amplitude of the magnetic susceptibility $\chi(\omega)$. Two regimes exist: weak-coupling and strong-coupling.

The weak-coupling regime is characterized as only a perturbation as the EPR resonance passes through the SRR resonance when the static magnetic field is stepped. Weak-coupling interactions result in small shifts of the SRR frequency and Q_0-value. A typical EPR experiment is performed if the change in these SRR parameters are measured. The measured shift in SRR frequency and Q_0-value would correspond to dispersion and absorption signals, respectively.[4.34, 4.35] Weak-coupling regime is desired for EPR experiments using meta-material surfaces.

However, as the concentration of the sample increases (increasing the magnetic susceptibility $\chi(\omega)$) or the Q_0-value increases, these systems can exhibit mode-splitting and anti-crossing features centered around the frequency of the SRR and the neighborhood of the EPR resonance. This regime, called strong-coupling, is intensified by resonant structures with large filling factors and can be likened to radiation damping.[4.36–38] One consequence of radiation damping is the second-order effect of the sample changing the current distributions of the resonator as it passes through resonance. Some qualitative understanding of a system with strong-coupling in the context of EPR had led to the understanding of this effect employing the two-coupled oscillator problem.[4.39–41] Herein, it is shown that the lumped-circuit transmission-line model approximates this interaction.

[1] It should be noted that L_R, L_L, M_L are all functions of ω from the relationship with Eqn. 2.33. This was removed in the equations for better readability.

4.3. Results and Discussion

The magnitude of the electric and magnetic field profile at the resonance frequency of the SRR (418 GHz) is shown in Figs. 4.6A and 4.6B, respectively. The dotted line represents the cut plane plotted to the right. To better assess the EPR sensitivity of the SRR with a 100 μm sample, the THz magnetic field squared was plotted in Fig. 4.6C along the axis of the SRR. The magnetic field squared is proportional to the EPR signal. In Fig. 4.6, a dash-dot line was plotted at 24 μm where the area between the quartz substrate surface (0 μm) and 24 μm represents 90% of the EPR signal.

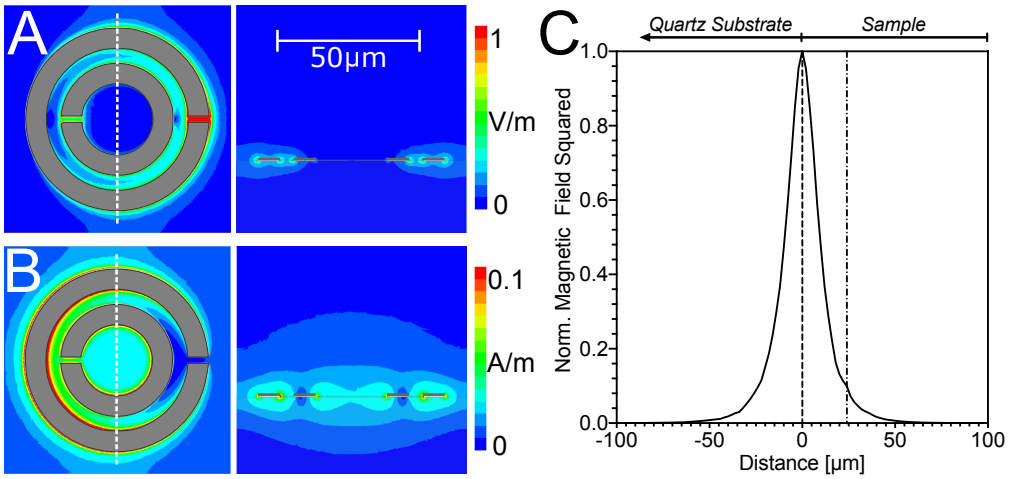

Figure 4.6.: Finite-element modeling solutions plotting the magnitude of the THz A) electric and B) magnetic field profile of the SRR. A cut plane is shown as a dotted line. C) Simulated THz magnetic field profile squared (proportional to EPR signal) on the axis of the SRR. The plot starts from -100 μm into the quartz substrate and through the SRR until the depth of the sample at 100 μm. The dash-dot line shows that 90% of the EPR signal originates from a depth of 24 μm.

Shown in Fig. 4.7 (dashed line) is the result of the measurement at a temperature of 2 K and in the absence of a static magnetic field. This absorbance was then normalized to compare to simulations. Simulations are shown in Fig. 4.7 as a solid line. The absorption feature is associated with the lowest-order resonance mode of the SRRs.[4.28] Without the sample, at an energy of 14.47 cm^{-1}, a pronounced absorbance with the full width at half maximum (FWHM) of 1.45 cm^{-1} was observed. After the thin film of hemin was placed on top of the SRRs, a shift of the absorbance to lower energy of 13.97 cm^{-1}, accompanied by a slight narrowing of the FWHM to 0.87 cm^{-1}. The absorptive feature could be identified in the intensity spectrum (not shown). Using the FWHM, Q_0-values of 10 and 17 were measured for both the SRR without sample and the SRR with the hemin sample, respectively. Simulations show the SRRs resonance at 13.76 cm^{-1} for SRRs with a sample. The frequency deviation of the simulation from the experiment was only 1.5%. The very good agreement was due to the high quality of the manufacturing of the SRRs. The Q_0-value of the simulated SRR was 42. The discrepancy was due to the unknown loss tangent of the hemin sample at THz frequencies.

The EPR transition will only be observed for the magnetic flux density component of the THz radiation $\mathbf{B}_1$ perpendicular to the static magnetic field $\mathbf{B}_0$ ($\mathbf{B}_1 \perp \mathbf{B}_0$).[4.42] Additionally, the resonance of the SRRs only couple to the THz radiation if the electric

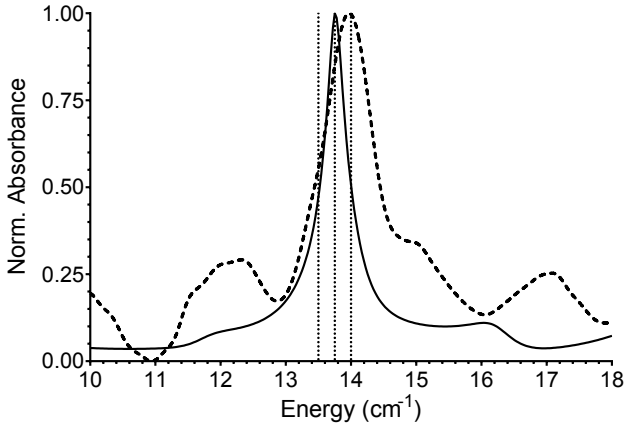

Figure 4.7.: Resonance condition of the SRR meta-material with 100 μm sample calculated using HFSS (solid) and measured (dashed) shown by plotting the normalized absorbance.

field is parallel to the gap of the rings of the SRRs ($\mathbf{E}_i \perp \mathbf{G}_{SRR}$).[4.28] The results of a series of FD-FT EPR experiments can be found in Fig. 4.8A-C and each measurement is described below. The spectra of Fig. 4.8A-C are on the same scale (indicated as Scale A).

No Coupling to SRR with EPR Transition. In this configuration the feature at the effective g-value of 6 of high-spin Fe was observed with almost unchanged intensity over the measured field and frequency range, shown in Fig. 4.8A. This data confirms the SRRs resonance was inactive since only the EPR transition was observed.

Coupling to SSR with EPR Transition. Measured data, shown in Fig. 4.8B, exhibited an increase in the EPR signal of hemin in the frequency range where the EPR line and the SRRs resonance overlap. Over this region, a complex interaction occurs where real and imaginary parts of the magnetic susceptibility $\chi(\omega)$ mix with the frequency-dependent effective $\mu(\omega)$ and $\epsilon(\omega)$ of the SRR.

Coupling to SSR without EPR Transition. In this experiment, $\mathbf{B}_1$ is parallel to $\mathbf{B}_0$ and, as such, EPR transitions should not be observed. However, in the region where the EPR line overlaps with the resonance of the SRRs a feature was observed, data are shown in Fig. 4.8C. This can be rationalized by a magnetic flux density component $\mathbf{B}_1 \perp \mathbf{B}_0$ that arises from the SRR geometry since $\mathbf{E}_i$ is perpendicular to the SRR gaps ($\mathbf{G}_{SRR}$). This configuration demonstrates the use of SRRs in resonance with THz radiation for resonant EPR detection at a single frequency.

Transmission-line model: Results. Parameters to duplicate the FD-FT THz EPR experiments using the lumped-circuit transmission-line model of Fig. 4.5 are shown in Table 4.1. The inductance $L_r(\omega)$, capacitance C_r, and resistance R_r needed to describe the SRR were found by calculating the inductance of a small loop (diameter 20 nm) and setting the capacitance to resonant at 13.9 cm^{-1}. The resistance chosen gives a Q_0-value of 10. The phenomenologically chosen EPR characteristics T_1, T_2, and γ give a Lorentzian line of suitable width to approximate the experimentally observed feature at the effective g-value of 6 as measured in Fig. 4.8A.

The integral of the magnetic susceptibility $\chi(\omega)$ of Eqn. 2.34 was normalized and the parameters g_f and g_r were used for scaling. The parameters encompass the filling factor η and number of spins for free-space and resonant signals, g_f and g_r, respectively. From

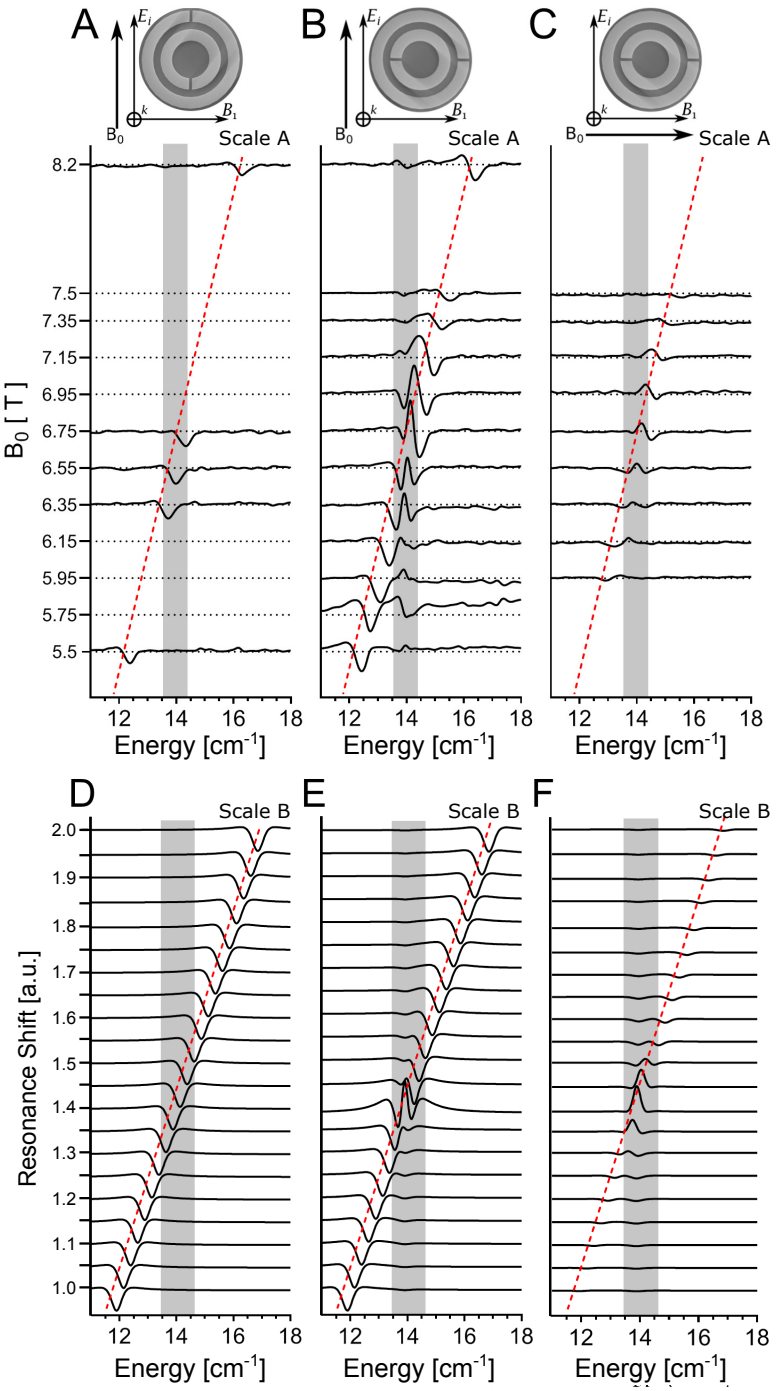

Figure 4.8.: Measured data and lumped-circuit model EPR signal interacting with the SRRs. The red dotted line indicates the calculated transition energy. The grey shaded area indicates the bandwidth of the SRRs with the sample. The SRRs are depicted by a single SRR. The direction of the static magnetic field $\mathbf{B}_0$ is shown compared to the THz radiation traveling wave normal to the SRRs, i.e the $\boldsymbol{k}$ vector goes into the paper, with $\mathbf{E}_i$ and $\mathbf{B}_1$ components indicated. The measurements in the three configurations are: A) No Coupling to SRR with EPR Transition, B) Coupling to SRR with EPR Transition, and C) Coupling to SRR without EPR Transition. The series is repeated using the lumped-circuit model in D-F.

Table 4.1.: Parameters used for the lumped-circuit model characterization.

Param.	Values
L_r	29.76×10^{-15} H
C_r	4.89×10^{-12} F
R_r	0.008 Ω
T_1	4×10^{-9} s
T_2	0.1×10^{-9} s
γ	0.28 MHz/mT

the right-hand side of Eqn. 2.33, the substitution

$$\eta\chi(\omega) = \begin{cases} g_f\hat{\chi}(\omega), & \text{for free-space } L_L(\omega) \\ g_r\hat{\chi}(\omega), & \text{for resonator } L_R(\omega) \end{cases} \tag{4.9}$$

where $\hat{\chi}(\omega)$ is the normalized magnetic susceptibility. Therefore, adjusting g_f and g_r affects the EPR signal intensity by scaling $\mu_r(\omega)$ in $L_L(\omega)$ and $L_r(\omega)$, respectively, in the lumped-circuit transmission-line model. The parameters g_f and g_r can be visualized in the illustration of Fig. 4.9. The parameter g_f represents the whole sample that was excited by the THz plane-wave traveling through the sample, illustrated as the blue hatch in Fig. 4.9A. The parameter g_r represents only the sample that was excited by the SRRs, illustrated as the blue hatch in Fig. 4.9B. When both the EPR transitions and SRR were coupled ($\mathbf{B}_1 \perp \mathbf{B}_0$ and $\mathbf{E}_i \perp \mathbf{G}_{SRR}$) the linear combination of Figs. 4.9A and 4.9B is excited. The spectra of Figs. 4.8D-F use the same g_f and g_r parameters and, therefore, are on the same scale (indicated as Scale B). The parameters used to characterize the coupling and EPR signal for the lumped-circuit model are found in Table 4.2.

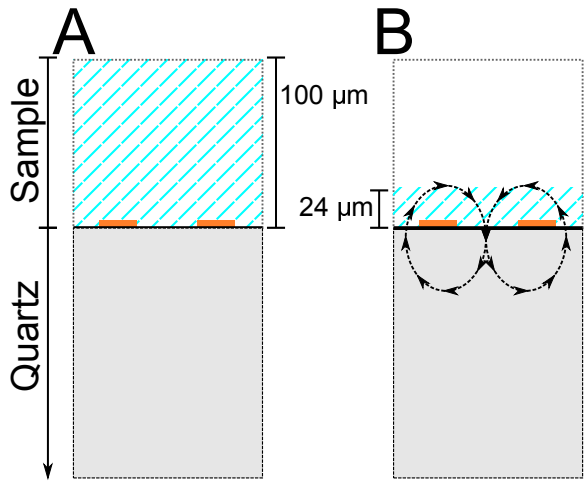

Figure 4.9.: An illustration showing the effective volume for A) the experiment without SRRs coupling and B) the experiment with only SRRs coupling. Here the hatched blue area is the volume of spins and the grey area is the quartz substrate. The THz magnetic field vectors (dashed arrows) are illustrated for the SRR geometry (orange).

In the calculation, coupling was adjusted using the inductive k_L and capacitive k_c coupling constants and fit to the data of Fig. 4.8B. It is noted that the coupling constants are not unique. Nevertheless, one interesting outcome of this model is the ratio of the

amplitude parameters g_f and g_r. A factor of 4.7 is realized for the apparent intensity of the EPR spins in the 24 μm region. This result is consistent with the THz magnetic field squared profile of Fig. 4.6C showing a factor of 4.2 for the sample to active-region ratio compared to Fig. 4.6B. This is reproduced in Figs. 4.6D and 4.6F.

Table 4.2.: Parameters used for the EPR characterization using the lumped-circuit model. The following configurations of A) $\mathbf{B}_1 \perp \mathbf{B}_0$ & $\mathbf{E}_i || \mathbf{G}_{SRR}$, B) $\mathbf{B}_1 \perp \mathbf{B}_0$ & $\mathbf{E}_i \perp \mathbf{G}_{SRR}$, and C) $\mathbf{B}_1 || \mathbf{B}_0$ & $\mathbf{E}_i \perp \mathbf{G}_{SRR}$ are shown.

A.

	Values
g_f	10×10^{-6}
g_r	47×10^{-6}
k_c	0
k_L	0.065

B.

	Values
g_f	10×10^{-6}
g_r	47×10^{-6}
k_c	0.255
k_L	0.065

C.

	Values
g_f	0
g_r	47×10^{-6}
k_c	0.255
k_L	0.065

Using the transmission-line model, the "EPR Transition without SRR Coupling" mode was realized by setting the coupling constant k_c to zero, illustrated in Fig. 4.8D and with parameters reproduced in Table 4.2A. The magnetic coupling constant k_L is not set to zero because there are some vector components of the THz magnetic field that generates a small current on the SRR as shown by the simulations of the surface currents in Fig. 4.10. The scattering magnetic field from the surface currents generated by magnetic coupling does not perturb the EPR transitions from the THz TEM-wave. The transmission-line model results of the "EPR Transition without SRR Coupling" mode are shown in Fig. 4.8D.

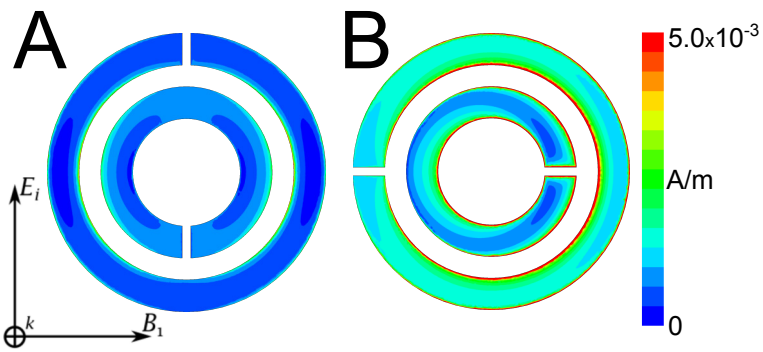

Figure 4.10.: Simulation of the surface currents for SRR coupling. The plane wave used to excite both profiles is shown on the left. A) When the SRR is not coupled to the THz TEM-wave ($\mathbf{E}_i || \mathbf{G}_{SRR}$) there exist surface currents from inductive coupling, k_L. B) When the SRR is coupled to the THz TEM-wave ($\mathbf{E}_i \perp \mathbf{G}_{SRR}$) surface currents are generated primarily by capacitive coupling k_c, yet inductive coupling k_L still exists.

In the "Coupling to SRR with EPR Transition" mode, the EPR transitions occur (g_f is non-zero) and the SRRs were coupled to the incoming THz TEM-wave. Using the transmission-line model, the response of the coupled resonance shown in Fig. 4.8B was duplicated. Data was plotted in Fig. 4.8E and with parameters reproduced in Table 4.2B. The change in the spectral shape shown in Figs. 4.8B and 4.8E can be interpreted as a phase shift between the EPR transition and the frequency-dependent effective $\mu(\omega)$ and $\epsilon(\omega)$ of the SRR. The phase shift is directly related to the capacitive (electric)

and inductive (magnetic) coupling, k_c and k_L, respectively. The spectral shape cannot be reproduced without the small magnetic coupling k_L. The magnetic coupling was enhanced at resonance and both electric and magnetic coupling was required to fit the model to the experiment.

In the "Coupling to SRR without EPR Transition" mode, the EPR transitions do not occur (g_f is zero), but the SRRs were coupled to the THz TEM-wave. The effect of the coupled resonance was duplicated in the calculated data using the lumped-circuit impedance, shown in Fig. 4.8B and with parameters reproduced in Table 4.2C.

At the SRR resonance, a magnetic resonance feature around 14 cm^{-1} was seen that does not shift with the magnetic field, shown clearly in Fig. 4.8B at a static magnetic field of 8.2 T. This feature was also found in calculated data in Figs. 4.8E and 4.8F. This is an interesting feature that, at the time, was thought to be noise, since any EPR transition should follow the linear step of the magnetic field. However, the enhancement provided by the SRRs increases sensitivity. This enhancement of the "tails" of the EPR line is detectable even at the edge of the neighborhood of resonance. This effect can be enhanced by approaching the strong-coupling domain as demonstrated with the transmission-line model.

Transmission-line model: Weak- and Strong Regime. The transmission-line model indicates that the spin system was in a weak-coupling regime, illustrated in Fig. 4.11. Here the solid line represents the frequency shift using the parameters in Table. 4.2C. A weak-coupling frequency perturbation was apparent at a simulated "resonance shift" of 1.4 (black dotted). The perturbation is compared to a constant SRR frequency of 14 cm^{-1} (approximately 420 GHz), represented as a dashed line. As the concentration increases, the magnetic susceptibility $\chi(\omega)$ increases and a non-linear effect occurs between the EPR transition and the resonant frequency of the SRR. This effect is the strong-coupling regime. This was characterized by two resonances (● and ■) interacting and creating an anti-crossing profile. A third resonance, denoted by the symbol ⬭ occurs as the linear shift crossing displaying the onset of strong-coupling. In Fig. 4.11, g_f was set to zero and g_r was increased 100 fold to create the strong-coupling regime compared to the model used to describe the experiment of Fig. 4.8F and Table 4.2C. In practice, the increased in g_r by 100 fold is equivalent to increasing the sample concentration by 100.

4.4. Conclusions and Outlook

SRRs structures have been simulated and experimentally verified for measuring thin films with very high-frequency (3.34-33.36 cm^{-1}; THz-bandgap) EPR. The very good agreement between finite-element modeling simulations and the fabricated SRRs allowed us to investigate the interaction of the SRRs with the EPR line of a high-spin system. The experiments revealed an increased EPR intensity by a factor of approximately 4 for an effective sample depth of 24 μm when the SRRs are employed as a surface resonator. Results were further confirmed using a lumped-circuit lossless transmission-line model which incorporates both magnetic and electric field coupling. The lumped-circuit model provides a unique way to study the interaction of spin-ensembles with meta-materials as the EPR transitions are swept through resonance. From first-principles, the EPR transitions have been included in lumped-circuit model permeability $\chi(\omega)$ which is then "detected" by the change in the trans-impedance of the coupled system.

Unlike meta-material literature for antennas, both magnetic and electric field coupling

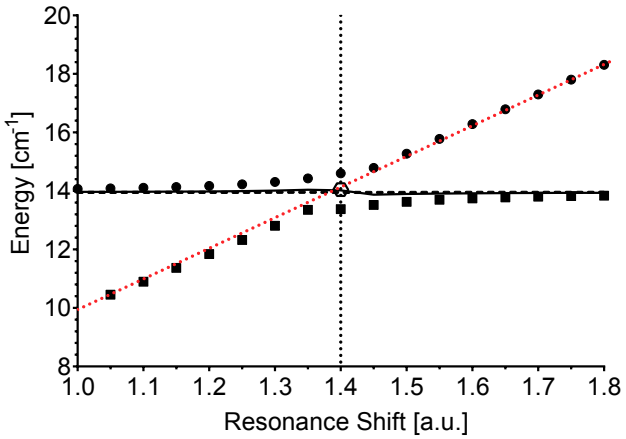

Figure 4.11.: Using the lumped-circuit transmission-line model of Fig. 4.5, a weak- and strong-coupling plot can be obtained. Shown alongside is constant microwave energy (approximately 14 cm^{-1}; dashed). The crossover point is illustrated as a dotted line and represents an SRR resonance at 1.4. The weak-coupling regime is produced by the parameters in Table 4.2C and is plotted as a black solid line. The symbols ○, ●, and ■ represent the frequencies in the strong-coupling regime, while the red dashed line represents the linear shift of the EPR signal as the static magnetic field is shifted.

was required to match the experimental data. When designing a meta-material based antenna, the inductive coupling and capacitive coupling reduce the total coupling over a finite frequency range and provide only a bulk frequency-dependent effective $\mu(\omega)$ and $\epsilon(\omega)$. However, when the SRR was used as a surface resonator for EPR and is covered with a sample, the inductance $\mathrm{L}_L(\omega)$ and mutual inductance $M_L(\omega)$ become a function of the EPR signal. Therefore, inductive coupling was not only a parameter for coupling but was a function of the EPR signal. Conversely, the electric field mutual capacitance M_C does not vary with EPR magnetic resonance. This shift in inductive coupling in the neighborhood of EPR resonance contributes considerably to the shape of the measured signal.

The lumped-circuit transmission-line model gives us a good representation of meta-material enhanced FD-FT THz EPR experiment to optimize the SRR geometry for the study of diluted samples in thin films. For example, by performing multi-frequency high-field EPR experiments.[4.43, 4.44] Such multi-frequency high-field EPR experiments would require several meta-material resonant discs to be fabricated with resonances at multiple frequencies. A series of SRRs could be used to obtain broadband information allowing for the study of dilute protein samples.

The understanding presented here provides a framework to design more complicated meta-material unit structures. By changing the geometry of the unit structure from an SRR, the use of meta-materials can be tuned for further EPR spectroscopy enhancement.[4.45]

CHAPTER 4. REFERENCES

[4.1] O. Grinberg, L. Berliner, Very High Frequency (VHF) ESR/EPR, Biological Magnetic Resonance, Springer US, 2004.

[4.2] R. N. Clarke, C. B. Rosenberg, Fabry–P'erot and open resonators at microwave and millimetre wave frequencies, 2-300 GHz, J. Phys. E Sci. Instrum. 15 (1) (1982) 9–24.

[4.3] R. Braakman, G. A. Blake, Principles and promise of Fabry–P'erot resonators at TeraHertz frequencies, J. Appl. Phys. 109 (6) (2011) 063102.

[4.4] T. J. Yen, W. J. Padilla, N. Fang, D. C. Vier, D. R. Smith, J. B. Pendry, D. N. Basov, X. Zhang, Terahertz magnetic response from artificial materials, Science 303 (5663) (2004) 1494–1496.

[4.5] V. G. Veselago, The electrodynamics of substances with simultaneously negative values of ϵ and μ., Soviet Physics Uspekhi 10 (4) (1968) 509.

[4.6] D. R. Smith, J. B. Pendry, M. C. K. Wiltshire, Metamaterials and negative refractive index, Science 305 (5685) (2004) 788–792.

[4.7] D. R. Smith, W. J. Padilla, D. C. Vier, S. C. Nemat-Nasser, S. Schultz, Composite medium with simultaneously negative permeability and permittivity, Phys. Rev. Lett. 84 (2000) 4184–4187.

[4.8] S. Linden, C. Enkrich, M. Wegener, J. Zhou, T. Koschny, C. M. Soukoulis, Magnetic response of metamaterials at 100 TeraHertz, Science 306 (5700) (2004) 1351–1353.

[4.9] W. Xu, L. Xie, Y. Ying, Mechanisms and applications of TeraHertz metamaterial sensing: A review, Nanoscale 9 (2017) 13864–13878.

[4.10] D.-K. Lee, J.-H. Kang, J. Kwon, J.-S. Lee, S. Lee, D. H. Woo, J. H. Kim, C.-S. Song, Q.-H. Park, M. Seo, Nano metamaterials for ultrasensitive TeraHertz biosensing, Sci. Rep. 7 (1) (2017) 8146.

[4.11] A. Schnegg, J. Behrends, K. Lips, R. Bittl, K. Holldack, Frequency domain Fourier transform THz-EPR on single molecule magnets using coherent synchrotron radiation, Phys. Chem. Chem. Phys. 11 (2009) 6820–6825.

[4.12] J. Nehrkorn, K. Holldack, R. Bittl, A. Schnegg, Recent progress in synchrotron-based frequency-domain fourier-transform THz-EPR, J. Magn. Reson. 280 (2017) 10–19.

[4.13] J. Disselhorst, H. Vandermeer, O. Poluektov, J. Schmidt, A pulsed EPR and ENDOR spectrometer operating at 95 GHz, J. Magn. Reson. Ser. A 115 (2) (1995) 183–188.

[4.14] A. Hassan, L. Pardi, J. Krzystek, A. Sienkiewicz, P. Goy, M. Rohrer, L.-C. Brunel, Ultrawide band multifrequency high-field EMR technique: A methodology for increasing spectroscopic information, J. Magn. Reson. 142 (2) (2000) 300–312.

[4.15] J. van Tol, L.-C. Brunel, R. J. Wylde, A quasioptical transient electron spin resonance spectrometer operating at 120 and 240 GHz, Rev. Sci. Instrum. 76 (7) (2005) 074101.

[4.16] S. A. Zvyagin, M. Ozerov, E. Čižmár, D. Kamenskyi, S. Zherlitsyn, T. Herrmannsdörfer, J. Wosnitza, R. Wünsch, W. Seidel, Terahertz-range free-electron laser electron spin resonance spectroscopy: Techniques and applications in high magnetic fields, Rev. Sci. Instrum. 80 (7) (2009) 073102.

[4.17] S. Takahashi, J. van Tol, C. C. Beedle, D. N. Hendrickson, L.-C. Brunel, M. S. Sherwin, Coherent manipulation and decoherence of S=10 single-molecule magnets, Phys. Rev. Lett. 102 (2009) 087603.

[4.18] P. Neugebauer, D. Bloos, R. Marx, P. Lutz, M. Kern, D. Aguilà, J. Vaverka, O. Laguta, C. Dietrich, R. Clérac, J. van Slageren, Ultra-broadband EPR spectroscopy in field and frequency domains, Phys. Chem. Chem. Phys. 20 (2018) 15528–15534.

[4.19] J. Lu, I. O. Ozel, C. A. Belvin, X. Li, G. Skorupskii, L. Sun, B. K. Ofori-Okai, M. Dincă, N. Gedik, K. A. Nelson, Rapid and precise determination of zero-field splittings by terahertz time-domain electron paramagnetic resonance spectroscopy, Chem. Sci. 8 (11) (2017) 7312–7323.

[4.20] J. Nehrkorn, B. M. Martins, K. Holldack, S. Stoll, H. Dobbek, R. Bittl, A. Schnegg, Zero-field splittings in metHb and metMb with aquo and fluoro ligands: a FD-FT THz-EPR study, Mol. Phys. 111 (18-19) (2013) 2696–2707.

[4.21] J. Nehrkorn, J. Telser, K. Holldack, S. Stoll, A. Schnegg, Simulating frequency-domain electron paramagnetic resonance: Bridging the gap between experiment and magnetic parameters for high-spin transition-metal ion complexes, J. Phys. Chem. B 119 (43) (2015) 13816–13824.

[4.22] M. Abo-Bakr, J. Feikes, K. Holldack, G. Wüstefeld, H.-W. Hübers, Steady-state far-infrared coherent synchrotron radiation detected at BESSY II, Phys. Rev. Lett. 88 (2002) 254801.

[4.23] C. Johnson, Hyperfine field of ^{57}Fe in hemin, Phys. Lett. 21 (5) (1966) 491 – 492.

[4.24] V. Marathe, S. Mitra, Zero-field splitting in hemin, Chem. Phys. Lett. 19 (1) (1973) 140 – 142.

[4.25] G. Lang, W. Marshall, Mössbauer effect in some haemoglobin compounds, J. Mol. Biol. 18 (3) (1966) 385 – 404.

[4.26] J. Pilbrow, Transition Ion Electron Paramagnetic Resonance, Oxford science publications, Clarendon Press, 1990.

[4.27] J. Naqui, L. Su, J. Mata, F. Martín, Recent advances in the modeling of transmission lines loaded with split ring resonators, Int. J. Antennas Propag. 2015 (792750) (2015) 13.

[4.28] N. Katsarakis, T. Koschny, M. Kafesaki, E. N. Economou, C. M. Soukoulis, Electric coupling to the magnetic resonance of split ring resonators, Appl. Phys. Lett. 84 (15) (2004) 2943–2945.

[4.29] J. Baena, J. Bonache, F. Martin, R. Sillero, F. Falcone, T. Lopetegi, M. Laso, J. Garcia-Garcia, I. Gil, M. Portillo, M. Sorolla, Equivalent-circuit models for split-ring resonators and complementary split-ring resonators coupled to planar transmission lines, IEEE Trans. Microw. Theory Tech. 53 (4) (2005) 1451–1461.

[4.30] M. Durán-Sindreu, J. Naqui, F. Paredes, J. Bonache, F. Martín, Electrically small resonators for planar metamaterial, microwave circuit and antenna design: A comparative analysis, Appl. Sci. 2 (2) (2012) 375–395.

[4.31] R. Bojanic, V. Milosevic, B. Jokanovic, F. Medina-Mena, F. Mesa, Enhanced modelling of split-ring resonators couplings in printed circuits, IEEE Trans. Microw. Theory Tech. 62 (8) (2014) 1605–1615.

[4.32] L. Su, J. Naqui, J. Mata-Contreras, P. Velez, F. Martin, Transmission line metamaterials based on pairs of coupled split ring resonators (SRRs) and complementary split ring resonators (CSRR): A comparison to the light of the lumped element equivalent circuits, in: 2015 International Conference on Electromagnetics in Advanced Applications (ICEAA), IEEE, 2015.

[4.33] S. Ramo, J. Whinnery, T. Van Duzer, Fields and Waves in Communication Electronics, Wiley, 1984.

[4.34] A. Abragam, The Principles of Nuclear Magnetism, Clarendon Press, 1961.

[4.35] C. P. Poole, Electron Spin Resonance: A Comprehensive Treatise on Experimental Techniques, Interscience, 1967.

[4.36] N. Bloembergen, R. V. Pound, Radiation damping in magnetic resonance experiments, Phys. Rev. 95 (1954) 8–12.

[4.37] S. Bloom, Effects of radiation damping on spin dynamics, J. Appl. Phys. 28 (7) (1957) 800–805.

[4.38] A. Szöke, S. Meiboom, Radiation damping in nuclear magnetic resonance, Phys. Rev. 113 (1959) 585–586.

[4.39] A. Schneider, A. Shuvaev, S. Engelbrecht, S. O. Demokritov, A. Pimenov, Electrically excited inverse electron spin resonance in a split-ring metamaterial resonator, Phys. Rev. Lett. 103 (2009) 103907.

[4.40] G. Boero, G. Gualco, R. Lisowski, J. Anders, D. Suter, J. Brugger, Room temperature strong coupling between a microwave oscillator and an ensemble of electron spins, J. Magn. Reson. 231 (2013) 133–140.

[4.41] G. Scalari, C. Maissen, D. Turčinková, D. Hagenmüller, S. De Liberato, C. Ciuti, C. Reichl, D. Schuh, W. Wegscheider, M. Beck, J. Faist, Ultrastrong coupling of the cyclotron transition of a 2d electron gas to a thz metamaterial, Science 335 (6074) (2012) 1323–1326.

[4.42] J. Nehrkorn, A. Schnegg, K. Holldack, S. Stoll, General magnetic transition dipole moments for electron paramagnetic resonance, Phys. Rev. Lett. 114 (2015) 010801.

[4.43] J. Krzystek, A. Ozarowski, J. Telser, Multi-frequency, high-field EPR as a powerful tool to accurately determine zero-field splitting in high-spin transition metal coordination complexes, Coord. Chem. Rev. 250 (17-18) (2006) 2308–2324.

[4.44] J. Telser, J. Krzystek, A. Ozarowski, High-frequency and high-field electron paramagnetic resonance (HFEPR): A new spectroscopic tool for bioinorganic chemistry, J. Bio. Inorg. Chem. 19 (3) (2014) 297–318.

[4.45] L. Zhang, S. Mei, K. Huang, C.-W. Qiu, Advances in full control of electromagnetic waves with metasurfaces, Adv. Opt. Mater. 4 (6) (2016) 818–833.

5. Self-Resonant Micro-Helix for nano-Liter Volume Single-Crystals at X-band Frequencies.

For typical EPR experiments on proteins, a frozen solution of 0.1-1 mM concentration is prepared and placed in a microwave cavity. Standard sample volumes at X-band frequencies (nominally 9.5 GHz) are in the 200 μl range. However, frozen solution EPR experiments only allow the determination of the principal values of magnetic interactions at an active site, and thus provide only a limited view of the electronic structure.[5.1, 5.2]

To resolve the full tensor magnetic interaction parameters, such as g-, zero field, hyperfine-, and, for nuclei with $I > 1/2$, quadrupole-tensors, single-crystal EPR experiments must be performed. In combination with X-ray crystallography diffraction, the magnetic-interaction tensors obtained with EPR experiments can be directly related to the protein geometry to help identify and better understand the catalytic mechanism of the enzyme.[5.3, 5.4] Despite its usefulness, single-crystal EPR is rarely applied to protein systems due to challenges in growing crystals of sufficient quality and volume for these experiments. Many protein crystals used in X-ray crystallography diffraction are of dimensions in the 50–300 μm range and, as such, are too small to be studied using commercial EPR instrumentation. Crystallization methods, such as macroseeding,[5.5] have the potential to increase the volume of the crystals, but such techniques are difficult to broadly implement.

Currently, volume-limited crystals can only be studied using high-frequency EPR in a single-mode[5.6], or, for continuous-wave experiments, Fabry-Pérot[5.7] resonators at W-band (94 GHz) or higher. Such high-frequency EPR spectrometers are not widely available and high-frequency conditions are usually unfavorable for advanced pulse experiments such as Electron Spin Echo Envelope Modulation (ESEEM) or Hyperfine Sublevel Correlation (HYSCORE) spectroscopies.[5.8]

Unlike nuclear magnetic resonance (NMR), where all nuclei are excited and contribute to the NMR signal, hyperfine spectroscopy experiments, such as ESEEM, HYSCORE, and electron-nuclear double resonance (ENDOR), probe only the nuclei that are magnetically coupled to the paramagnetic center. Extending these experiments to single crystals not only provides the magnitude of the hyperfine- and quadrupole-tensors of ligand nuclear spins that interact with the paramagnetic centers, but also the associated angles relative to the geometry of the active site of an enzyme. Such interacting nuclei are either naturally abundant, such as ^{1}H and ^{14}N, or the catalytic cofactors must be enriched with nuclei such as ^{2}H, ^{13}C, ^{15}N, and ^{57}Fe, for further analysis of magnetic interaction tensors with respect to the first ligand-sphere. Furthermore, the same interaction tensors can be calculated from the molecular structure using quantum chemical calculations.[5.9] These experimentally determined spectroscopic parameters can, therefore, be used to verify the adequacy of the level of theory which, in turn, gives confidence to the predicted electronic and geometric structure of the involved intermediates and transition states in the whole catalytic cycle. The groundwork for understanding the inner workings of enzymes lies in collecting as much accurate spectroscopic information as possible, including other

A significant portion of this chapter is from J. W. Sidabras, J. Duan, M. Winkler, T. Happe, R. Hussein, A. Zouni, D. Suter, A. Schnegg, W. Lubitz, E. J. Reijerse, Sci. Adv., 10 (5) (2019), eaay1394. and is reproduced under the CC BY-NC license.

spectroscopic and structural methods (for example, optical and vibrational spectroscopy, Mößbauer, X-ray spectroscopy, and diffraction, etc.). Every experiment contributes to the total picture and ultimately leads to a fundamental understanding of the catalytic mechanism of these enzymes.

To improve the sensitivity for studying single crystals using EPR on readily available spectrometers, typically at X-band frequencies, the microwave cavity design must be abandoned and replaced with small-volume resonators based on lumped-circuits in the microwave frequency range. This allows the reduction of the sample volume by one order of magnitude, from 200 μl to 20 μl using a loop-gap resonator.[5.10] Further reductions can be achieved by incorporating materials with a high dielectric constant in a standard resonator to reduce the active volume down to 1 μl.[5.11–13] For protein single-crystals the volume must be reduced even further (less than 0.03 μl), which requires radical new approaches.

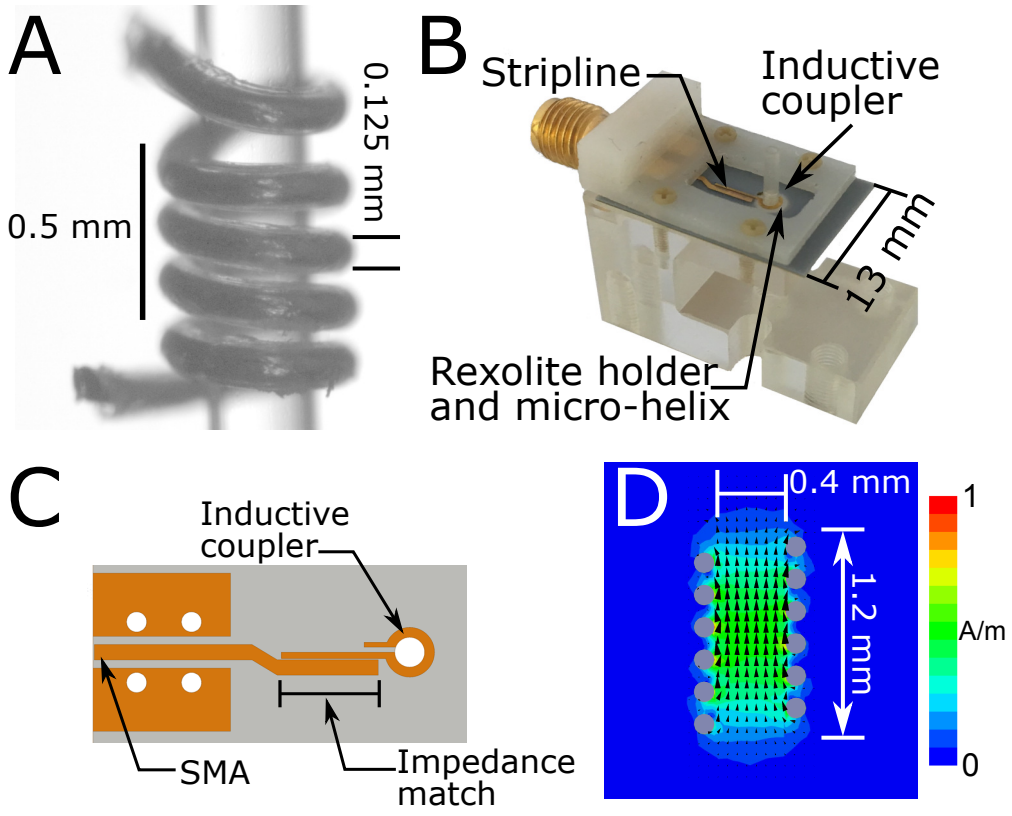

Figure 5.1.: The self-resonant micro-helix. A) A fabricated five-turn micro-helix wrapped around a 0.4 mm outer diameter capillary. The micro-helix is glued into a Rexolite holder and then placed in a B) coupling and support assembly which includes a planar micro-coupler. C) The planar micro-coupler consists of a stripline impedance-match to an inductive coupling loop. D) Finite-element modeling simulations of the microwave magnetic field normalized to Max(H_1).

The focus is on the development of resonant structures to increase EPR absolute spin sensitivity at X-band frequencies without the use of superconducting materials, which require temperatures that are sub-optimal for metallo-enzyme research and exhibit Q-values too large for pulse experiment, or commercial bridge modifications, which require technical expertise not commonly available in EPR laboratories. The concept of a

self-resonant micro-helix, shown in Fig. 5.1A is combined with that of a planar micro-coupler, shown in Figs. 5.1B and 5.1C. The coupling structure on the printed circuit board is a resonant structure that drives the self-resonant micro-helix placed in the center of the coupling loop,[5.14] shown in Fig. 5.1B. The micro-helix geometry offers significant advantages, in that, the microwave field homogeneity is strongly improved along with volume sensitivity for small samples (Fig. 5.1D), the microwave characteristics are optimal for pulse and continuous-wave experiments with need for very little microwave power, and the micro-helix assembly is easily matched and tuned over a variety of samples and temperatures.

In this chapter, the design and implementation of a micro-helix is outlined. Experimental and simulated comparisons of the micro-helix geometry to commercially available and state-of-the-art resonator designs are presented. To further test the micro-helix geometry two experiments were performed on photosystem II tyrosine D radical: an 85 nl frozen solution and $0.3 \times 0.18 \times 0.18$ mm^3 single crystal. These data demonstrate the utility of the micro-helix in studying protein single-crystals at volumes relevant for X-ray crystallography and provide a benchmark for future work.

5.1. Methods

Four resonator geometries were compared in this work. The Bruker Biospin (i) dielectric ER4118X-MD-5W1 (MD5W1; sapphire ϵ_r of 11.5 parallel to C-axis and 9.3 perpendicular to C-axis) resonator and (ii) loop-gap resonator (LGR) ER4118X-MS-3W1 (MS3; split-ring) resonators were used as comparisons to known commercial resonator geometries. The dimensions of the MD5W1 and the MS3 can be found in Figs. 5.2A and 5.2B, respectively. Additionally, two Ω-shaped 0.5 mm ID planar micro-resonators (PMR) were also tested.[5.15–18] The first PMR was printed on (iii) Rogers 6010LM (RO6010LM; Rogers Corp, Chandler, AZ, USA) substrate. The second PMR was printed on a (iv) sapphire substrate. Both PMR geometries have a 0.5 mm hole through the substrate which allows for a capillary sample to be placed in the center of the resonator. The general geometry for the PMR is shown in Fig. 5.2C.

The commercially available resonators, PMR, and micro-helix designs were modeled in Ansys HFSS using driven mode. In driven mode, Ansys HFSS requires a coupling structure and mimics the output of a network analyzer. All designs were matched to 50 Ω with an $S_{11} < -35$ dB. Frequency and Q-values are read directly from a simulated S_{11}-plot and Q_0-values are calculated by Eqn. 3.9.[5.19] EPR signal intensity (unsaturable signal Eqn. 2.29; saturable signal Eqn. 2.28) and resonator efficiency values (mT/W$^{1/2}$; Λ_{ave} Eqn. 2.31) were calculated using Ansys HFSS.[5.20]

The micro-helix was fabricated by hand winding 5 to 8 turns of 0.125 mm diameter silver wire with Polytetrafluoroethylene (PTFE) coating (0.0255 mm thickness, total 0.18 mm diameter; Science Products, GmbH, Hofheim, Germany) around a 0.4 mm drill bit and placed inside a Rexolite cylinder (0.8 mm inner diameter and 1.2 mm outer diameter) with a length of 10 mm. The drill bit was removed as the coil is affixed with super-glue by capillary action, waiting 1 minute, and blowing out the excess. The assembly was left to dry for several days.

The coupling loop was designed in Ansys HFSS and prepared for fabrication with AutoDesk Inventor Professional 2019. The printed circuit board designs were emailed to Streamline Circuit (Santa Clara, CA, USA) engineers and manufactured on a PTFE substrate. The printed circuit board was connected to the bridge by a high-frequency

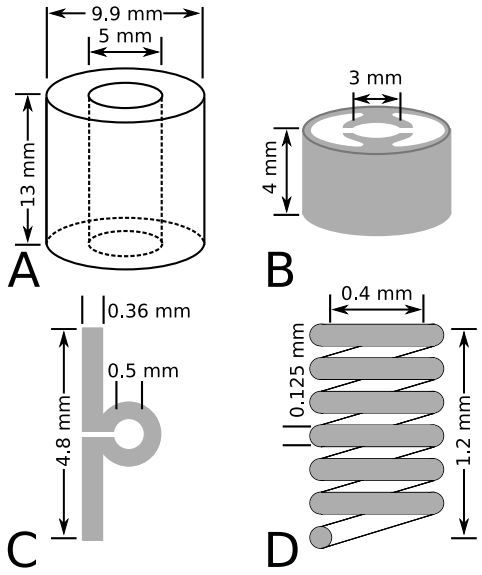

Figure 5.2.: Dimensions and geometry of the four resonators compared in this work. A) Bruker Biospin ER4118X-MD-5W1 (MD5W1) sapphire dielectric resonator, B) Bruker Biospin ER4118X-MS-3W1 (MS3) split-ring resonator, C) Planar Micro Resonator 0.5 mm inner loop diameter, and D) self-resonant micro-helix with a 0.4 mm inner diameter. Grey indicates metallic surfaces.

SMA end launcher (AmphenolRF; 901-10510-1). Impedance matching was achieved by moving the micro-helix relative to the coupling loop until critically coupled on a network analyzer. If required, fine-tune matching was obtained with a slide-screw tuner at the bridge output.

Bench tests of resonator characteristics, such as the frequency measurements, Q_0-value, and sample frequency shifts, were performed on an Agilent 8722ES (now Keysight Technologies; Santa Rosa, CA, USA) vector network analyzer.

A comparison of resonator EPR characteristics was performed on an Elexsys E580 X-band bridge by Bruker Biospin. The signal-to-noise ratio for the measured data was calculated by the ratio of the acquired signal to the standard deviation of the noise voltage, defined by

$$\mathrm{SNR} = \frac{S_{p\text{–}p}}{2\sigma_{noise}} \tag{5.1}$$

where $S_{p\text{–}p}/2$ is the mean value of the peak-to-peak (or peak for absorption spectra) signal, and σ_{noise} is the standard deviation of the noise.[5.21, 5.22] The standard deviation of the noise was calculated using 200 points in an off-resonance region.

The photosystem II complex sample from spinach was prepared by following the BBY method. The BBY particles were placed in a 0.4 mm outer diameter capillary with a 0.3 mm inner diameter.[5.23] The tyrosine D ($Y_D^\bullet$) radical was generated by ambient light at room temperature for a few minutes and then rapidly frozen in liquid nitrogen. The $Y_D^\bullet$ radical is well-suited as a biological test sample since it has been extensively studied and the g- and hyperfine tensors are known.[5.6] Using UV-VIS spectroscopy, the number of chlorophyll molecules in the sample can be determined and, taking into account that there are approximately 250 chlorophyll molecules per photosystem II complex in spinach, the approximate number of core complexes in the active volume were calculated. Each photosystem II complex contains one $Y_D^\bullet$ radical. For the sample prepared in this work,

7.9 μM/ml of chlorophyll molecules were measured, resulting in approximately 1.6×10^{12} $Y_D^\bullet$ radicals in the 85 nl that fill the micro-helix.

Additionally, the photosystem II core complex was extracted and purified from the thermophilic cyanobacterium *Thermosynechococcus elongatus* and crystallized to reach a crystal size of 0.3 × 0.18 × 0.18 mm^3, using the method of Athina Zouni and colleagues.[5.24] The crystals were gradually transferred to a cryogenic protection buffer (100 mM MES, pH 6.5, 5 mM $CaCl_2$, 30% (w/w) glycerol, 16% PEG2000). The photosystem II core complex forms an asymmetric unit during crystallization and has a unit cell space group symmetry $P2_1\,2_1\,2_1$ which copies the asymmetric unit into four sites (PDB ID: 1W5C, Ref. [5.24]) for a total of eight $Y_D^\bullet$ radicals per unit cell. From the geometry, approximately 8.9×10^{12} $Y_D^\bullet$ radicals were calculated in the sample measured herein. The active center and the $Y_D^\bullet$ of a cyanobacterium is equivalent to that of the photosystem II from spinach.

5.2. Results and Discussion

5.2.1. Self-Resonant Micro-Helix Design

Cavity resonators, such as the Bruker Super High-Q, are not sufficiently sensitive for extremely small samples since the very small filling factor (η Eqn. 2.21) is not compensated by the high Q-value (Eqn. 2.19) resulting in a poor EPR signal.[5.25] Therefore, one way to maximize Λ_{ave} of Eqn. 2.31 is to reduce the size of the resonant structure relative to the sample volume, increasing the filling factor. The challenge arises due to potentially increasing the losses in the system, degrading the Q-value, more than the increase in the filling factor. Two common methods to reduce the size of a resonant geometry is to either use dielectric resonators (DR) to reduce the wavelength and, consequently, the size of the resonator or loop-gap resonators (LGR) to reduce the cut-off frequency of a waveguide by introducing protrusions to create regions of inductive loops and capacitive gaps. However, to study sample volumes less than 0.03 μl, further resonator reduction strategies are needed.

Limitations to minimizing LGR geometries stem from an increase in Ohmic losses due to a reduction in the gap spacing to maintain a constant resonant frequency as the sample-loop radius is reduced. In practice, this has put a limit on the Λ_{ave} obtainable to less than 1 mT/W$^{1/2}$ for X-band frequencies. Further EPR signal improvement is possible using dielectric resonators by increasing the dielectric permittivity, and dielectric resonators with permittivity up to 80 have been used for continuous-wave EPR experiments on crystals of porous materials and polymers.[5.11, 5.12] However, such resonators exhibit Q-values over 2500 that make pulse experiments problematic.[5.26]

Several other approaches have been followed to develop application-specific resonators for micro-samples: microstrip resonators (MR)[5.27, 5.28], ultra-miniature micro-resonators (UMR, 2-150 μm)[5.29], surface loop-gap micro-resonators (LGMR, 50-150 μm)[5.30], very high-permittivity dielectric resonators[5.31, 5.32], and planar micro-resonators.[5.15, 5.16, 5.18] All of which significantly reduce the size of the resonator, but have challenges that limit the usefulness for single-crystal experiments. Herein, a new type of resonator is introduced based on a self-resonant micro-helix which is particularly useful for protein single-crystal experiments at X-band and can be used as a drop-in replacement on a standard commercial system. The self-resonant micro-helix geometry, illustrated in Fig. 5.1, solves these challenges by providing good magnetic field homogeneity, a high-efficiency parameter, an optimum Q-value for both pulse and continuous-wave EPR

experiments, straight-forward impedance matching, and ease of sample placement.

Helical resonators were first introduced to EPR in the early-1960s as a method to increase the microwave magnetic field at the sample. Resonant helical geometries were affixed to one end of a shorted waveguide creating a slow-wave structure.[5.33, 5.34] Coupling was achieved by direct connection to a coaxial line with a capacitive matching network or by microwave incident on the helical structure from a waveguide. The sample was placed within the helix and showed a reasonable sensitivity increase and larger microwave magnetic field due to higher filling factors compared to typical cavities.[5.35] Broadband slow-wave helical resonators were employed for multi-frequency experiments, where a non-resonant structure, having a Q-value close to unity, could be matched with a slide-screw tuner over an octave bandwidth.[5.36] However, over time, they were replaced by loop-gap resonators which achieved higher concentration sensitivity for limited samples.[5.37]

Recently, micro-coils have gained popularity in NMR for nano-liter samples[5.38–43] and for microfluidics.[5.44] However, three characteristics differentiate the micro-helix configuration from those described in the EPR[5.33, 5.34, 5.45] and NMR literature[5.46]: (i) the helix is self-resonant, meaning that the self-inductance of n-turns (L_{tot}) and self-capacitance between the loops (C_{tot}) resonate at a frequency determined by $\omega^2 L_{tot} C_{tot} = 1$, where ω is the resonant frequency in radians/s. Since the geometry is self-resonant, no additional capacitors are needed. A self-resonant micro-helix has lower Ohmic loss, which provides a higher Q-value than is typically feasible with micro-coil geometries in NMR, where, with an NMR micro-coil, a typical Q-value is around 30.[5.46] With a self-resonant micro-helix, the volume to surface ratio is maximized and a Q-value of 300 is achievable. (ii) Compared to previous EPR literature, the helix length is much smaller than the wavelength (31.6 mm at 9.5 GHz), which increases the uniformity and the inner diameter is 0.4 mm at X-band frequencies, which increases the resonator efficiency. With this geometry, the micro-helix is not a slow-wave structure but an inductor at self-resonance. The normalized microwave magnetic field profile is shown in Fig. 5.1D. (iii) Finally, the helix is coupled to an inductive coupling loop on a printed-circuit board by mutual inductance, which can be designed to minimize noise and further increase the EPR signal-to-noise ratio.[5.14] Mutual inductance coupling does not require a balun or capacitive matching network, simplifying coupling methods.

5.2.2. Simulated Comparison of a Planar micro-resonator & a self-resonant micro-Helix

HFSS Tutorial

In this section an eigenmode solution was constructed for both the PMR and micro-helix to compare how the signal (Eqns. 2.28 and 2.29) and resonator efficiency Λ_{ave} (Eqn. 2.31) scale with a lossy aqueous sample ($\epsilon_r = 63 - i26.46$ from Ref. [5.47]) and relatively-lossless ice sample ($\epsilon_r = 3.17 - i0.0035$ from Ref. [5.48]). An eigenmode solution was used for simplicity since it requires no matching network.

The Ansys HFSS solutions were created using local variables for performing parametric sweeps.[1] For instance, the sample radius on both geometries were be varied and this parameter will be used in this comparison. Mesh operations have been added on the quartz capillary tube and on the surface of the main resonator geometries to reduce

[1] The files can be found at *https://github.com/jsidabras/HFSSTutorial* and the Ansys *aedt* file has 4 projects to be solved.

numerical fluctuations and obtain a field profile void of discontinuities.

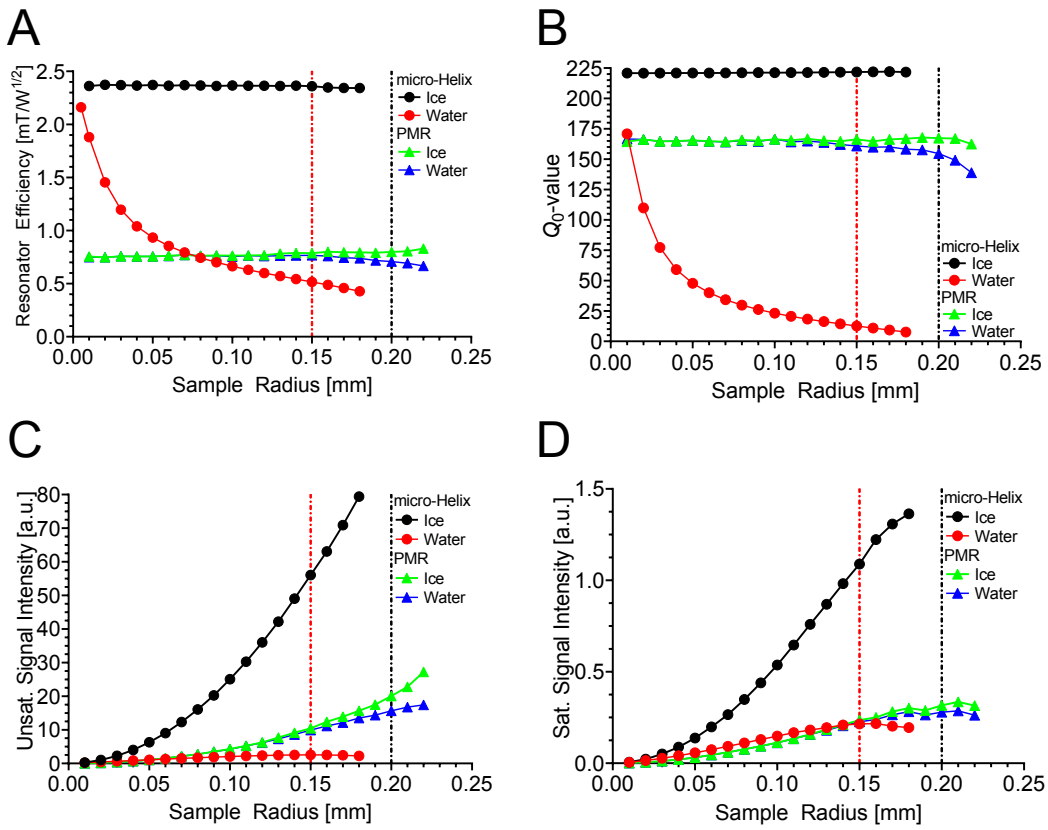

Figure 5.3.: EPR characteristics for the PMR with sapphire substrate (▲) and the 0.4 mm micro-helix (●) with a water or ice sample. Shown are the EPR characteristics as the sample radius is swept for the A) resonator efficiency Λ_{ave}, B) Q_0-value, C) unsaturated EPR signal, and D) saturable EPR signal. The dashed-dot lines indicate the largest practical capillary inner radius for the helix (red) and PMR (black).

Shown in Fig. 5.3 are the simulated EPR characteristics for the micro-helix (●) and planar micro-resonator (▲) geometries. The simulations were completed using an ice sample and an aqueous sample (water) and were plotted with colors shown in the legend. The sample radius was swept and a quartz sample holder with a wall thickness of 0.025 mm was used as a capillary. The dashed-dot line indicates the largest commercially available practical capillary inner radius for the helix (red) and PMR (black). In this study, a "concentration sensitivity" comparison was made where the resonator performance is evaluated assuming a varying sample volume at a fixed concentration.

For the PMR (▲), little change in both the average resonator efficiency Λ_{ave} and Q_0-value is exhibited as the sample radius is increased, Figs. 5.3A and 5.3B, respectively. From the simulations, the electric field (which gives rise to losses) is well contained in the planar micro-resonator geometry away from the sample loop. Shown in Fig. 5.4A is a plot of the magnitude of the electric field. A potential is formed across the PMR gap and a gradient of charge is formed in the loop which goes to zero opposite of the gap. This is similar to the electric field profile of a one-loop–one-gap loop-gap resonator.

In the PMR, the value of Λ_{ave} is approximately one-third of the micro-Helix (●;

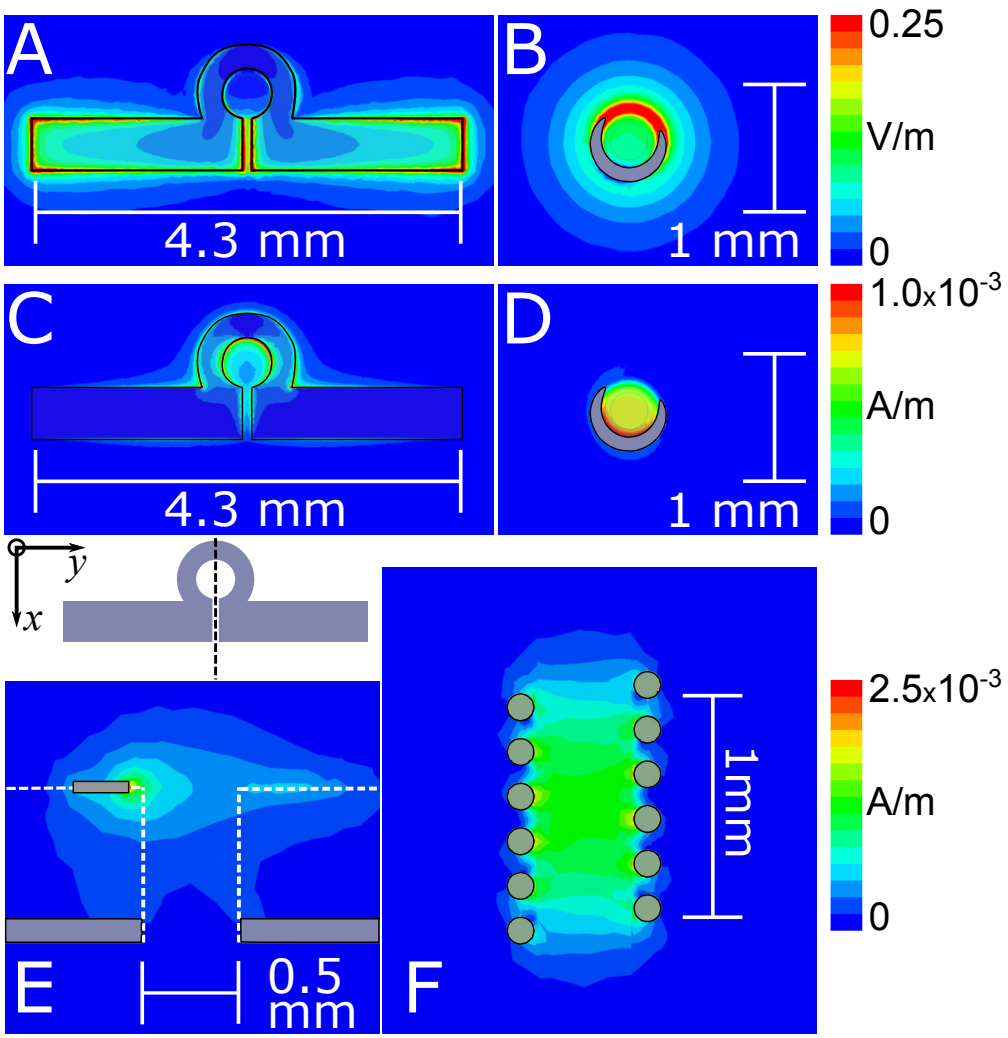

Figure 5.4.: Simulated field distribution for the magnitude of the electric field for the A) planar micro-resonant (PMR) and B) micro-helix and the magnitude of $\mathbf{H}_{1r}$ with $\mathbf{H}_0$ in the y-direction for the C) PMR and D) micro-helix in the x-y-plane. And the magnitude of $\mathbf{H}_{1r}$ with $\mathbf{H}_0$ in the y-direction for the E) PMR and F) micro-helix in the x-z-plane with a normalized voltage input.

in Fig. 5.3A). The reduction in Λ_{ave} is due to a significant portion of the magnetic field stored energy that is located outside of the sample volume in the PMR geometry and significant inhomogeneity of the magnetic field along the axis. This is illustrated in Fig. 5.4C where the magnitude of $\mathbf{H}_{1r}$ with $\mathbf{H}_0$ in the y-direction is plotted. As illustrated, a significant portion of this magnetic field lies outside of the sample region. This is also true along the axis, shown in Fig. 5.4E, where a large gradient of $\mathbf{H}_{1r}$ is present.

With the micro-helix geometry, the $\mathbf{H}_{1r}$ is concentrated in the center and a very little magnetic field is found outside of the sample volume, shown in Fig. 5.4D. Additionally, the $\mathbf{H}_{1r}$ field profile along the axis is more homogeneous compared to the PMR, as shown in Fig. 5.4F. Normalized $\mathbf{H}_{1r}$ squared, which is proportional to signal, on-axis for both the PMR and micro-helix is plotted in Fig. 5.5. The more homogeneous magnetic field in the micro-helix leads to a higher filling factor η and, ultimately, a higher average

resonator efficiency Λ_{ave}, as shown in Fig. 5.3A.

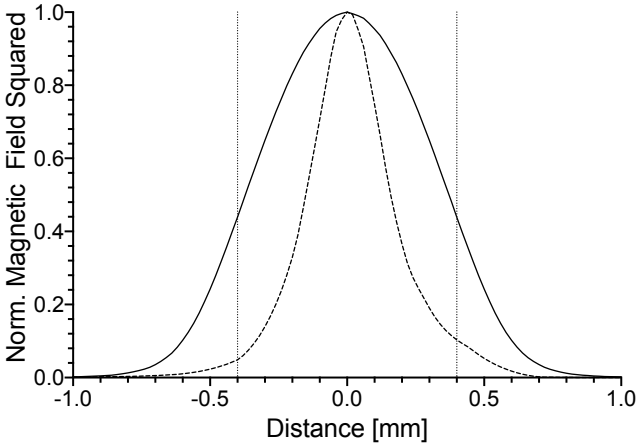

Figure 5.5.: Magnetic Field Squared on axis of the micro-helix (solid) and PMR (dashed) is plotted.

As anticipated from Eqn. 2.29, relatively lossless samples will display EPR unsaturable signal growth that is proportional to the magnetic field squared within the sample volume, shown in Fig. 5.3C for the micro-helix (black; ●) and PMR (green; ▲). With such samples, the EPR signal expected by using the micro-helix is significantly enhanced compared to the PMR. In contrast, the saturable sample defined by Eqn. 2.28 has a maximum due to the interplay of the power loss P_l and the magnetic field in the sample. Since the micro-helix exhibits an azimuthal component of the electric field that penetrates the sample, shown in Fig 5.4B, lossy aqueous samples are problematic in this geometry. Likewise, the resonator efficiency Λ_{ave} and Q_0-values are significantly reduced as the diameter of the aqueous sample increases, shown in Fig. 5.3A and 5.3B, respectively.

Aqueous sample simulations show that the PMR losses do not increase with the size of the sample and little changes of the unsaturable and saturable signal are illustrated, shown as blue in Figs. 5.3C and 5.3D. Compared to the micro-helix geometry with lossy aqueous samples, the PMR performs 5 times better for experiments at the same microwave power (unsaturable signal) and 50% better for the experiments at the same microwave field (saturable signal). This means the PMR geometry may be advantageous for room temperature samples and further improvements to the PMR to increase the uniformity and filling factor η are underway.

This example assumed the sample tube was filled and extends beyond the active region. It is noted that the active length of the two resonators are different. The data plotted in Fig. 5.3 was normalized to the active volume and a comparison of the "absolute sensitivity" was performed. Based on the magnetic field profile of Figs. 5.4E and 5.4F, the active region of the micro-helix and planar micro-resonator are assumed to be 1.2 mm and 1.1 mm, respectively, and a volume normalized signal is plotted in Fig. 5.6.

At a fixed sample volume, the losses in the micro-helix associated with the aqueous sample still significantly affect the performance of the resonator. Plotted in Figs. 5.6A and 5.6B as a solid line for the micro-helix (●). However, compared to the PMR (▲) there exists some sample volumes where the micro-helix yields a higher EPR signal. Finally, at a fixed sample volume and a relatively lossless sample, the micro-helix significantly outperforms the PMR geometry, plotted in Figs. 5.6A and 5.6B.

These simulations demonstrate that the self-resonant micro-helix should be used pri-

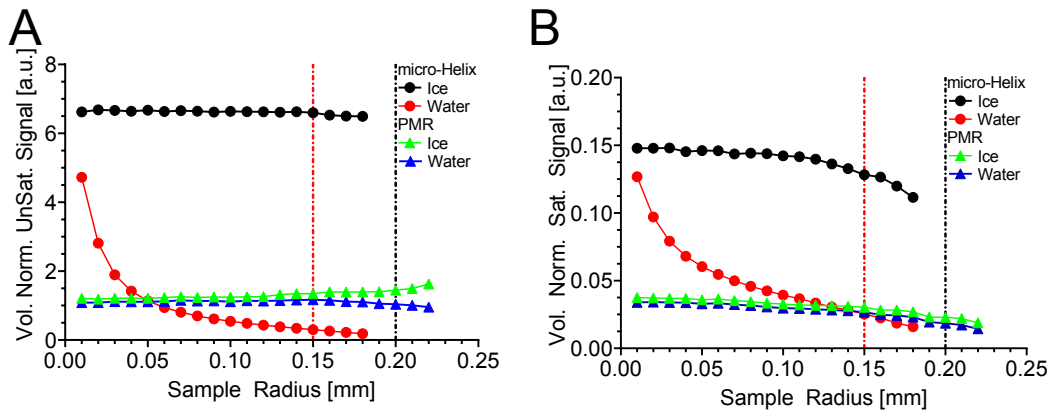

Figure 5.6.: Volume normalized Swept EPR signal for the PMR with sapphire substrate (black; ▲) and the 0.4 mm micro-helix (red; ●) with a water (solid) and ice (dashed) sample. Shown are the data from the A) unsaturated EPR signal and B) saturable EPR signal normalized to sample volume. The active region of the micro-helix and planar micro-resonator is assumed to be 1.2 mm and 1.1 mm, respectively. The dashed-dot line indicates the largest practical capillary inner radius for the helix (red) and PMR (black).

marily for frozen or lossless samples. However, for extremely small aqueous sample volumes (<9 nl), the micro-helix outperforms the PMRs. This is primarily due to the PMR planar geometry which limits the Q-value (50-180) and produces a strong inhomogeneity of the microwave magnetic field compared to the microwave magnetic field of the self-resonant micro-helix.

5.2.3. Experimental Comparison of Resonators.

The PMRs were fabricated by printing the micro-resonator geometry on a substrate using photo-lithographic techniques.[5.15, 5.16, 5.18] PMRs show significant improvement in absolute spin sensitivity compared to the best commercial probeheads available.[5.25] PMRs can be produced relatively cheaply using semiconductor etching techniques and laser scribing and configured for many frequencies with inner diameter sample sizes of 20-1000 μm. Furthermore, these structures offer excellent filling factors, high resonator efficiencies, and minimal power dissipation. It was recently demonstrated that a planar micro-resonators with Rogers RO6010LM substrate and a 500 μm sample diameter can be successfully employed for the study of crystals of inorganic metal complexes as well as [NiFe]-hydrogenase ($0.35 \times 0.2 \times 0.2$ mm^3) at 14 GHz, equipped with a specially designed cryogenic receiver at a temperature of 12 K.[5.17] Yet, such designs require a modified bridge to accommodate the cryogenic amplifier setup.

Improvement of the Q-value of the PMR geometry is reported here. By changing the substrate from Rogers RO6010LM substrate to single-crystal sapphire the Q-value increases by a factor of 3 and matches the simulations in Fig. 5.6B. The reduction of the Q-value using the Rogers RO6010LM substrate was not just due to the loss tangent of the material but partially due to surface roughness which gives rise to Ohmic losses.

The self-resonant micro-helix geometry wound around a 0.4 mm capillary is shown in Fig. 5.1A. The final number of the micro-helix windings was determined by the pitch of the helix, the quartz capillary sample tube (0.4 mm outer diameter 0.3 mm inner

diameter), and the surrounding Rexolite which all affect the resonance frequency. The fabricated 6.5-turn micro-helix had a resonant frequency around 9.7 GHz when coupled to the printed-circuit board inductive coupler.

Simulated comparison of the fabricated micro-helix geometry with commercial (Bruker MD5W1 and Bruker MS3) and state-of-the-art (PMR; based on Rogers RO6010LM printed-circuit board or sapphire substrates) microwave probes is provided in Tables 5.1 and 5.2. Simulations were performed assuming a fixed sample geometry of 0.1 mm diameter by 0.1 mm height cylindrical sample. The simulated sample allows for absolute sensitivity comparisons amongst the resonator designs.

Table 5.1.: Resonator EPR signal characteristics calculated and measured for a fixed sample geometry.

	UnSat. Signal		Sat. Signal	
Geometry	Calc.	Meas.	Calc.	Meas.
Bruker MD5W1	1.0	1.0	1.0	1.0
Bruker MS3	1.5	1.2	1.0	1.0
PMR RO6010LM	4.4	1.2	0.9	1.2
PMR Sapphire	18.6	13.3	3.9	3.8
Micro-Helix	35.7	28.2	6.1	5.7

Table 5.2.: Resonator characteristics calculated and measured.

	DR	LGR	PMR		
Geometry	MD5W1	MS3	6010LM	Sapphire	Micro-Helix
Freq. Calc.	9.67	9.67	9.87	9.87	9.78
Freq. Meas.	9.69	9.69	9.58	9.58	9.73
Q_0-value Calc.	8860	870	90	190	360
Q_0-value Meas.	6650	600	61	181	220
Λ Calc. [mT/W$^{1/2}$]	0.60	0.68	1.9	2.9	4.1
Λ_{ave} Calc. [mT/W$^{1/2}$]	0.60	0.68	1.5	2.6	4.0
$P_{1/2}$ Meas. [mW]	19.2	18.4	17.3	1.8	0.8
Λ_{ave} Meas. [mT/W$^{1/2}$]	–	–	–	2.2	3.2

Power Saturation Measurements in All Resonators Experimentally, a minuscule amount of lithium phthalocyanine (LiPC)[5.49] is embedded in Crytoseal (or similar) wax and was used as a point sample. The LiPC sample produces a very sharp line width (less than 0.05 mT) in the presence of oxygen (narrower without oxygen present), saturates at large values of $\mathbf{H}_{1r}$, and very little sample volume is needed to observe the signal. Therefore the use of LiPC allows for a fair comparison between all resonators by using the same sample throughout the experiments.[2]

Power saturation experiments that were performed with the LiPC sample are plotted in Fig. 5.7. From the power saturation data, EPR characteristics for each resonator can be ascertained and tabulated in Tables 5.1 and 5.2. The unsaturable signal was measured at constant microwave power (0.01 mW), while the saturable signal was measured at the

[2]The term "minuscule" is defined as enough sample to observe a signal in the Bruker MD5W1 without causing line broadening in the micro-helix geometry. Such line broadening is due to a radiation dampening-like behavior caused by the large filling factor η.

power where the EPR signal amplitude is maximum ($P_{1/2}$-value; indicated by $\diamond$). At the $P_{1/2}$-value, the B_{1r} incident on the sample is identical in each of the resonators. For the power saturation experiments used in this work, the microwave power was stepped in 3 dB increments from 200 mW to 0.2 μW (0-60 dB). Each scan was 30 s over 1 mT with 4096 pts, receiver gain of 60 dB and 100 kHz field modulation at 0.1 mT in all resonators. The over-modulation of the LiPC sample was used to increase the sensitivity in the Bruker commercial resonators while increasing the intrinsic line width (line-height–line-width compromise, discussed in Ref. [5.50]).

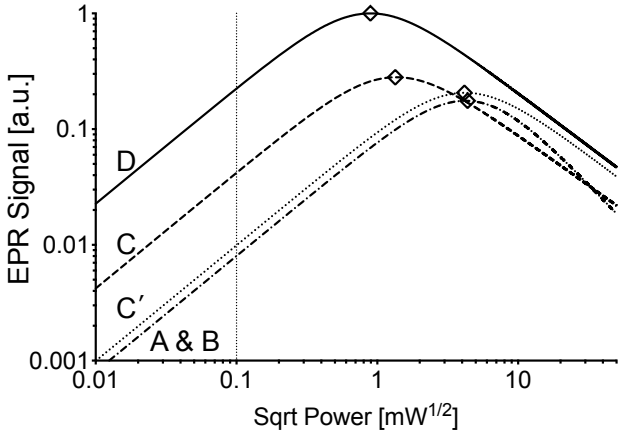

Figure 5.7.: Power saturation data of LiPC showing the A) Bruker MD5 (dash-dot), and B) Bruker MS3, Ω-type PMR with 0.5 mm sample loop with C) sapphire substrate (dashed) and C′) Rogers 6010LM substrate (dotted), and D) micro-helix (solid). EPR saturable signal is taken at peak signal ($P_{1/2}$-value, constant microwave field; indicated by $\diamond$), while EPR unsaturable signal is taken at 0.01 mW (constant microwave power; dotted line).

As described in Table 5.1, if the EPR signal cannot be saturated (UnSat.; Eqn. 2.29) a factor of approximately 28 can be achieved compared to commercially available probe-heads. EPR signals that cannot be saturated are proportional to the square root of the incident microwave power and, therefore, the EPR signal intensity is only limited by the amount of power available. However, most protein samples saturate readily, and, as such, the maximum signal that can be obtained is determined by the microwave magnetic field at the sample. When the sample is saturable (Sat.; Eqn. 2.28), a factor of 5.7 can be achieved. The micro-helix exhibits the highest absolute sensitivity with no modification to the commercial bridge.

The ratio of two $P_{1/2}$-values can be compared to the square of the ratio of Λ_{ave}. The data for the Bruker MS3 and MD5W1, in our hands, lay on top of each other for the LiPC point sample.

Measurement of Λ_{ave} in the PMR and micro-Helix In order to measure the B_{1r} directly, a series of pulse nutation experiments were performed.[5.1] The pulse nutation experiments were performed with an echo detected EPR signal using a 40 ns $\pi/2$ pulse and a pulse separation of 300 ns. An HA6047 300 W amplifier (HBH Microwave GmbH, Stutensee, DE) was used for all resonators and the power attenuation was adjusted for a maximum echo. From the nutation experiment oscillations, Eqn. 2.43 is used to solve for B_{1r} in Gauss and f_{rab} is equal to the inverse of the time in seconds for a whole (2π) oscillation. The value of B_{1r} is converted to mT (divide by 10) and normalized to the

incident power by,

$$\Lambda_{ave} = \frac{B_{1r}}{(P/2^{\zeta/3})^{1/2}} \qquad [\mathrm{mT/W^{1/2}}], \tag{5.2}$$

where P is the maximum power available (in this case, 300 W) and ζ is the attenuation of that power set on the console in dB.

The sample was a 2% w/w BDPA (α,γ-bisdiphenylene-β-phenylallyl; Sigma-Aldrich Chemicals; CAS number 35585-94-5) in polystyrene. The PS and BDPA were fully dissolved in toluene, laid out onto a covered Pyrex Petri dish, and left to evaporate for several days. The sample was then cut and placed in the sample tube for further testing. For direct measurement of Λ_{ave}, an EPR nutation experiment was performed at three pulse powers using the 2% w/w BDPA in polystyrene and cut to $0.55 \times 0.18 \times 0.08$ mm^3. The micro-helix has a measured power conversion efficiency parameter of 3.2 mT/W$^{1/2}$ which corresponds, for an $S = 1/2$ spin system with a g-value of 2, to a $\pi/2$ pulse of 20 ns with an incident power of only 20 mW. No signal was measurable in the PMR RO6010LM, MS3, and MD5W1 due to a lack of sensitivity. However, the PMR with a sapphire substrate has a good efficiency parameter of 2.2 mT/W$^{1/2}$ which corresponds, for an $S = 1/2$ spin system with a g-value of 2, to a $\pi/2$ pulse of 20 ns with an incident power of approximately 40 mW. These data were tabulated in Table 5.2.

5.2.4. EPR of Photosystem II tyrosine D radical

In the previous section, it was shown that the self-resonant micro-helix outperforms both the commercial resonators and state-of-the-art PMR resonators in EPR experiments with standard samples. To further benchmark the micro-helix geometry a protein sample, specifically, photosystem II is measured. In photosystem II, water oxidation takes place at the tetranuclear manganese cluster, with a redox-active tyrosine radical ($Y_Z^\bullet$) as an interface to the light-induced electron transfer process,[5.51] shown in Fig. 5.8.[3] Symmetrically to $Y_Z^\bullet$, a long-lived tyrosine radical ($Y_D^\bullet$) exists in the second branch of the photosystem II which contains no manganese cluster. In this work, the $Y_D^\bullet$ radical was used as a standard probe because it is stable for several hours under ambient conditions[5.52] and has been well-characterized using a variety of EPR techniques.[5.6, 5.53] The hyperfine interactions from several protons, both on the phenyl ring and distal CH_2 carbon, lead to the distinct splittings of the radical (S=1/2). To generate the tyrosine radical ($Y_D^\bullet$) EPR signal, the photosystem II core complex samples were illuminated in ambient light and rapidly frozen.

The tyrosine D radical ($Y_D^\bullet$) of photosystem II was measured in two forms: (i) a frozen solution sample of photosystem II (BBY particles)[5.23] placed in a 0.3 mm inner diameter capillary and (ii) a $0.3 \times 0.18 \times 0.18$ mm^3 single crystal of photosystem II core complexes.[5.24] In both photosystem II samples, the $Y_D^\bullet$ and first ligand-sphere are known to be identical. These samples provide a benchmark for future work.

Frozen solution EPR of Photosystem II tyrosine D radical ($Y_D^\bullet$). Shown in Fig. 5.9 is the $Y_D^\bullet$ radical EPR signal in an 85 nl frozen solution from photosystem II (BBY particles) at a temperature of 80 K using the self-resonant micro-helix. A continuous-wave EPR experiment, shown in Fig. 5.9A, was performed on an Elexsys E580 X-band bridge by sweeping 10 mT in 1 minute (4096 points) with a modulation rate of 100 kHz and an amplitude of 0.5 mT. The data was averaged 49 times for a total of 49 minutes at an incident power of 0.2 μW. To further improve the signal-to-noise

[3] Ref. [5.51] is distributed under the terms of the Creative Commons Attribution 4.0 International License (*http://creativecommons.org/licenses/by/4.0/)*

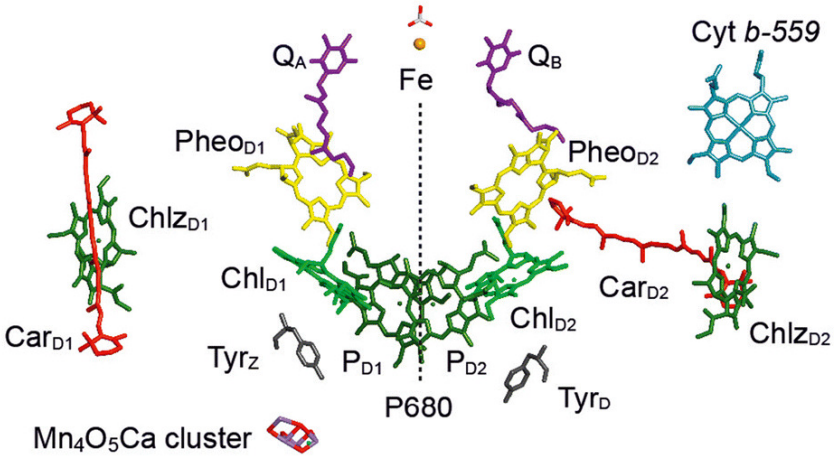

Figure 5.8.: Photosystem II core complex. The figure is modified from Ref. [5.51] and reproduced with permission.[3]

ratio of the continuous-wave experiment, a field-swept non-adiabatic rapid scan (NARS) experiment was performed, data are shown in Fig. 5.9B. The field-swept non-adiabatic rapid scan (NARS) experiment was performed on the same commercial hardware using the rapid-scan method of Möser *et al.*[5.54] and processed with the method described in Hyde *et al.*[5.55] Herein, the scan rate was a sinusoidal 100 kHz field-sweep at 1 mT amplitude and a field-step size of 0.05 mT. The collected real and imaginary, pure-absorption and pure-dispersion, spectra were pseudo-modulated with a 0.5 mT moving difference (MDIFF)[5.55] to compare to the field-modulated continuous-wave experiment. A factor of 2 in signal-to-noise improvement was obtained for the same signal acquisition time.

A field-swept two-pulse electron spin-echo (ESE) EPR experiment was performed on the same commercial hardware over an 8 mT sweep, shown in Fig. 5.9C. The field-swept ESE data was pseudo-modulated with a 0.5 mT MDIFF to compare the experiment with the field-modulated continuous-wave experiment of Fig. 5.9A. The signal-to-noise ratio for all three experiments was calculated and tabulated in Table 5.3.

Table 5.3.: Signal-to-noise calculations for the three experiments performed on the photosystem II $Y_D^{\bullet}$ radical in frozen solution at a temperature of 80 K. Approximately 1.6×10^{12} spins were calculated to be in the 85 nl that fill the micro-helix.

Experiment	SNR Re.	SNR Im.	Time
Continuous Wave	197	131	49 min
NARS	4400	2300	55 min
NARS (MDIFF)	410	423	–
ESE	248	–	45 min
ESE (MDIFF)	106	–	–

Finally, a comparison between the MD5W1 dielectric resonator and the self-resonant micro-helix was performed with the frozen solution photosystem II (BBY particle) sample at a temperature of 80 K. A continuous-wave EPR experiment was performed to compare the EPR signal obtained with 85 nl volume in the micro-helix. The photosystem II

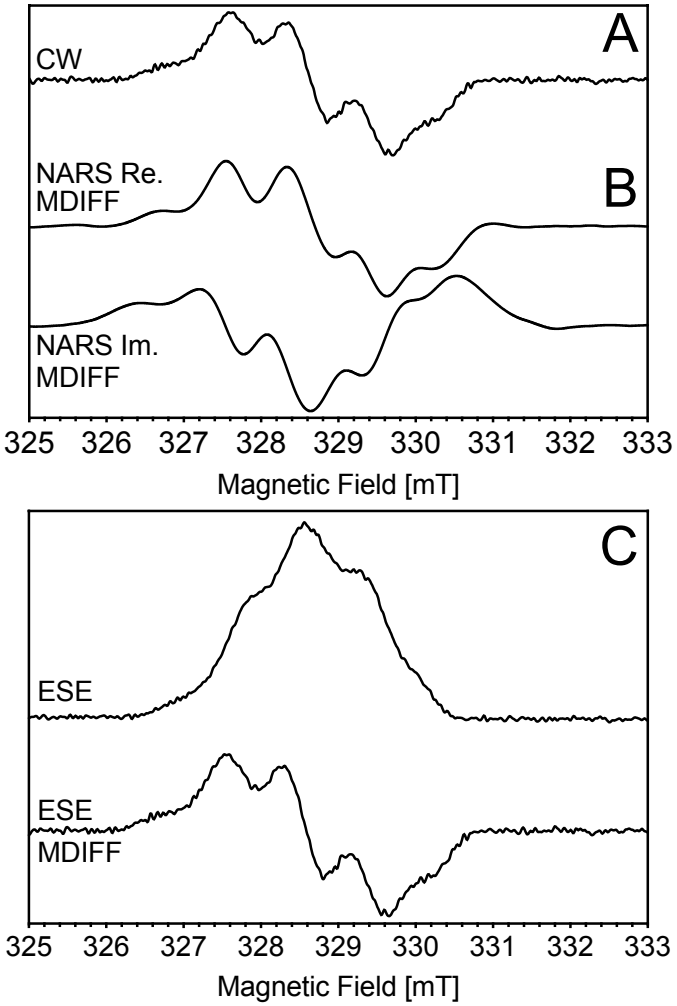

Figure 5.9.: Three frozen solution experiments with $Y_D^\bullet$ in photosystem II at 80 K were performed: A) continuous-wave, B) real and imaginary NARS, and C) ESE experiments. Calculated moving difference (MDIFF) pseudo-modulation of 0.5 mT is shown for the NARS and field-swept ESE experiments to directly compare to the continuous-wave EPR experiment.

sample was placed in a 0.3 mm inner diameter quartz tube with a sample height of 9 mm (636 nl) and centered in the dielectric cavity. A signal-to-noise ratio of approximately 300 was calculated for a sample volume of 636 nl, shown in Fig. 5.10. The spectrum was collected by sweeping 10 mT in 1 minute (4096 points) with a modulation rate of 100 kHz and an amplitude of 0.5 mT. The data were averaged 49 times for a total time of 49 minutes at an incident power of 3.1 μW. This power was chosen to compare the two samples at approximately the same B_{1r} incident on the sample. Normalizing the signal-to-noise ratio with the volume yields a factor of approximately 5 improvement in absolute spin sensitivity using the self-resonant micro-helix compared to the MD5W1. These experiments serve to show the versatility of the micro-helix to perform EPR experiments on limited sample volumes (less than 85 nl) at X-band frequencies.

Single-Crystal continuous-wave EPR of the tyrosine D radical ($Y_D^\bullet$) in the photosystem II core complex. Shown in Fig. 5.11 is continuous-wave EPR data

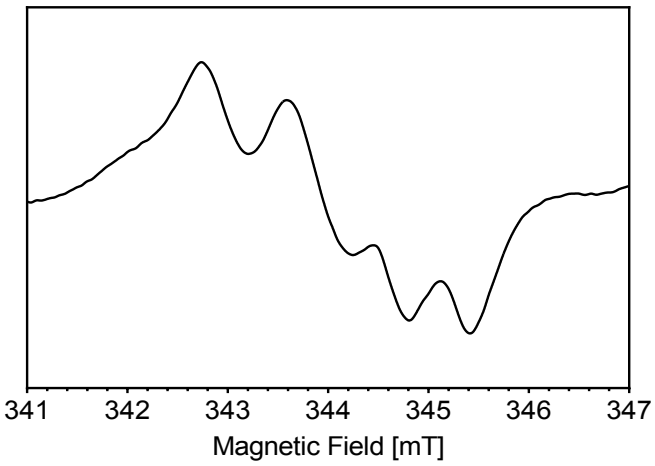

Figure 5.10.: Continuous-wave EPR of frozen solution photosystem II sample performed in the Bruker MD5W1 dielectric resonator at a temperature of 80 K. A signal-to-noise ratio of approximately 300 is calculated for a sample volume of 636 nl.

collected at two separate angles of the photosystem II $Y_D^\bullet$ radical in a single crystal at a temperature of 80 K as a sensitivity test for the 0.4 mm inner diameter self-resonant micro-helix. The photosystem II core complex crystal had a volume of 0.3 × 0.18 × 0.18 mm^3. The spectra were collected by sweeping 15 mT in 1 minute (4096 points) with a modulation rate of 100 kHz and an amplitude of 0.3 mT. The data were averaged 49 times for a total time of 49 minutes at an incident power of 0.2 μW. Simulations using the known g-tensor and hyperfine tensors[5.6] were performed with an Easyspin (http://easyspin.org; Ref. [5.56]) global fit routine to find the crystal orientation and plotted in red in Fig. 5.11. At X-band, the g-anisotropy of the $Y_D^\bullet$ radical is very small and is not resolved. Instead, the orientation dependence is primarily determined by the hyperfine interaction pattern of the coupled proton nuclei.[5.6] Using only two angles, a unique fit cannot be found, but a demonstration of the $Y_D^\bullet$ features are shown. A non-specifically bound Mn^{2+} signal was also present in the crystal, yielding the signals indicated by an asterisk ($*$).

The use of photosystem II crystals as a benchmark provides a challenging system to measure. The photosystem II core complex has a molecular weight of approximately 455 kDa as a monomer and each complex contains only one $Y_D^\bullet$ radical. Approximately 8.9×10^{12} $Y_D^\bullet$ radicals were present in the sample with a crystal size of 0.3 × 0.18 × 0.18 mm^3 and the crystal space group $P2_1\,2_1\,2_1$. These data demonstrate the versatility of the micro-helix to study large complexes in small crystal dimensions. A photosystem II core complex crystal can be routinely grown to dimensions of 0.3 mm but requires significant effort to increase in size. Finally, the $Y_D^\bullet$ radical is easily saturable with large microwave magnetic fields, which limits the available microwave power and maximum EPR signal at a given temperature. Despite these challenges, a signal-to-noise of approximately 35 was calculated for the $Y_D^\bullet$ radical in the single-crystal sample.

Qualitative Sensitivity Comparison of the X-band micro-helix to High-frequency single-mode resonators. Simulations were performed in Ansys HFSS comparing a cylindrical TE_{011} cavity at W-band frequencies (95 GHz) to the micro-helix geometry at X-band frequencies using an 85 nl frozen solution sample. Assuming no

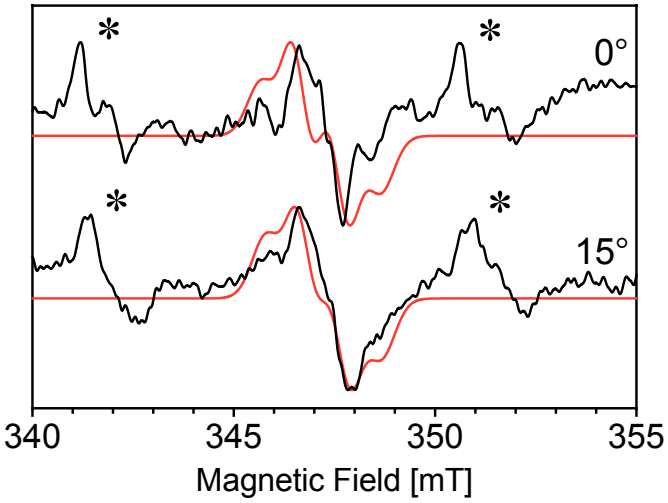

Figure 5.11.: Single-Crystal continuous-wave EPR of $Y_D^{\bullet}$ in photosystem II core complex. Continuous-wave EPR collected with the 0.4 mm inner diameter self-resonant micro-helix at two angles of the photosystem II $Y_D^{\bullet}$ radical from a single crystal at a temperature of 80 K. The crystal size was 0.3 × 0.18 × 0.18 mm^3. Shown in red is a fitted simulation with similar features. A non-specifically bound Mn^{2+} signal is also present in the mother-liquor of the crystal, indicated by an asterisk (∗). Each spectrum was collected in 49 minutes with a signal-to-noise ratio of approximately 35.

g-anisotropy, the W-band TE_{011} exhibits a factor of approximately 3 in improved EPR signal intensity compared to the micro-helix geometry at X-band frequencies. However, for example, the g-anisotropy at W-band spreads the tyrosine D radical in the photosystem II spectrum by a factor of 2 (see Fig. 2 in Ref. [5.6]); for some systems, the g-anisotropy may be more severe. Therefore, the micro-helix EPR sensitivity at X-band is comparable to a standard W-band system with a cylindrical TE_{011} cavity.

As the frequency becomes even higher, the resonator efficiency decreases due to losses on the surface of the resonator. For example, the Bruker 263 GHz single-mode resonator has a reported Λ_{ave}-value of 0.7 $mT/W^{1/2}$.[5.57] This is approximately half of the cylindrical TE_{011} cavity at W-band. The lower Λ_{ave} leads to only a factor of five in EPR signal improvement compared to the micro-helix at X-band. However, g-anisotropy becomes more severe as the operating frequency increases.

Therefore, the micro-helix geometry opens up the possibility to perform multi-frequency EPR on the same sample from X-band to 263 GHz. Using a 0.4 mm outer diameter capillary, a sample can be placed in the micro-helix at X-band and the same sample can then be inserted into a W-band or 263 GHz cavity. This ability allows for complementary techniques to be used for disentangling the angle dependencies of hyperfine-tensor interactions.

5.3. Conclusions and Outlook

An application of the self-resonant micro-helix geometry and planar-coupling structure that increases the EPR absolute spin sensitivity by a factor of approximately 30, if the signal is unsaturable, and 6, if the EPR signal can be saturated, was presented. For

saturable EPR signals, such as those found in protein samples, the self-resonant micro-helix saves up to a factor of 32 in measuring time. From this gain of EPR sensitivity, the self-resonant micro-helix is well-suited for EPR studies on protein single-crystals with dimensions less than 0.3 mm.

Due to the very high efficiency parameter of 3.2 $\mathrm{mT/W^{1/2}}$, which corresponds to a $\pi/2$ pulse of 20 ns with an incident power of only 20 mW, the micro-helix geometry is advantageous in extending pulse EPR to experiments that usually require costly high-power microwave amplifiers (e.g. HYSCORE), further expanding the applicability of pulse EPR. This work also demonstrates that the self-resonant micro-helix performs well for field-swept non-adiabatic rapid scan (NARS) techniques due to its small size and "open" structure, which increases the continuous-wave EPR spin sensitivity further by a factor of 2 for the same experimental time. With a NARS experiment a the self-resonant micro-helix is measured to have an absolute spin sensitivity of 63.5×10^6 Spins/G in 85 nl of sample for 50 minutes of collection time. Due to the relatively large bandwidth of the micro-helix (90 MHz critically-coupled), this geometry is particularly well-suited for frequency-swept NARS and rapid scan experiments which further improve the signal-to-noise ratio for saturable samples [5.54, 5.55] and for the use of arbitrary-waveform generators for advanced pulse spectroscopy. [5.1, 5.2, 5.58]

The micro-helix Q-value and high-efficiency parameter Λ_{ave} significantly reduces the dead-time making the resonator suitable for experiments that record the onset of the EPR signal during pulses. For example, assuming a typical X-band bandwidth of 70 MHz and a Q_0-value of 1000, a β of 6.5 is needed to over-couple the cavity to the desired bandwidth. By also assuming it takes 15-time constants (factor of 2 for voltage detection), the ring-down of the cavity can be calculated by

$$15 \times \tau_c = 15 \times 2 \times Q/2\pi\nu, \tag{5.3}$$

where ν is the frequency of interest. This produces a dead-time of 67 ns. For the micro-helix, with a critically-coupled measured Q_0-value of 220 the dead-time is 55 ns.[4] Assuming the micro-helix can be over-coupled by a β of 6.5, this leads to a dead-time of 15 ns. However, compared to the Bruker MS3, the micro-helix would need a factor of 10 less power for the same B_{1r}, lowering the number of time constants needed.

As this technology matures, further improvements to enhance the sensitivity based on new fabrication techniques and choice of other materials will be explored. Not only does the increase in sensitivity save time in EPR data measurements, but it also reduces the need for the availability of, or necessity to, grow larger crystals. Overall, the self-resonant micro-helix provides the possibility to study catalytically-active proteins at crystal dimensions relevant to X-ray crystallography diffraction and, as such, is a significant advancement in the field of enzyme research.

[4] While critically-coupled, the signal-to-noise is improved by a $\sqrt{2}$ compared to an over-coupled cavity.

CHAPTER 5. REFERENCES

[5.1] A. Schweiger, G. Jeschke, Principles of Pulse Electron Paramagnetic Resonance, Oxford University Press, 2001.

[5.2] D. Goldfarb, S. Stoll, EPR Spectroscopy: Fundamentals and Methods, eMagRes, Wiley, 2018.

[5.3] S. E. J. Bowman, J. Bridwell-Rabb, C. L. Drennan, Metalloprotein crystallography: More than a structure, Acc. Chem. Res. 49 (4) (2016) 695–702.

[5.4] W. Lubitz, E. Reijerse, M. van Gastel, [NiFe] and [FeFe] hydrogenases studied by advanced magnetic resonance techniques, Chem. Rev. 107 (10) (2007) 4331–4365.

[5.5] R. Hussein, M. Ibrahim, R. Chatterjee, L. Coates, F. Müh, V. K. Yachandra, J. Yano, J. Kern, H. Dobbek, A. Zouni, Optimizing crystal size of photosystem II by macroseeding: Toward neutron protein crystallography, Cryst. Growth Des. 18 (1) (2018) 85–94.

[5.6] W. Hofbauer, A. Zouni, R. Bittl, J. Kern, P. Orth, F. Lendzian, P. Fromme, H. T. Witt, W. Lubitz, Photosystem II single crystals studied by EPR spectroscopy at 94 GHz: the tyrosine radical $Y_D^b ullet$, PNAS 98 (12) (2001) 6623–6628.

[5.7] R. Klette, J. T. Törring, M. Plato, K. Möbius, B. Boenigk, W. Lubitz, Determination of the g-tensor of the primary donor cation radical in single crystals of rhodobacter sphaeroides R-26 reaction centers by 3-mm high-field EPR, J. Phys. Chem. 97 (9) (1993) 2015–2020.

[5.8] I. Krstić, B. Endeward, D. Margraf, A. Marko, T. F Prisner, Structure and dynamics of nucleic acids, Top. Curr. Chem. 321 (2011) 159–98.

[5.9] F. Neese, Quantum chemical calculations of spectroscopic properties of metalloproteins and model compounds: EPR and Mössbauer properties, Curr. Opin. Chem. Biol. 7 (1) (2003) 125–135.

[5.10] J. S. Hyde, W. Froncisz, Loop-gap resonators, in: A. J. Hoff (Ed.), Advanced EPR: Applications in Biology and Biochemistry, Elsevier, 1989, pp. 277–306.

[5.11] S. Friedländer, M. Šimėnas, M. Kobalz, P. Eckold, O. Ovchar, A. G. Belous, J. Banys, H. Krautscheid, A. Pöppl, Single crystal electron paramagnetic resonance with dielectric resonators of mononuclear Cu^{2+} ions in a metal–organic framework containing Cu_2 paddle wheel units, J. Phys. Chem. C 119 (33) (2015) 19171–19179.

[5.12] S. Friedländer, P. S. Petkov, F. Bolling, A. Kultaeva, W. Böhlmann, O. Ovchar, A. G. Belous, T. Heine, A. Pöppl, Continuous-wave single-crystal electron paramagnetic resonance of adsorption of gases to cupric ions in the Zn(II)-doped porous coordination polymer $Cu_{2.965}Zn_{0.035}(btc)_2$, J. Phys. Chem. C 120 (48) (2016) 27399–27411.

[5.13] R. R. Mett, J. W. Sidabras, J. R. Anderson, C. S. Klug, J. S. Hyde, Rutile dielectric loop-gap resonator for x-band epr spectroscopy of small aqueous samples, J. Magn. Reson. 307 (2019) 106585.

[5.14] R. R. Mett, J. W. Sidabras, J. S. Hyde, MRI surface-coil pair with strong inductive coupling, Rev. Sci. Instrum. 87 (12) (2016) 124704.

[5.15] R. Narkowicz, D. Suter, R. Stonies, Planar microresonators for EPR experiments, J. Magn. Reson. 175 (2) (2005) 275–284.

[5.16] R. Narkowicz, D. Suter, I. Niemeyer, Scaling of sensitivity and efficiency in planar microresonators for electron spin resonance, Rev. Sci. Instrum. 79 (8) (2008) 084702.

[5.17] R. Narkowicz, H. Ogata, E. Reijerse, D. Suter, a cryogenic receiver for EPR, J. Magn. Reson. 237 (2013) 79–84.

[5.18] R. Narkowicz, D. Suter, Tuner and radiation shield for planar electron paramagnetic resonance microresonators, Rev. Sci. Instrum. 86 (2) (2015) 024701.

[5.19] E. Ginzton, Microwave Measurements, McGraw-Hill, 1957.

[5.20] J. S. Hyde, J. W. Sidabras, R. R. Mett, Resonators for multifrequency EPR of spin labels, in: S. K. Misra (Ed.), Multifrequency Electron Paramagnetic Resonance: Theory and Applications, Wiley-VCH Verlag GmbH & Co. KGaA, 2011, Ch. 5.2, pp. 244–269.

[5.21] D. Schroeder, Astronomical Optics, Elsevier Science, 2000.

[5.22] A. Oppenheim, R. Schafer, J. Buck, Discrete-Time Signal Processing, Pearson Education, 1999.

[5.23] D. A. Berthold, G. T. Babcock, C. F. Yocum, A highly resolved, oxygen-evolving photosystem II preparation from spinach thylakoid membranes: EPR and electron-transport properties, FEBS Lett. 134 (2) (1981) 231–234.

[5.24] J. Kern, B. Loll, C. Lüneberg, D. DiFiore, J. Biesiadka, K.-D. Irrgang, A. Zouni, Purification, characterisation and crystallisation of photosystem II from Thermosynechococcus elongatus cultivated in a new type of photobioreactor, Biochim. Biophys. Acta, Bioenerg. 1706 (1) (2005) 147–157.

[5.25] E. Reijerse, A. Savitsky, Electron Paramagnetic Resonance Instrumentation, Vol. 6, eMagRes, 2017, pp. 187–206.

[5.26] S. Friedländer, O. Ovchar, H. Voigt, R. Böttcher, A. Belous, A. Pöppl, Dielectric ceramic EPR resonators for low temperature spectroscopy at X-band frequencies, Appl. Magn. Reson. 46 (1) (2015) 33–48.

[5.27] A. C. Torrezan, T. P. Mayer Alegre, G. Medeiros-Ribeiro, Microstrip resonators for electron paramagnetic resonance experiments, Rev. Sci. Instrum. 80 (7) (2009) 075111.

[5.28] A. Ghirri, C. Bonizzoni, M. Righi, F. Fedele, G. Timco, R. Winpenny, M. Affronte, Microstrip resonators and broadband lines for X-band EPR spectroscopy of molecular nanomagnets, Appl. Magn. Reson. 46 (2015) 749–756.

[5.29] Y. Twig, E. Dikarov, A. Blank, Ultra miniature resonators for electron spin resonance: Sensitivity analysis, design and construction methods, and potential applications, Mol. Phys. 111 (18–19) (2013) 2674–2682.

[5.30] Y. Twig, E. Suhovoy, A. Blank, Sensitive surface loop-gap microresonators for electron spin resonance, Rev. Sci. Instrum. 81 (10) (2010) 104703.

[5.31] W. M. Walsh, L. W. Rupp, Enhanced esr sensitivity using a dielectric resonator, Rev. Sci. Instrum. 57 (9) (1986) 2278–2279.

[5.32] I. Golovina, I. Geifman, A. Belous, New ceramic EPR resonators with high dielectric permittivity, J. Magn. Reson. 195 (1) (2008) 52–59.

[5.33] R. H. Webb, Use of traveling wave helices in ESR and double resonance spectrometers, Rev. Sci. Instrum. 33 (7) (1962) 732–737.

[5.34] J. C. Collingwood, J. W. White, Helical resonators for spin resonance spectroscopy, J. Sci. Instrum. 44 (7) (1967) 509.

[5.35] L. R. Adkins, A. W. Nolle, EPR spectrometer utilizing traveling wave helix for 2 Gc region, Rev. Sci. Instrum. 37 (10) (1966) 1404–1405.

[5.36] H. Mahdjour, W. G. Clark, K. Baberschke, High-sensitivity broadband microwave spectroscopy with small nonresonant coils, Rev. Sci. Instrum. 57 (6) (1986) 1100–1106.

[5.37] W. Froncisz, J. S. Hyde, the loop-gap resonator: A new microwave lumped circuit ESR sample structure, J. Magn. Reson. 47 (3) (1982) 515–521.

[5.38] D. L. Olson, T. L. Peck, A. G. Webb, R. L. Magin, J. V. Sweedler, High-resolution microcoil ^{1}H-NMR for mass-limited, nanoliter-volume samples, Science 270 (5244) (1995) 1967–1970.

[5.39] R. Subramanian, M. Lam, A. Webb, RF microcoil design for practical NMR of mass-limited samples, J. Magn. Reson. 133 (1) (1998) 227–231.

[5.40] M. E. Lacey, R. Subramanian, D. L. Olson, A. G. Webb, J. V. Sweedler, High-resolution NMR spectroscopy of sample volumes from 1 nl to 10 *mu*l, Chem. Rev. 99 (10) (1999) 3133–3152.

[5.41] A. P. M. Kentgens, J. Bart, P. J. M. van Bentum, A. Brinkmann, E. R. H. van Eck, J. G. E. Gardeniers, J. W. G. Janssen, P. Knijn, S. Vasa, M. H. W. Verkuijlen, High-resolution liquid- and solid-state nuclear magnetic resonance of nanoliter sample volumes using microcoil detectors, J. Chem. Phys. 128 (5) (2008) 052202.

[5.42] R. M. Fratila, A. H. Velders, Small-volume nuclear magnetic resonance spectroscopy, Annu. Rev. Anal. Chem. 4 (1) (2011) 227–249.

[5.43] C. J. Jones, C. K. Larive, Could smaller really be better? Current and future trends in high-resolution microcoil NMR spectroscopy, Anal. Bioanal. Chem. 402 (1) (2012) 61–68.

[5.44] M. Mompeán, R. M. Sánchez-Donoso, A. de la Hoz, V. Saggiomo, A. H. Velders, M. V. Gomez, Pushing nuclear magnetic resonance sensitivity limits with microfluidics and photo-chemically induced dynamic nuclear polarization, Nat. Commun. 9 (1) (2018) 108–108.

[5.45] M. Mossakowski, J. Koprowski, A helical-coil resonator magnetically coupled with microstrip transmission line for EPR spectroscopy, Materiały Elecktroniczne 37 (4) (2009) 3–8.

[5.46] A. Webb, Microcoil nuclear magnetic resonance spectroscopy, J. Pharm. Sci. 38 (5) (2005) 892–903.

[5.47] W. J. Ellison, Permittivity of pure water, at standard atmospheric pressure, over the frequency range 0–25THz and the temperature range 0–100C, J. Phys. Chem. Ref. Data 36 (1) (2007) 1–18.

[5.48] J. H. Jiang, D. L. Wu, Ice and water permittivities for millimeter and sub-millimeter remote sensing applications, Atmos. Sci. Lett. 5 (2004) 146–151.

[5.49] K. J. Liu, P. Gast, M. Moussavi, S. W. Norby, N. Vahidi, T. Walczak, M. Wu, H. M. Swartz, Lithium phthalocyanine: A probe for electron paramagnetic resonance oximetry in viable biological systems, Proc. Natl. Acad. Sci. 90 (12) (1993) 5438–5442.

[5.50] G. Eaton, S. Eaton, D. Barr, R. Weber, Quantitative EPR, Springer Vienna, 2010.

[5.51] W. Lubitz, M. Chrysina, N. Cox, Water oxidation in photosystem II, Photosynth. Res. 142 (1) (2019) 105–125.

[5.52] K. Saito, A. W. Rutherford, H. Ishikita, Mechanism of tyrosine D oxidation in photosystem II, Proc. Natl. Acad. Sci. 110 (19) (2013) 7690–7695.

[5.53] S. Styring, J. Sjöholm, F. Mamedov, Two tyrosines that changed the world interfacing the oxidizing power of photochemistry to water splitting in photosystem II, Biochim. Biophys. Acta, Bioenerg. 1817 (1) (2012) 76–87.

[5.54] J. Möser and K. Lips and M. Tseytlin and G.R. Eaton and S.S. Eaton and A. Schnegg, Using rapid-scan EPR to improve the detection limit of quantitative EPR by more than one order of magnitude, J. Magn. Reson. 281 (2017) 17–25.

[5.55] J. S. Hyde, B. Bennett, A. W. Kittell, J. M. Kowalski, J. W. Sidabras, Moving difference (MDIFF) non-adiabatic rapid sweep (NARS) EPR of copper(II), J. Magn. Reson. 236 (11) (2013) 15–25.

[5.56] S. Stoll, A. Schweiger, EasySpin, a comprehensive software package for spectral simulation and analysis in epr, J. Magn. Reson. 178 (1) (2006) 42–55.

[5.57] I. Gromov, P. Höfer, Bruker mm-wave EPR system ELEXSYS E780: Design and performance, EUROMAR 2013, Crete, Greece, 2013.

[5.58] T. F. Segawa, A. Doll, S. Pribitzer, G. Jeschke, Copper ESEEM and HYSCORE through ultra-wideband chirp EPR spectroscopy, J. Chem. Phys. 143 (4) (2015) 044201.

6. Single-Crystal EPR on the H_{ox} stable catalytic intermediate of [FeFe]-Hydrogenase

Nature has evolved enzymes with various metallic cofactors (metallo-enzymes) to efficiently catalyze energy conversion reactions. These enzymes, which include, for example, photosystem II oxygen-evolving complex[6.1], hydrogenases[6.2], nitrogenases[6.3], and CO dehydrogenase[6.4], employ first-row transition metals to perform their catalytic functions. One of the main challenges is to fully understand these enzymatic mechanisms and provide a basis for cheap, robust, and highly active molecular catalysts designed for practical applications.[6.5] The ultimate goal is to alleviate the requirement of noble metals, such as platinum, that limit the scalability of current technology. This important biophysical and biochemical research seeks metallo-enzyme based and inspired systems as an interesting route to advance towards the future of clean energy and efficient energy storage.[6.6]

The catalytic cycle of redox enzymes often contain paramagnetic intermediates and EPR is the method of choice used to study these occurrences. Through EPR experiments, information on the magnetic and geometrical structure of the active site can be obtained. EPR spectroscopy can probe isolated intermediates in the catalytic cycle when either a single unpaired electron or multiple unpaired electrons with magnetic couplings are present in the ground state. Fundamentally understanding such enzymes is of broad biochemical and biophysical importance as scientists move towards bioengineering mimics of nature's most elusive chemistry.[6.7]

One such interesting class of metallo-enzymes are the hydrogenases[6.2] which catalyze the conversion of molecular hydrogen H_2, such that,

$$H_2 \rightleftharpoons 2H^+ + 2e^-. \tag{6.1}$$

Hydrogenases are key enzymes in many organisms for hydrogen metabolism regulation in the cell or are used as electron donors for processes further down energy conversion pathways. The hydrogenase enzyme family has three distinct active-sites with different mechanistic hydrogen conversion. These mechanisms utilize either a single-iron center [Fe], a bi-nuclear iron [FeFe], or a nickel-iron [NiFe] active site for catalysis.

For hydrogenases, specifically [NiFe]-hydrogenase, the single-crystal EPR strategy has been very successful.[6.8–11] The active site of this enzyme harbors a [NiFe] binuclear cluster in which the iron carries two cyanide (CN^-) and one carbon-monoxide (CO) ligand. The metals are bridged by two cysteine thiols and the nickel center is further coordinated by two cysteine thiolate side groups. The paramagnetic states all originate from the nickel center, while the iron center remains Fe(II) during the catalytic cycle.[6.2] The open-coordination site between the two metals can be occupied by an oxygen species leading to the inactive oxidized states or a hydride, which is the key intermediate in the catalytic cycle.[6.11] For all these species the g-tensor magnitude and orientation was determined and analyzed in terms of ligand-field theory and verified using quantum

chemical calculations providing fundamental insight into the electronic structure and the dependence on the first ligand-sphere.[6.11–14] The [NiFe]-hydrogenase crystals in these studies were relatively large ($2 \times 0.5 \times 0.5$ mm^3) enabling measurements in standard X-band probeheads with measuring time of 2-3 hours per angle, stepping over 180 degrees. However, even with the large crystal volume, ESEEM and HYSCORE experiments on [NiFe]-hydrogenase were only published in frozen solution with volumes of 50-200 μL and experimental times upwards of 2 hours for each experiment.[6.11]

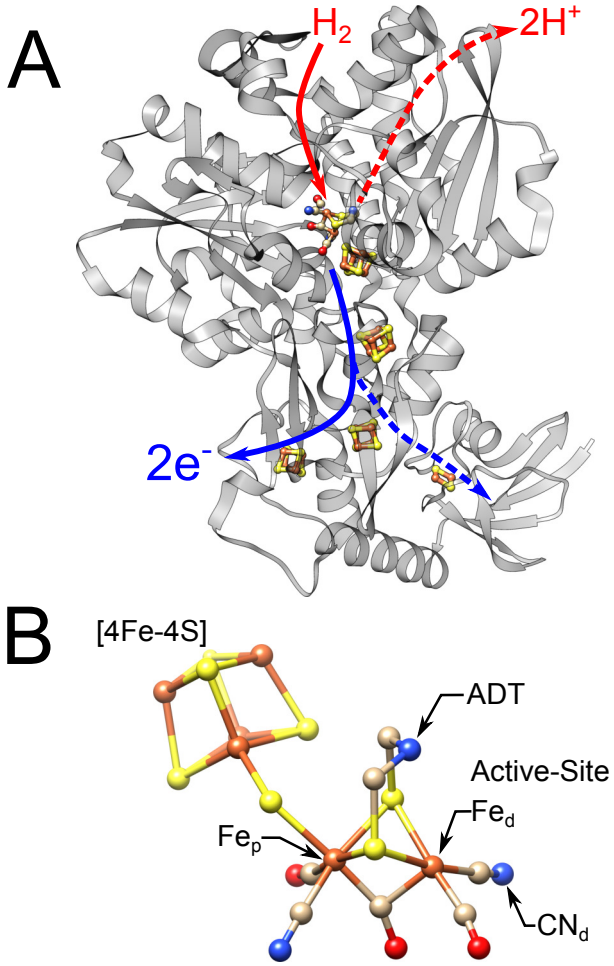

Figure 6.1.: A) Crystal structure of *Clostridium pasteurianum* (CpI) from PDB ID 4XDC.[6.15] The [Fe-Fe]-Hydrogenase CpI is a 64 kDa protein with four [4Fe-4S] clusters and one [2Fe-2S] cluster. The iron-sulfur clusters are involved in the electron-transfer pathway (solid blue). A [2Fe-2S] cluster is found symmetric to the [4Fe-4S] pathway (dashed blue) and is believed to "tune" the redox potentials of the nearby [4Fe-4S] clusters. There exists a proton ($2H^+$;dashed red) and hydrogen (H_2; solid red) transfer channel. The active-site, or the H-cluster, resides at the top in this view and is expanded to show the H-cluster structure. B) Within the H-cluster, the proximal iron (Fe_p) and distal iron (Fe_d) of the [FeFe]-hydrogenase is shown. Fe is orange, S is yellow, N is blue, O is red, and C is beige.

Of great interest is the bi-nuclear [FeFe]-hydrogenase.[6.16] These enzymes have turn-over frequencies over 10,000 s^{-1} [6.17] and provide a potential route to sustainable hydrogen

production. The proposed crystal structure of one such hydrogenase from *Clostridium pasteurianum* (CpI) highlighting the active site and electron-transfer pathway is shown in Fig. 6.1A.[6.15] The electron-transfer pathway involving accessory iron-sulfur clusters is indicated as a solid blue arrow. In CpI, a [2Fe-2S] cluster is found symmetric to the electron-transfer pathway, illustrated as a dashed blue line, and is believed to "tune" the redox potentials of the [4Fe-4S] clusters.[6.18]

The [FeFe]-hydrogenase active-site, shown in Fig. 6.1B, carries a [4Fe-4S] cluster linked via a cysteine ligand connecting the [2Fe]-cofactor molecule. The [2Fe]-cofactor contains an iron atom proximal (Fe_p) and one distal (Fe_d) to the [4Fe-4S] cluster. Each iron carries a cyanide (CN^-) and one carbon-monoxide (CO) ligand. The two irons share a bridging carbon-monoxide (μCO). Additionally, the two iron atoms are bridged by a 2-aza-propane 1,3-dithiolate (ADT) ligand. The [FeFe]-hydrogenase active site is known as the H-cluster and has a total of six iron atoms at various redox states in the catalytic cycle. In the vicinity of the H-cluster, there exists proton ($2H^+$; illustrated as a dashed red line) and molecular hydrogen (H_2; illustrated as a solid red line) channels for gas exchange. Through many spectroscopic techniques, such as Fourier Transform Infra-Red (FTIR), EPR, Nuclear Magnetic Resonance (NMR), Mößbauer, Raman, and Nuclear resonance vibrational (NRVS), a convincing catalytic cycle, shown in Fig. 6.2, has been hypothesized.[6.2, 6.19, 6.20]

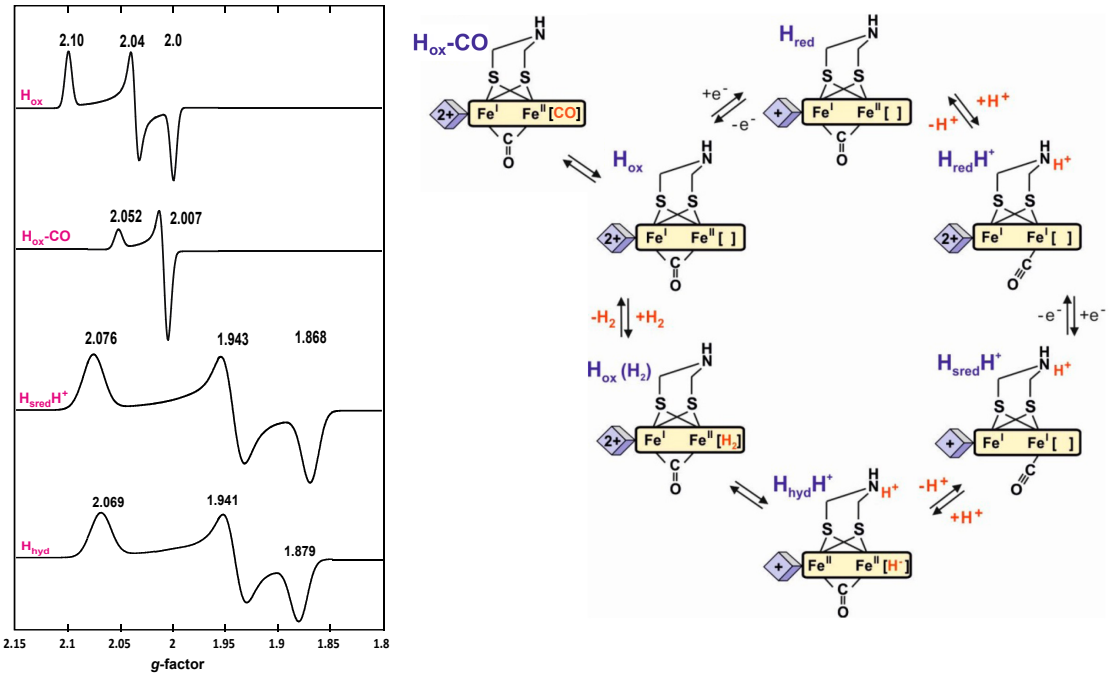

Figure 6.2.: Simulations of the EPR signal from stable paramagnetic intermediates of frozen solution samples using the indicated principle g-values along the catalytic cycle of [FeFe]-hydrogenase is displayed on the left. A simplified catalytic cycle showing the redox states of the distal and proximal iron and [4Fe-4S] clusters is displayed on the right.

From frozen solution samples the principle axes of the g-tensor have been measured using EPR spectroscopy. EasySpin simulations using the measured g-tensor values, plotted in Fig. 6.2 with g-tensor values indicated, highlight the differences of the spectra. However, the full g-tensor and the hyperfine-tensor, including angular information of the

active site are still elusive. More work must be done to fully understand the catalytic mechanism and relate it to quantum chemical calculations.

Using frozen solution samples, EPR spectroscopy has been used to study the paramagnetic states of [FeFe]-hydrogenase from several organisms.[6.2, 6.21–23] These experiments have determined the magnetic principal g-values, hyperfine, and quadrupole parameters for the catalytic states with EPR active co-factors and [4Fe-4S] clusters. Such important intermediate states include H_{ox} and H_{sred} in the catalytic cycle, a reversible carbon monoxide (CO) inhibited H_{ox}-CO state, and any state with reduced [4Fe-4S] clusters, including the *apo*-HydA protein which lacks the H-cluster. Simulations of the frozen solution spectra of these states are shown in Fig. 6.2. In this work, focus was on H_{ox} which is the primary catalytic state of the [FeFe]-hydrogenase where crystals of suitable size (0.8-3 nl) are available from CpI.

Summary of Magnetic Properties of the H_{ox} Intermediate. It was found that an *Escherichia coli* (*E. coli*) expressed *apo*-HydA could be combined with an artificially synthesized H-cluster to form fully functional [FeFe]-hydrogenase.[6.24, 6.25] This discovery has not only increased the yields of [FeFe]-hydrogenase synthesis but has allowed synthetically modified co-factors to be inserted into the *apo* protein. These experiments allowed for a wealth of information to be obtained, including the identification of the head group in the bridging ADT-ligand which eluded X-ray crystallography diffraction measurements.[6.26] Additionally, it became possible to enrich the H-cluster with magnetic isotopes and study the corresponding magnetic interactions. These experiments allowed the synthesis of ^{57}Fe in the binuclear co-factor, ^{13}C, ^{14}N, and ^{15}N in the CN^- and ADT ligands, and ^{13}C in the CO ligands. A summary of the magnetic properties of the H_{ox} stable catalytic intermediate can be found in Table 6.1.

The data in Table 6.1 represents the current knowledge on the magnetic properties of the [FeFe]-hydrogenase in the H_{ox} stable catalytic intermediate. However, this table is not exhaustive and further information on both the magnitude and orientation of the g-, hyperfine-, and quadrupole-tensors is still needed. To date, quantum chemical calculations have difficulties in predicting the principal values of the g-tensor and are only used to qualitatively assign spin densities when simulating interactions with surrounding nuclei.[6.27, 6.31] From the current literature, it is not clear which amino acids are involved in the first ligand-sphere and, therefore, single-crystal EPR experiments are needed to properly determine the full-magnetic interactions of the H-cluster.

In Chapter 5, advancement to the state-of-the-art EPR instrumentation was achieved with the self-resonant micro-helix. From this development the ability to measure protein single crystals with dimensions less than 0.3 mm^3 was feasible. In this chapter, the demonstration of (i) a full angular g-tensor determination was performed and, due to the six-fold signal enhancement of the micro-helix, that (ii) advanced pulse EPR experiments, like ESEEM and HYSCORE, were attainable on the same crystal. Herein, for the first time, the g-tensor values from field-stepped ESE rotational data and ^{14}N HYSCORE data for a [FeFe]-hydrogenase in the active oxidized state (H_{ox}) from *Clostridium pasteurianum* in a 0.3 × 0.1 × 0.1 mm^3 crystal volume were measured.[1] These data demonstrate the utility of the micro-helix in studying protein single-crystals at sizes relevant for X-ray crystallography.

[1] Only one other study is known where both measurements of the g-tensor and ESEEM/HYSCORE experiments were performed on the same crystal. The [NiFe]-hydrogenase protein single-crystals used in this study had a volume of 8 μl. Experiments were performed at both at X- and W-band. These studies can be found in Ref. [6.32].

Table 6.1.: EPR parameters determined by frozen solution of [FeFe]-hydrogenase in the H_{ox} stable catalytic intermediate through a series of pulse EPR experiments in the literature previous to this work.

	Fe_p †	Fe_d †	[4Fe4S]
oxidation state	II	I	2+
Spin state	$S = 0$	$S = 1/2$	$S_{eff} = 0$
g-values	–	[2.100, 2.040, 1.999]	–
A (MHz)	[12.3, 11.4, 12.6]	[12.3, 11.4, 12.6]	±[11.2, 10.4, 11.6]
[α, β, γ] (deg)	[0, 0, 0] ±30	[0, 0, 0] ±30	[0, 0, 0] ±30

† From DFT calculations of Ref. [6.27], it is assumed that the majority of the spin is located on Fe_d; however, significant ^{57}Fe hyperfine interactions on both irons are measured by Silakov *et al.* in Ref. [6.21].

	$C^{15}N_d$ ‡	$C^{14}N_d$ ‡	ADT-Ligand (^{14}N)§
A (MHz)	[-1.3, -1.1, 6.2]	[-0.9, -0.8, 4.4]	[1.35, 1.15, 1.15]
[α, β, γ] (deg)	[-90, -50, 0]*	[-90, -50, 0]*	[0, 0, 0]
$P_{\|\|}$ [MHz]	–	0.9	1.23
η	–	0.34	0.13
[α, β, γ] (deg)	–	[-46, -119, 0]*	[0, -90, 0]*

‡ Data is obtained from Adamska *et al.* of Ref. [6.23]. Other groups, such as Britt and colleagues in Ref. [6.28] have obtained similar values; however, Adamska *et al.* use the same molecular frame described in this work.
§ Data is obtained from Adamska *et al.* of Ref. [6.22].

	$^{13}CN_p$ ‡	$^{13}CN_d$ ‡	ADT: $^{13}C_1$ ♮	ADT: $^{13}C_2$ ♮
A (MHz)	[5.5, 5.5, 4.6]	[30, 28.5, 22.7]	[1.0, 1.3, 3.3]	[-1.49, -1.75, -0.45]
[α, β, γ] (deg)	[0, 0, 0]	[-46, -119, 0]*	–	–

	$^{13}CO_p$**	$^{13}CO_d$**	μ^{13}CO**
A (MHz)	[5.52, 5.52, 4.55]	[20.5, 29.9, 26.0]	[9.0, 3.8, 4.5]
[α, β, γ] (deg)	[25, 25, 0]	[37, 26, 0]	[0, 20, 0]

* The Euler angles are in the new EasySpin Euler definition (since version 5.0), which required the transformation $[\alpha, \beta, \gamma] = -[\gamma, \beta, \alpha]$ from the published results.
** Data is obtained from Britt *et al.* of Ref. [6.29].
♮ The principal values were found using Q-band ENDOR spectroscopy and the sign was determined by the MIMS-TRIPLE experiment in Ref. [6.30].

6.1. Methods

The [FeFe]-hydrogenase from *Clostridium pasteurianum* (CpI) was crystallized with a maximum size of 0.3 × 0.1 × 0.1 mm^3 by the method of Esselborn *et al.*[6.15] under auto-oxidative conditions, i.e. without reducing agents. This leaves the enzyme in the characteristic active oxidized state (H_{ox}), giving rise to a $S = 1/2$ ground state of the H-cluster. In the configuration, the accessory iron-sulfur clusters in the protein are oxidized and, due to anti-ferromagnetic coupling, remain EPR silent with an effective spin of zero.[6.2] Under a microscope in an anaerobic chamber, the protein crystal was drawn by capillary action into a 0.3 mm inner diameter sample tube with mother liquor and cryoprotectant, the crystal was centered in the micro-helix, and the micro-helix assembly was flash frozen. The micro-helix assembly was affixed to the EPR probehead, placed in a pre-cooled cryostat, and attached to the EPR bridge.

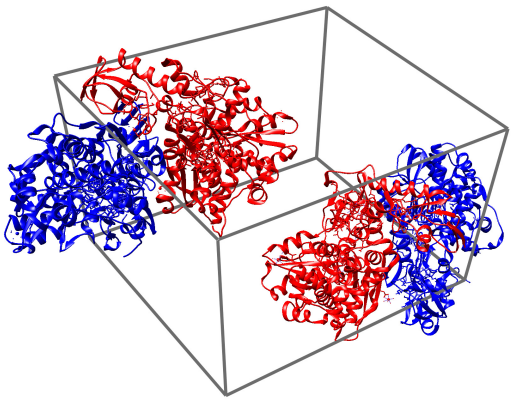

Figure 6.3.: Shown is the unit cell of PDB ID 4XDC with the molecules in an asymmetric unit (red and blue) and copied by the P1 2_1 1 symmetry.

The [FeFe]-hydrogenase of *Clostridium pasteurianum* (CpI) has a molecular weight of 64 kDa. The unit cell has P1 2_1 1 symmetry with two molecules in the asymmetric unit (PDB ID: 4XDC), shown in Fig. 6.3. Each of the four enzymes per unit cell contains one H-cluster, Fig. 6.1B, which results in four distinct signals. The single crystal had, based on the unit cell dimensions, approximately 17×10^{12} enzymes within the crystal. The signals correspond to 4.25×10^{12} spins per peak.

Matlab Routines

In the current setup, the entire probehead was rotated within the magnet with the static magnetic field in the laboratory frame L_1-direction and rotation takes place on axis of the microwave magnetic field in the L_3-direction, illustrated in Fig. 2.2. The probehead setup is axially symmetric and the whole micro-helix probehead was rotated in 5° steps over 180° in one-plane within the magnet as shown in Fig. 2.3A.

For the fitting, the laboratory frame was set in the EasySpin simulations and the collected spectra are fitted using the Matlab programs supplied in Appendix D.[2] The *esfit* routine was modified with a sub-routine employing partial parallelization of the simulations. This allowed for 12 spectra in 3 chunks to be simulated simultaneously

[2]The Matlab program files can be found at: *https://github.com/jsidabras/esFit-routines.*

for a total of 36 spectra per fit. A particle swarm optimization algorithm with 10,000 particles (fits) was used to find the solution. Each run was allowed to converge in 10 iterations and was checked if a local minimum was found. The EasySpin solution took about 1 second for each fit for a total of approximately 2.5 hours per iteration. Simulations were re-run until a good fit was established.

The EasySpin fitting simulation was set up with 9 unknowns: the three axes of the crystal frame that relates how the crystal was orientated in the laboratory frame, the three axes of the g-tensor of the first molecule (g-tensor A) and how it relates to the Molecular-Frame A, and the three axes of the g-tensor of the second molecule (g-tensor B) and how it relates to the Molecular-Frame B.

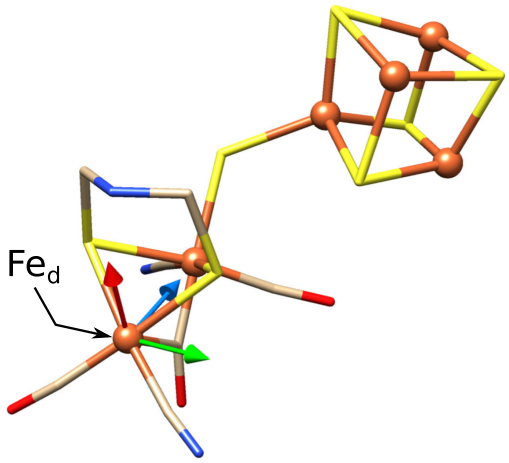

Figure 6.4.: Molecular Frame of FeFe-hydrogenase H_{ox} state from PDB ID: 4XDC. With the axes labeled as g_x: red, g_y: green, and g_z: blue. The distal iron (Fe_d) is indicated and the g-components are $g_z > g_y > g_x$.

From the crystal structure, the molecular frame of the H-cluster can be determined. The molecular frame was calculated using the distal iron (Fe_d) as the origin and is plotted in Fig. 6.4. The three axes for the molecular frame were chosen as (i) an axis from the distal iron (Fe_d) to the proximal iron (Fe_p), (ii) the normal of a plane calculated from the proximal iron, distal iron, and the nitrogen of the ADT-ligand (Fe_p-Fe_d-N_1), and (iii) the cross product of (i) into (ii). The g_z-component was chosen to be the axis from Fe_d to Fe_p and the g-components are ordered by $g_z > g_y > g_x$.

The H-cluster of the first [FeFe]-hydrogenase, colored red in Fig. 6.3, serves the basis for the first molecular-frame (Molecular-Frame A). A second molecular-frame (Molecular-Frame B) was needed since the [FeFe]-hydrogenase is crystallized with an asymmetric unit, shown blue in Fig. 6.3. Molecular-Frame B was defined by the same procedure as the Molecular-Frame A, but at the origin of the distal iron in the H-cluster of protein B.

Based on similar research at W-band with photosystem II, it can be assumed that the g-tensor of the second molecule will be similar to the first molecule.[6.33, 6.34] The deviation of the g-tensor of the second molecule (g-tensor B) with respect to the first (g-tensor A) was limited to 15 degrees. While the crystal frame and g-tensor A were set to vary a whole rotation. The principal g-values were obtained from previous frozen solution EPR experiments from Ref. [6.2] (g-values: [1.999, 2.039, 2.097] corresponding to x, y, and z, respectively).

For the HYSCORE experiment the magnetic field was set to one of the peaks measured in the two-pulse ESE experiment, τ is 280 ns, t_1 and t_2 start at 300 ns with 256 48 ns

steps, and π-pulse is 80 ns at a microwave power of 7 mW.

6.2. Results and Discussion

6.2.1. Pulse EPR in Single Crystals of [FeFe]-Hydrogenase.

First, a field-swept two-pulse electron spin-echo EPR experiment was performed every 5° on a protein single-crystal of the [FeFe]-hydrogenase of *Clostridium pasteurianum* (CpI) in the oxidized H_{ox} stable catalytic intermediate and plotted in Fig. 6.5A. A very good signal-to-noise ratio of approximately 290 was calculated for a collection time of only 8 minutes for each spectrum at a temperature of 15 K.

From these spectra, the data was fitted to simulations that relate the different frames of reference to each other as defined in the EasySpin simulation package. Rotational matrices for the relationship of these frames were tabulated in Table 6.2. The rotational matrices were calculated from the Euler angles found from the fitting of the laboratory and g-tensor frames. The peak positions of the EasySpin simulated data are plotted as an angle-dependent "resonance roadmap" which overlays on top of the field-swept two-pulse electron spin-echo EPR experiment, shown in Fig. 6.5A. Each of the four dashed lines represent the EPR signals originating from the unit cell.

Table 6.2.: Rotational matrices for the crystal frame with respect to the laboratory frame and the g-tensor with respect to the molecular frame. The crystal frame and g-tensor are found by fitting the data in Fig. 6.5A with the molecular frame from PDB ID 4XDC.

	Crystal Frame		
	a	b	c
L_1	+0.273	−0.162	−0.948
L_2	−0.022	−0.987	+0.162
L_3	−0.962	+0.023	−0.273

	Molecular-Frame A			Molecular-Frame B		
	x	y	z	x	y	z
a	−0.331	−0.938	+0.107	−0.595	−0.666	−0.450
b	−0.770	+0.203	−0.605	+0.456	−0.740	+0.494
c	+0.545	−0.283	−0.789	−0.662	+0.089	+0.744

	g-Tensor A			g-Tensor B		
	x	y	z	x	y	z
a	+0.476	−0.484	+0.735	+0.377	−0.605	−0.701
b	−0.400	+0.625	+0.671	−0.388	+0.584	−0.713
c	+0.783	+0.613	−0.103	+0.841	+0.541	−0.015

The proposed g-tensor orientation is plotted as a stereo view in Fig. 6.5B.[3] The g-tensor (g_x: green, g_y: blue, g_z: red) is presented with the origin at the distal iron (Fe_d), where DFT calculations predict the majority of the spin density in the H_{ox} stable catalytic intermediate exist.[6.27, 6.31]

[3]For a 3D view of the proposed g-tensor see: https://act-epr.org/FeFeHydrogenase.html

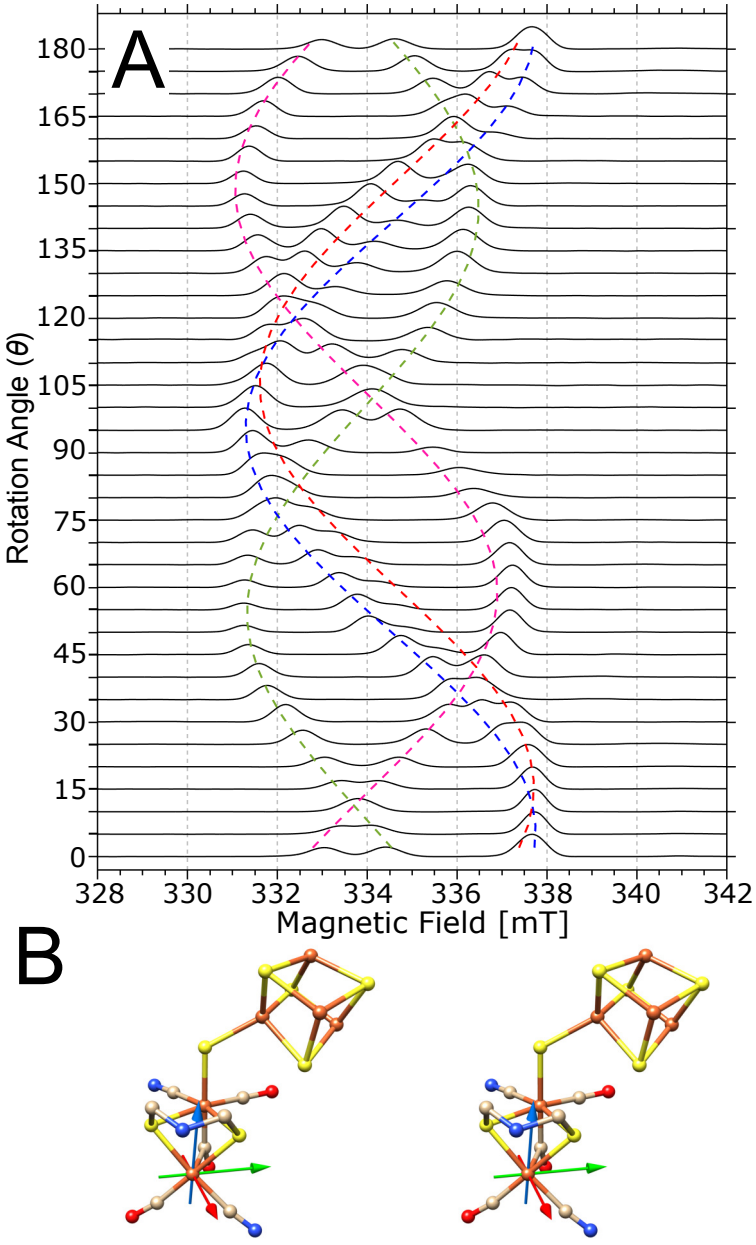

Figure 6.5.: A) Pulse EPR on single-crystal [FeFe]-hydrogenase of *Clostridium pasteurianum* (CpI) in the H_{ox} stable catalytic intermediate showing collected data in one plane for a full rotation of 180° in 5° steps at a temperature of 15 K. B) A stereo view of the analyzed g-tensor (g_x: green, g_y: blue, g_z: red) is mapped on the crystal structure (PDB ID: 4XDC). The order of the principal values of the g-tensor is $g_z \geq g_y \geq g_x$.

Comparison to Previous Literature. With ^{14}N and ^{15}N HYSCORE measurements of the CN_d^- and ADT-ligand in frozen solution, Adamska *et al.* were able to simulate and calculate a hypothetical *g*-tensor that would give rise to the measured spectra.[6.23] By proposing that the g_z-axis lies along the Fe_p-Fe_d axis, an angle of 117° is made by CN_d^--Fe_d-g_z, shown in Fig. 6.6A. This angle produced simulated HYSCORE data that matched well to the measured data. Adamska *et al.* assumed the g_x-axis pointed along the Fe_d to ADT-amine nitrogen axis bisecting the nitrogen. This assumption was made because the ADT-amine nitrogen is believed to be part of the formation of the hydride.

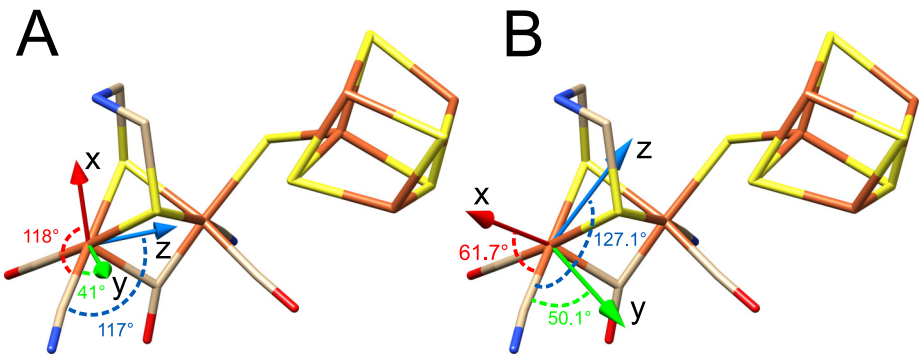

Figure 6.6.: A) The proposed *g*-tensor by Adamska *et al.* overlaid onto the H-cluster from PCB ID 3C8Y. (Adapted from Ref. [6.23] with permission from the PCCP Owner Societies.) B) The proposed *g*-tensor of this work overlaid onto the H-cluster from PCB ID 4XDC.[6.15]

The data collected using single-crystal EPR in this work is in good agreement with the HYSCORE data representing the g_z-axis collected by Adamska *et al.*. Only a deviation of 10.1° was measured from the axes previously proposed, shown in Fig. 6.6B. However, the newly proposed *g*-tensor orientation has the *x*-axis pointing outward at the open coordination site and a 9.1° deviation from bisecting the H-cluster. The *g*-tensor measured by single-crystal experiments showed that the g_z-axis lies on the plane created by the CO_d, CN_d^-, and bridging sulfur. The deviation of the frozen solution projection of Adamska *et al.* compared to the single-crystal measurement was due to the frozen solution data being under-determined.

Further analysis and refinement is possible with the collection of hyperfine and quadrupole data originating from the same crystal and relating the whole dataset to quantum chemical calculations.

6.2.2. Advanced Pulse EPR in Single Crystals.

Single-crystal ESEEM and HYSCORE experiments were performed due to the excellent signal-to-noise of the field-stepped ESE. HYSCORE was performed every 30° on each of the peaks shown in the field-swept ESE EPR dataset. Each spectrum was collected over approximately one hour, using a standard four-pulse HYSCORE sequence.[6.35] To obtain information on the hyperfine- and quadrupole-tensors, HYSCORE or ESEEM data must be collected on at least one peak and followed through a 180° rotation. Multiple peaks can be used to over-determine the system. A series of HYSCORE experiments following the fuchsia-colored resonance roadmap of Fig. 6.5A is shown in Fig. 6.7.

In an HYSCORE experiment, the 2D density representation showed correlations between the nuclear-spin transitions (m_I) in both projections of the electron spin. Both, the

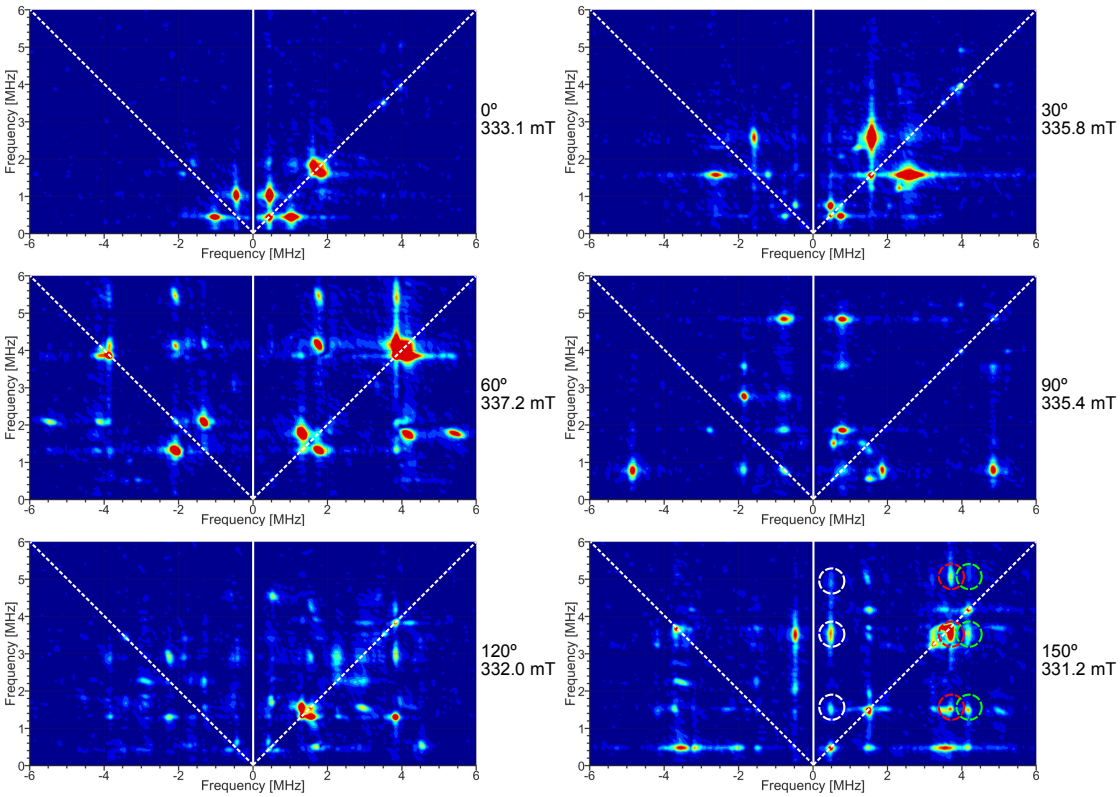

Figure 6.7.: Single-crystal HYSCORE EPR following the fuchsia-colored resonance roadmap of Fig. 6.5A.

^{14}N nucleus ($I = 1$) from a distal cyanide-ligand (CN^-_d) and the secondary amine group in the ADT-ligand can potentially contribute to the HYSCORE spectrum generating three transitions per ligand for each electron-spin transition (m_S) manifold. According to an earlier study on H_{ox} in frozen solution, the features of the distal cyanide-ligand spread out up to 6 MHz, while the transitions of the ADT-amine nitrogen were found between 2 and 4 MHz.[6.22, 6.23]

Currently, the full hyperfine- and quadrupole-tensor has not been solved. However, a comparison of the data that was collected with previous work can be used to gain further insight. For example, in Fig. 6.7 at 0 and 30 degrees a strong signal can be seen in the weak coupling (++) quadrant under a coupling frequency of 4 MHz. These signals were attributed to the ADT-ligand and fit the principal values described in Adamska *et al.*[6.22] As the HYSCORE data is rotated these signals are reduced and signals with larger couplings were found in the 4 to 6 MHz range, including signals in the strong coupling (−+) quadrant. These signals are best represented by the distal cyanide-ligand (CN^-_d) as described in a second paper by Adamska *et al.*[6.23].

6.3. Conclusions and Outlook

In this work, it was demonstrated that a full angular g-tensor determination can be performed on crystals with volumes smaller than 30 nl with excellent signal-to-noise ratio at X-band frequencies. The proposed g-tensor was a refinement on previous work by Adamska *et al.*, which used orientation-selection HYSCORE on frozen-solution samples

at X-band and Q-band to back project the g-tensor. Although in this study only a single plane was covered, the P1 2_1 1 symmetry of the crystal and the orientation of the crystal in the Laboratory Frame has allowed for a good fit.

This work also demonstrates the ability to perform HYSCORE experiments on the same crystal and highlights the feasibility of such advanced pulse EPR measurements. Future ESEEM and HYSCORE experiments will address the ^{14}N couplings of the CN^- and ADT-ligand in greater detail. Preliminary experiments can be found in Appendix E. Possibly this will involve selective ^{15}N labeling as has been demonstrated before.[6.23, 6.26] From such experiments it is possible to extract the magnitude and orientation of the nitrogen hyperfine- and quadrupole-tensors in the molecular axis frame and relate them to the electronic structure as predicted through quantum chemical calculations. Such studies will further protein engineering and artificial enzyme research for creating bio-inspired and bio-mimicking hydrogenase systems.[6.36]

This work shows the application of the synergy between X-ray crystallography diffraction data and EPR. The self-resonant micro-helix further strengthens this synergy by reducing the crystal dimensions to less than 0.3 mm and reducing the crystallograpy barrier to studying important enzymes with stable paramagnetic states.

CHAPTER 6. REFERENCES

[6.1] N. Cox, D. A. Pantazis, F. Neese, W. Lubitz, Biological water oxidation, Acc. Chem. Res. 46 (7) (2013) 1588–1596.

[6.2] W. Lubitz, H. Ogata, O. Rüdiger, E. Reijerse, Hydrogenases, Chem. Rev. 114 (8) (2014) 4081–4148.

[6.3] B. M. Hoffman, D. Lukoyanov, Z.-Y. Yang, D. R. Dean, L. C. Seefeldt, Mechanism of nitrogen fixation by nitrogenase: the next stage, Chem. Rev. 114 (8) (2014) 4041–4062.

[6.4] J. Shi, Y. Jiang, Z. Jiang, X. Wang, X. Wang, S. Zhang, P. Han, C. Yang, Enzymatic conversion of carbon dioxide, Chem. Soc. Rev. 44 (2015) 5981–6000.

[6.5] N. S. Lewis, D. G. Nocera, Powering the planet: Chemical challenges in solar energy utilization, Proc. Natl. Acad. Sci. 103 (43) (2006) 15729–15735.

[6.6] R. Schlögl, A. Aho, M. Antonietti, S. Arndt, M. Behrens, E. Bill, A. Brandner, G. Centi, P. Claus, N. Cox, et al., Chemical Energy Storage, De Gruyter, 2012.

[6.7] M. Watanabe, Y. Honda, H. Hagiwara, T. Ishihara, [FeFe]-hydrogenase and its organic molecule mimics—artificial and bioengineering application for hydrogenproduction, J. Photochem. Photobiol. C: Photochem. Rev. 33 (2017) 1–26.

[6.8] C. Geßner, O. Trofanchuk, K. Kawagoe, Y. Higuchi, N. Yasuoka, W. Lubitz, Single crystal EPR study of the Ni center of NiFe hydrogenase, Chem. Phys. Lett. 256 (4) (1996) 518–524.

[6.9] O. Trofanchuk, M. Stein, C. Geßner, F. Lendzian, Y. Higuchi, W. Lubitz, Single crystal EPR studies of the oxidized active site of [NiFe] hydrogenase from Desulfovibrio vulgaris Miyazaki F, J. Biol. Inorg. Chem. 5 (1) (2000) 36–44.

[6.10] S. Foerster, M. Stein, M. Brecht, H. Ogata, Y. Higuchi, W. Lubitz, Single crystal EPR studies of the reduced active site of [NiFe] hydrogenase from Desulfovibrio vulgaris Miyazaki F, J. Am. Chem. Soc. 125 (1) (2003) 83–93.

[6.11] W. Lubitz, E. Reijerse, M. van Gastel, [NiFe] and [FeFe] hydrogenases studied by advanced magnetic resonance techniques, Chem. Rev. 107 (10) (2007) 4331–4365.

[6.12] P. Liu, J. A. Rodriguez, Catalysts for hydrogen evolution from the [NiFe] hydrogenase to the $Ni_2P(001)$ surface: the importance of ensemble effect, J. Am. Chem. Soc. 127 (42) (2005) 14871–14878.

[6.13] A. G. Agrawal, M. van Gastel, W. Gärtner, W. Lubitz, Hydrogen bonding affects the [NiFe] active site of desulfovibrio vulgaris miyazaki F hydrogenase: a hyperfine sublevel correlation spectroscopy and density functional theory study, Phys. Chem. B 110 (15) (2006) 8142–8150.

[6.14] H. Ogata, W. Lubitz, Y. Higuchi, Structure and function of [NiFe] hydrogenases, J. Biochem. 160 (5) (2016) 251–258.

[6.15] J. Esselborn, N. Muraki, K. Klein, V. Engelbrecht, N. Metzler-Nolte, U.-P. Apfel, E. Hofmann, G. Kurisu, T. Happe, A structural view of synthetic cofactor integration into [FeFe]-hydrogenases, Chem. Sci. 7 (2016) 959–968.

[6.16] J. W. Peters, G. J. Schut, E. S. Boyd, D. W. Mulder, E. M. Shepard, J. B. Broderick, P. W. King, M. W. Adams, [FeFe]- and [NiFe]-hydrogenase diversity, mechanism, and maturation, Biochim. Biophys. Acta 1853 (6) (2015) 1350–1369.

[6.17] C. Madden, M. D. Vaughn, I. Díez-Pérez, K. A. Brown, P. W. King, D. Gust, A. L. Moore, T. A. Moore, Catalytic turnover of [FeFe]-hydrogenase based on single-molecule imaging, J. Am. Chem. Soc. 134 (3) (2012) 1577–1582.

[6.18] J. H. Artz, D. W. Mulder, M. W. Ratzloff, C. E. Lubner, O. A. Zadvornyy, A. X. LeVan, S. G. Williams, M. W. W. Adams, A. K. Jones, P. W. King, J. W. Peters, Reduction potentials of [FeFe]-hydrogenase accessory iron–sulfur clusters provide insights into the energetics of proton reduction catalysis, J. Am. Chem. Soc. 139 (28) (2017) 9544–9550.

[6.19] V. Pelmenschikov, J. A. Birrell, C. C. Pham, N. Mishra, H. Wang, C. Sommer, E. Reijerse, C. P. Richers, K. Tamasaku, Y. Yoda, T. B. Rauchfuss, W. Lubitz, S. P. Cramer, Reaction coordinate leading to H_2 production in [FeFe]-hydrogenase identified by nuclear resonance vibrational spectroscopy and density functional theory, J. Am. Chem. Soc. 139 (46) (2017) 16894–16902.

[6.20] C. Sommer, A. Adamska-Venkatesh, K. Pawlak, J. A. Birrell, O. Rüdiger, E. J. Reijerse, W. Lubitz, Proton coupled electronic rearrangement within the H-cluster as an essential step in the catalytic cycle of [FeFe] hydrogenases, J. Am. Chem. Soc. 139 (4) (2017) 1440–1443.

[6.21] A. Silakov, E. J. Reijerse, S. P. J. Albracht, E. C. Hatchikian, W. Lubitz, The electronic structure of the H-cluster in the [FeFe]-hydrogenase from Desulfovibrio desulfuricans: A Q-band ^{57}Fe- ENDOR and HYSCORE study, J. Am. Chem. Soc. 129 (37) (2007) 11447–11458.

[6.22] A. Adamska-Venkatesh, S. Roy, J. F. Siebel, T. R. Simmons, M. Fontecave, V. Artero, E. Reijerse, W. Lubitz, Spectroscopic characterization of the bridging amine in the active site of [FeFe] hydrogenase using isotopologues of the H-cluster, J. Am. Chem. Soc. 137 (40) (2015) 12744–12747.

[6.23] A. Adamska-Venkatesh, T. R. Simmons, J. F. Siebel, V. Artero, M. Fontecave, E. Reijerse, W. Lubitz, Spectroscopic characterization of the bridging amine in the active site of [FeFe] hydrogenase using isotopologues of the H- cluster, Phys. Chem. Chem. Phys. 17 (2015) 5421–5430.

[6.24] J. Esselborn, C. Lambertz, A. Adamska-Venkatesh, T. Simmons, G. Berggren, J. Noth, J. Siebel, A. Hemschemeier, V. Artero, E. Reijerse, M. Fontecave, W. Lubitz, T. Happe, Spontaneous activation of [FeFe]-hydrogenases by an inorganic [2Fe] active site mimic, Nat. Chem. Biol. 9 (2013) 607.

[6.25] J. A. Birrell, K. Wrede, K. Pawlak, P. Rodriguez-Maciá, O. Rüdiger, E. J. Reijerse, W. Lubitz, Artificial maturation of the highly active heterodimeric [FeFe] hydrogenase from Desulfovibrio desulfuricans ATCC 7757, Isr. J. Chem. 56 (9-10) (2016) 852–863.

[6.26] A. Adamska-Venkatesh, S. Roy, J. F. Siebel, T. R. Simmons, M. Fontecave, V. Artero, E. Reijerse, W. Lubitz, Spectroscopic characterization of the bridging amine in the active site of [FeFe] hydrogenase using isotopologues of the H- cluster, J. Am. Chem. Soc. 137 (40) (2015) 12744–12747.

[6.27] C. Greco, A. Silakov, M. Bruschi, U. Ryde, L. De Gioia, W. Lubitz, Magnetic properties of [FeFe]-Hydrogenases: A theoretical investigation based on extended QM and QM/MM models of the H-cluster and its surroundings, Eur. J. Inorg. Chem. 2011 (7) (2011) 1043–1049.

[6.28] W. K. Myers, T. A. Stich, D. L. M. Suess, J. M. Kuchenreuther, J. R. Swartz, R. D. Britt, The cyanide ligands of [FeFe] hydrogenase: Pulse EPR studies of ^{13}C and ^{15}N-labeled H-cluster, J. Am. Chem. Soc. 136 (35) (2014) 12237–12240.

[6.29] G. Rao, R. D. Britt, Electronic structure of two catalytic states of the [FeFe] hydrogenase H-cluster as probed by pulse electron paramagnetic resonance spectroscopy, Inorg. Chem. 57 (17) (2018) 10935–10944.

[6.30] E. J. Reijerse, V. Pelmenschikov, J. A. Birrell, C. P. Richers, M. Kaupp, T. B. Rauchfuss, S. P. Cramer, W. Lubitz, Asymmetry in the ligand coordination sphere of the [FeFe] hydrogenase active site is reflected in the magnetic spin interactions of the aza-propanedithiolate ligand, J. Phys. Chem. Lett. 10 (2019) 6794–6799.

[6.31] A. T. Fiedler, T. C. Brunold, Computational studies of the H-cluster of Fe-only hydrogenases: Geometric, electronic, and magnetic properties and their dependence on the [4Fe4S] cubane, Inorg. Chem. 44 (25) (2005) 9322–9334.

[6.32] M. T. J. Brecht, Hochfeld- und Puls-EPR-Untersuchungen an der Kofaktoren von [NiFe]-Hydrogenasen: Beiträge zur Klärung des Mechanismusses der biologischen Wasserstoffspaltung, Ph.D. thesis, Technischen Universität Berlin.

[6.33] W. Hofbauer, A. Zouni, R. Bittl, J. Kern, P. Orth, F. Lendzian, P. Fromme, H. T. Witt, W. Lubitz, Photosystem II single crystals studied by EPR spectroscopy at 94 GHz: the tyrosine radical $Y^{b}_{D}ullet$, PNAS 98 (12) (2001) 6623–6628.

[6.34] C. Teutloff, S. Pudollek, S. Keßen, M. Broser, A. Zouni, R. Bittl, Electronic structure of the Tyrosine D radical and the water-splitting complex from pulsed ENDOR spectroscopy on photosystem II single crystals, Phys. Chem. Chem. Phys. 11 (2009) 6715–6726.

[6.35] A. Schweiger, G. Jeschke, Principles of Pulse Electron Paramagnetic Resonance, Oxford University Press, 2001.

[6.36] C. Esmieu, P. Raleiras, G. Berggren, From protein engineering to artificial enzymes–biological and biomimetic approaches towards sustainable hydrogen production, Sustain. Energ. Fuels 2 (2018) 724–750.

7. Summary and Future Work

In this body of work, three challenges of modern EPR were addressed by the development of application-specific microwave resonant structures. These efforts span the frequency range from 9.5 to 420 GHz.

In Chapter 3, the introduction of the uniform field re-entrant TE_{01U} resonator at Q-band frequencies (35 GHz) improved EPR sensitivity by providing more homogeneous magnetic flux density over the sample volume during $\pi/2$ and π pulses. This has an advantage in pulse experiments as the sequences used for excitation of the spin system become more complex.

For example, HYSCORE data at Q-band will benefit from uniform magnetic flux density excitation by providing a mixing pulse that maximizes the nuclear transition mixing and reduce on-diagonal signals.[7.1, 7.2] Such signals dominate the spectrum and make interpretation difficult. For EDNMR, a uniform magnetic field excitation translates into a reduction of the width of the central peak allowing for the measurement of modulation frequencies typically hidden by this feature.[7.3] For ESEEM and pulsed electron electron double resonance (PELDOR), the modulation depth improves due to the full excitation of the spins. Finally, the increase in resonator bandwidth, from the lower Q-value and implementation of a more efficient waveguide junction, allows the spectroscopist to utilize state-of-the-art arbitrary waveform generators for further signal improvement and method development.[7.4–8]

In Chapter 4, the experiments in the THz-bandgap with hemin sample and meta-materials made from an array of split-ring resonators at 420 GHz served as an interesting example of the two oscillator problem in physics. Using analytical lumped-circuit transmission-line theory, the EPR response was fully reproduced. The use of split-ring resonators created a cross-sectional area that was not limited by the wavelength of the operating frequency. The split-ring resonators maintain an active depth proportional to the individual geometry providing a suitable volume for thin-film samples. An EPR signal enhancement of 4 was measured at the operating frequency of the split-ring resonators compared to the system without the meta-materials coupled. With the new understanding outlined in this work, it may be possible to design a series of multi-frequency high-field EPR experiments with meta-material resonant discs at each frequency. This will allow spectroscopists to probe the zero-field splitting characteristics of high-spin samples in thin-film or limited samples.

The self-resonant micro-helix at X-band (9.5 GHz) in Chapter 5 provided a resonator efficiency of 3.2 $mT/W^{1/2}$ corresponding to a $\pi/2$ pulse of 20 ns with an incident power of only 20 mW. This self-resonant micro-helix exhibited an absolute sensitivity increase up to a factor of approximately 30 in the EPR signal compared to commercial resonators. For samples that saturate readily, the micro-helix provided a factor of 6 in absolute EPR sensitivity. This translates into a factor of 36 in measurement time for equivalent sample volumes. Additionally, the high resonator efficiency and low Q_0-value (bandwidth of 90 MHz critically coupled) provides an opportunity to measure FID induced EPR on systems without costly high-power amplifiers, further extending the usefulness of pulse EPR spectroscopy.

Finally, the implementation of the self-resonant micro-helix has allowed, for the first time, the collection of EPR data from a single crystal of [FeFe]-hydrogenase in the H_{ox} state from *Clostridium pasteurianum* (CpI). The crystal dimensions were limited by by

both the duration of crystal growth time and the general crystal growth size of 0.3 × 0.1 × 0.1 mm^3. Full g-tensor analysis was successfully performed and an orientation of the principal axes was discussed. With the excellent signal-to-noise ratio, data was also collected on the same protein crystal using an ESEEM/HYSCORE pulse sequence. These data show an angle dependant ^{14}N hyperfine- and quadrupole-tensor originating from the cyanide-ligand of the distal iron and the ADT-ligand. To our knowledge, the ESEEM/HYSCORE spectra collected herein were the first published results from a protein single-crystal with a volume of 3 nL at X-band.

Future Work

In total, this collection of work advances the state-of-the-art of EPR spectroscopy. However, within these challenges, the most exciting is the application of single-crystal EPR to metallo-enzyme research.

Further advancements to the assembly described in Chapter 5 include the implementation of onboard cryogenic low-noise amplifiers. Since most metallo-enzyme EPR is performed in the 5-20 K temperature range, the use of cryogenic low-noise amplifiers is straight-forward. It was not pursued in this work since the commercial bridge would have to be modified to accommodate a transmission probehead. However, at least a factor of three increase in EPR signal-to-noise ratio compared to the work presented here is possible.[7.9]

The implementation of single-crystal EPR to metallo-enzymes allows for the study of many complex reaction centers.[7.10] Not only does this research push the boundaries of detection limits, but it also provides experimental data for quantum chemical calculations that lack accurateness for open-shell molecules. Single-crystal studies of metallo-enzymes, such as [FeFe]-hydrogenase, provide the much-needed data to study the interactions of the active site to the first and second coordination spheres.

Furthermore, other potentially interesting proteins, such as CODH[7.11], MMO[7.12], Rieske[7.13] and other Fe-S cluster containing proteins[7.14] are rarely studied in single crystals. Yet, in doing so, the electronic structure and enzymatic function of these systems could be extensively studied building on the synergy of X-ray crystallography diffraction for structural information and EPR for structural, function, and dynamic information of the local molecular interactions of an enzyme.

CHAPTER 7. REFERENCES

[7.1] S. Van Doorslaer, E. Vinck, The strength of EPR and ENDOR techniques in revealing structure–function relationships in metalloproteins, Phys. Chem. Chem. Phys. 9 (2007) 4620–4638.

[7.2] J. Harmer, G. Mitrikas, A. Schweiger, Advanced Pulse EPR Methods for the Characterization of Metalloproteins.

[7.3] N. Cox, W. Lubitz, A. Savitsky, W-band ELDOR-detected NMR (EDNMR) spectroscopy as a versatile technique for the characterisation of transition metal–ligand interactions, Mol. Phys. 111 (18–19) (2013) 2788–2808.

[7.4] A. Doll, S. Pribitzer, R. Tschaggelar, G. Jeschke, Adiabatic and fast passage ultra-wideband inversion in pulsed EPR, J. Magn. Res. 230 (2013) 27–39.

[7.5] T. F. Segawa, A. Doll, S. Pribitzer, G. Jeschke, Copper ESEEM and HYSCORE through ultra-wideband chirp EPR spectroscopy, J. Chem. Phys. 143 (4) (2015) 044201.

[7.6] P. E. Spindler, P. Schöps, W. Kallies, S. J. Glaser, T. F. Prisner, Perspectives of shaped pulses for EPR spectroscopy, J. Magn. Reson. 280 (2017) 30–45.

[7.7] N. Wili, G. Jeschke, Chirp echo fourier transform EPR-detected NMR, J. Magn. Res. 289 (2018) 26–34.

[7.8] T. F. Prisner, Shaping EPR: Phase and amplitude modulated microwave pulses, J. Magn. Res. 306 (2019) 98–101.

[7.9] R. Narkowicz, H. Ogata, E. Reijerse, D. Suter, a cryogenic receiver for EPR, J. Magn. Reson. 237 (2013) 79–84.

[7.10] R. H. Holm, E. I. Solomon, Bioinorganic Enzymology II, ACS Publications, 2014.

[7.11] J. Shi, Y. Jiang, Z. Jiang, X. Wang, X. Wang, S. Zhang, P. Han, C. Yang, Enzymatic conversion of carbon dioxide, Chem. Soc. Rev. 44 (2015) 5981–6000.

[7.12] B. M. Hoffman, D. Lukoyanov, Z.-Y. Yang, D. R. Dean, L. C. Seefeldt, Mechanism of nitrogen fixation by nitrogenase: the next stage, Chem. Rev. 114 (8) (2014) 4041–4062.

[7.13] D. J. Ferraro, L. Gakhar, S. Ramaswamy, Rieske business: Structure–function of Rieske non-heme oxygenases, Biochem. Biophys. Res. Commun. 338 (1) (2005) 175–190.

[7.14] D. C. Johnson, D. R. Dean, A. D. Smith, M. K. Johnson, Structure, function, and formation of biological iron-sulfur clusters, Annu. Rev. Biochem. 74 (1) (2005) 247–281.

Appendices

A. *Curriculum Vitae*

Jason W. Sidabras

DOB: 10 November, 1981
Websites: https://jasonsidabras.com
https://act-epr.org
Email: jason.sidabras@cec.mpg.de
jason.sidabras@gmail.com

Research

Max Planck for Chemical Energy Conversion
EU Researcher March 2016 – Present | Biophysical Chemistry | Mülheim a.d. Ruhr, DE
Supervisor: Prof. Wolfgang Lubitz
Summary: 2 Papers, 8 Talks, 3 Abstracts

- Awarded the Horizon 2020 Marie Skłodowska-Curie Actions Fellowship
- Develop resonators to study protein single-crystal applications to [FeFe]-Hydrogenase
- Developing novel resonators from 10 GHz to 244 GHz

Medical College of Wisconsin
Research Engineer III June 2003 – February 2016 | Dept. of Biophysics | Milwaukee, WI, USA
Supervisor: Prof. James S. Hyde
Summary: 31 Papers, 1 Book Chapter, 3 Patents, 7 Talks, and 35 Abstracts

- Uniform 100 kHz field modulation for cylindrical TE_{011} cavities
- Optimized PTFE extrusions resulting in EPR signal improvements
- EPR and MRI resonator development (250 MHz–260 GHz)

Education

Technical University Dortmund
Physics 2016-2020 | Dortmund, DE
Supervisor: Prof. Dieter Suter
Degree: Dr. rer. nat. (Feb. 2020)

Medical College of Wisconsin
BioPhysics 2015-2016 | Milwaukee, WI | Cum. GPA: 3.56
Supervisor: Prof. James S. Hyde

- Formal course in Magnetic Resonance in context with new developments of spin-labeling
- Formal course in biophysical principles of cellular functions

Marquette University
M.S. in Electrical Engineering 2004-2010 | Milwaukee, WI | Cum. GPA: 3.31
Supervisors: Profs. James E. Richie & James S. Hyde
Thesis: Modelling Electron Paramagnetic Resonance Field-Modulation Slots using Dyadic Green Functions of Evanescent Fields in Rectangular and Cylindrical Waveguides

- Studied fundamentals of numerical methods
- Further refined analytical skills in electromagnetic theory

Milwaukee School of Engineering
B.S. in Electrical Engineering Technology 1999-2003 | Milwaukee, WI

- Studied fundamentals of electrical engineering principles: focused on electromagnetics

Additional Course Work

- Physical Methods in Molecular and Heterogeneous Catalysis, Summerschool, 2016, Wissenschaftspark Gelsenkirchen.
- 7th EFEPR summer school: Advanced Electron Paramagnetic Resonance (EPR) Spectroscopy, 2015, Berlin.

Awards

2017-2019	Horizon 2020 Marie Skłodowska-Curie Actions Fellowship
2017	21st annual JEOL Student Lecture Competition Winner
2017	EPR2017 Young Investigator Award of Excellence Prize

Societies

2009	U.S. National	Sigma Xi: Scientific research
2012	International	International EPR (ESR) Society
2015	International	Advancing Science, Serving Society (AAAS)

Patents

2006	U.S. #7,088,101	Aqueous sample holder for electron paramagnetic resonance and magnetic resonance spectroscopy.
2014	U.S. #8,674,694	Coil System and Method for Post-Exposure Dosimetry Using Electron Paramagnetic Resonance Spectroscopy.
2017	PCT.US2017-052045	Strongly coupled fourth-order resonance coil systems for enhanced signal detection

In the Media

1. Oct. 2019: Royal Chemical Society Chemistry World
   https://www.chemistryworld.com/news/new-setup-enables-epr-studies-on-tiny-protein-crystals/4010466.article
2. Nov. 2019: Phys.org
   https://phys.org/news/2019-11-electron-paramagnetic-resonance-epr-spectroscopy.html

List of Publications

1. Sidabras, J. W., Duan, J., Winkler, M., Happe, T., Hussein, R., Zouni, A., Suter, D., Schnegg, A., Lubitz, W. and Reijerse, E. J. *Extending electron paramagnetic resonance to nanoliter volume protein single crystals using a self-resonant microhelix.,* Sci. Adv. (5), 2019, pp. eaay1394.
2. Hyde, J. S., Sidabras, J. W. and Mett, R. R. *Uniform Field Resonators for EPR Spectroscopy: A Review.,* Cell Biochem. Biophys. (77), 2019, pp. 3–14.
3. Mett, R. R., Sidabras, J. W., Anderson, J. R., Klug, C. S. and Hyde, J. S. *Rutile dielectric loop-gap resonator for X-band EPR spectroscopy of small aqueous samples.,* J. Magn. Reson. (307), 2019, pp. 106585.
4. Zadlo, A., Szewczyk, G., Sarna, M., Camenisch, T. G., Sidabras, J. W., Ito, S., Wakamatsu, K., Sagan, F., Mitoraj, M. and Sarna, T. *Photobleaching of pheo-melanin increases its phototoxic potential: Physicochemical studies of synthetic pheomelanin subjected to aerobic photolysis.,* Pigment Cell Melanoma Res. (32), 2019, pp. 359–372.
5. Swarts, S. G., Sidabras, J. W., Grinberg, O., Tipikin, D. S., Kmiec, M., Petryakov, S. V., Schreiber, W., Wood, V. A., Williams, B. B., Flood, A. B. and Swartz, H. M. *Developments in Biodosimetry Methods for Triage With a Focus on X-band Electron Paramagnetic Resonance In Vivo Fingernail Dosimetry.,* Health Phys. (115), 2018, pp. 140–150.

6. Sidabras, J. W., Mett, R. R. and Hyde, J. S. *Extruded dielectric sample tubes of complex cross section for EPR signal enhancement of aqueous samples.,* J. Magn. Reson. (277), 2017, pp. 45–51.
7. Sidabras, J. W., Reijerse, E. J. and Lubitz, W. *Uniform Field Re-entrant Cylindrical TE_{01U} Cavity for Pulse Electron Paramagnetic Resonance Spectroscopy at Q-band.,* Appl. Magn. Reson. (48), 2017, pp. 1301–1314.
8. Sidabras, J. W., Richie, J. E. and Hyde, J. S. *Axially uniform magnetic field-modulation excitation for electron paramagnetic resonance in rectangular and cylindrical cavities by slot cutting.,* J. Magn. Reson (274), 2017, pp. 115–124.
9. Sidabras, J. W., Sarna, T., Mett, R. R. and Hyde, J. S. *Uniform field loop-gap resonator and rectangular TE_{U02} for aqueous sample EPR at 94GHz.,* J. Magn. Reson (282), 2017, pp. 129–135.
10. Strangeway, R. A., Hyde, J. S., Camenisch, T. G., Sidabras, J. W., Mett, R. R., Anderson, J. R., Ratke, J. J. and Subczynski, W. K. *Broadband W-band Rapid Frequency Sweep Considerations for Fourier Transform EPR.,* Cell Biochem. Biophys. (75), 2017, pp. 259–273.
11. Grinberg, O., Sidabras, J. W., Tipikin, D. S., Krymov, V., Mariani, M., Feldman, M. M., Kmiec, M. M., Petryakov, S. V., Brugger, S., Carr, B., Schreiber, W., Swarts, S. G. and Swartz, H. M. *Dielectric-Backed Aperture Resonators for X-Band in vivo EPR Nail Dosimetry.,* Radiat. Prot. Dosim. (172), 2016, pp. 121–126.
12. Mett, R. R., Sidabras, J. W. and Hyde, J. S. *MRI surface-coil pair with strong inductive coupling.,* Rev. Sci. Instrum. (87), 2016, pp. 124704.
13. Mett, R. R., Sidabras, J. W. and Hyde, J. S. *Meta-metallic coils and resonators: Methods for high Q-value resonant geometries.,* Rev. Sci. Instrum. (87), 2016, pp. 084703.
14. Sidabras, J. W., Strangeway, R. A., Mett, R. R., Anderson, J. R., Mainali, L. and Hyde, J. S. *Hyperbolic-cosine waveguide tapers and oversize rectangular waveguide for reduced broadband insertion loss in W-band electron paramagnetic resonance spectroscopy. II. Broadband characterization.,* Rev. Sci. Instrum. (87), 2016, pp. 034704.
15. Tipikin, D. S., Swarts, S. G., Sidabras, J. W., Trompier, F. and Swartz, H. M. *Possible nature of the radiation-induced signal in nails: High-field EPR, confirming chemical synthesis, and quantum chemical calculations.,* Radiat. Prot. Dosim. (172), 2016, pp. 112–120.
16. Li, R., Liu, X., Sidabras, J. W., Paulson, E. S., Jesmanowicz, A., Nencka, A. S., Hudetz, A. G. and Hyde, J. S. *Restoring susceptibility induced MRI signal loss in rat brain at 9.4 T: A step towards whole brain functional connectivity imaging.,* PLoS One (10), 2015, pp. e0119450.
17. He, X., Swarts, S. G., Demidenko, E., Flood, A. B., Grinberg, O., Gui, J., Mariani, M., Marsh, S. D., Ruuge, A. E., Sidabras, J. W., Tipikin, D., Wilcox, D. E. and Swartz, H. M. *Development and validation of an ex vivo electron paramagnetic resonance fingernail biodosimetric method.,* Radiat. Prot. Dosim. (159), 2014, pp. 172–181.
18. Mainali, L., Sidabras, J. W., Camenisch, T. G., Ratke, J. J., Raguz, M., Hyde, J. S. and Subczynski, W. K. *Spin-label W-band EPR with seven-loop-six-gap resonator: Application to lens membranes derived from eyes of a single donor.,* Appl. Magn. Reson. (45), 2014, pp. 1343–1358.
19. Sidabras, J. W., Varanasi, S. K., Mett, R. R., Swarts, S. G., Swartz, H. M. and Hyde, J. S. *A microwave resonator for limiting depth sensitivity for electron paramagnetic resonance spectroscopy of surfaces.,* Rev. Sci. Instrum. (85), 2014, pp. 104707.
20. Hyde, J. S., Bennett, B., Kittell, A. W., Kowalski, J. M. and Sidabras, J. W. *Moving difference (MDIFF) non-adiabatic rapid sweep (NARS) EPR of copper(II).,* J. Magn. Reson (236), 2013, pp. 15–25.
21. Swartz, H. M., Flood, A. B., Williams, B. B., Dong, R., Swarts, S. G., He, X., Grinberg, O., Sidabras, J. W., Demidenko, E., Gui, J., Gladstone, D. J., Jarvis, L. A., Kmiec, M.

M., Kobayashi, K., Lesniewski, P. N., Marsh, S. D. P., Matthews, T. P., Nicolalde, R. J., Pennington, P. M., Raynolds, T., Salikhov, I., Wilcox, D. E. and Zaki, B. I. *Electron paramagnetic resonance dosimetry for a large-scale radiation incident.,* Health Phys. (103), 2012, pp. 255–267.

22. He, X., Gui, J., Matthews, T. P., Williams, B. B., Swarts, S. G., Grinberg, O., Sidabras, J., Wilcox, D. E. and Swartz, H. M. *Advances towards using finger/toenail dosimetry to triage a large population after potential exposure to ionizing radiation.,* Radiat. Meas. (46), 2011, pp. 882–887.
23. Kittell, A. W., Camenisch, T. G., Ratke, J. J., Sidabras, J. W. and Hyde, J. S. *Detection of undistorted continuous wave (CW) electron paramagnetic resonance (EPR) spectra with non-adiabatic rapid sweep (NARS) of the magnetic field.,* J. Magn. Reson (211), 2011, pp. 228–233.
24. Mett, R. R., Sidabras, J. W., Anderson, J. R. and Hyde, J. S. *Hyperbolic-cosine waveguide tapers and oversize rectangular waveguide for reduced broadband insertion loss in W-band electron paramagnetic resonance spectroscopy.,* Rev. Sci. Instrum. (82), 2011, pp. 074704.
25. Pollock, J., Williams, B. B., Sidabras, J. W., Grinberg, O., Salikhov, I., Lesniewski, P., Kmiec, M. and Swartz, H. M. *Surface loop resonator design for in vivo EPR tooth dosimetry using finite element analysis.,* Health Phys. (98), 2010, pp. 339–344.
26. Hyde, J. S., Bennett, B., Walter, E. D., Millhauser, G. L., Sidabras, J. W. and Antholine, W. E. *EPR of Cu^{2+} prion protein constructs at 2 GHz using the $g_\perp$ region to characterize nitrogen ligation.,* Biophys. J. (96), 2009, pp. 3354–3362.
27. Mett, R. R., Sidabras, J. W. and Hyde, J. S. *Coupling of Waveguide and Resonator by Inductive and Capacitive Irises for EPR Spectroscopy.,* Appl. Magn. Reson. (35), 2009, pp. 285–318.
28. Froncisz, W., Camenisch, T. G., Ratke, J. J., Anderson, J. R., Subczynski, W. K., Strangeway, R. A., Sidabras, J. W. and Hyde, J. S. *Saturation recovery EPR and ELDOR at W-band for spin labels.,* J. Magn. Reson (193), 2008, pp. 297–304.
29. Mett, R. R., Sidabras, J. W., Golovina, I. S. and Hyde, J. S. *Dielectric microwave resonators in TE_{011} cavities for electron paramagnetic resonance spectroscopy.,* Rev. Sci. Instrum. (79), 2008, pp. 094702.
30. Hyde, J. S., Froncisz, W., Sidabras, J. W., Camenisch, T. G., Anderson, J. R. and Strangeway, R. A. *Microwave frequency modulation in CW EPR at W-band using a loop-gap resonator.,* J. Magn. Reson (185), 2007, pp. 259–263.
31. Sidabras, J. W., Mett, R. R., Froncisz, W., Camenisch, T. G., Anderson, J. R. and Hyde, J. S. *Multipurpose EPR loop-gap resonator and cylindrical TE_{011} cavity for aqueous samples at 94 GHz.,* Rev. Sci. Instrum. (78), 2007, pp. 034701.
32. Sidabras, J. W., Mett, R. R. and Hyde, J. S. *Aqueous flat-cells perpendicular to the electric field for use in electron paramagnetic resonance spectroscopy, II: design.,* J. Magn. Reson (172), 2005, pp. 333–341.
33. Mett, R. R., Sidabras, J. W. and Hyde, J. S. *Radio frequency skin depth concepts in magnetic resonance,* Curr. Top. Biophys (28:2), 2004, pp. 117–122.

Book Chapter

1. Hyde, J. S. Sidabras, J. W., Mett, R. R., *Multifrequency electron paramagnetic resonance: theory and applications*, edited by S. K. Misra (John Wiley & Sons, 2011), Chap. 5.2: Resonators for Multifrequency EPR of Spin Labels.

List of Recent Presentations

Full list of abstracts can be found at *http://jasonsidabras.com.* Internal talks at MPI-CEC, TUD, or MCW are not listed.

1. J. W. Sidabras (2019). *Beyond structure: Investigating paramagnetic states in protein crystals of nano-liter volumes at X band.* XIth International Workshop on EPR (ESR) in Biology and Medicine, Krakow, Poland (Invited Talk)
2. J. W. Sidabras, E. J. Reijerse, W. Lubitz (2018). *Uniform Field Resonators for Correlation Spectroscopy Methods at Q-Band.* 51st Annual International Meeting ESR Spectroscopy Group of the Royal Society of Chemistry, London, UK (Talk)
3. J. W. Sidabras, D. Suter, E. J. Reijerse, A. Savitsky, W. Lubitz (2017). *Planar Micro-Resonators and Micro-Helix Geometries for Studying Protein Single Crystals with X-band EPR.* 50th International International Meeting of the ESR Spectroscopy Group of the Royal Society of Chemistry, Oxford, UK (Talk)
4. J. W. Sidabras, D. Suter, E. J. Reijerse, W. Lubitz (2017). *Multi-Frequency Resonator Development.* International Conference on Electron Paramagnetic Resonance Spectroscopy and Imaging of Biological Systems EPR 2017, Morgantown, WV (Talk)
5. J. W. Sidabras, D. Suter, E. J. Reijerse, A. Savitsky, W. Lubitz (2017). *Resonator Development for Studying Protein Single Crystals of Limited Dimensions at X-band.* 20th ISMAR and Rocky Mountain Conference on EPR, Quebec City, Quebec, Canada (Talk)
6. J. W. Sidabras, D. Suter, E. J. Reijerse, W. Lubitz (2017). *Multi-Frequency Resonator Development for Studying Volume-Limited Metallo-Proteins.* 2nd Adriatic Symposium on Byophysical Approaches in Biomedical Studies, Split, Croatia (Invited Talk)
7. J. W. Sidabras, D. Suter, E. J. Reijerse, W. Lubitz (2016). *Micro-Resonators for Electron Paramagnetic Resonance Spectroscopy of Size Limited Samples at 9.5 GHz.* German Chemical Society (GDCh), Magnetic Resonance Section (FGMR) 38th Annual Discussion Meeting, Düsseldorf, DE (Talk)
8. J. W. Sidabras, D. Suter, E. J. Reijerse, W. Lubitz (2016). *Resonator Development for Studying Protein Single Crystals of Limited Dimensions.* Xth International Workshop on EPR (ESR) in Biology and Medicine, Krakow, Poland (Invited Talk)

List of Recent Poster Presentations

Full list of abstracts can be found at *http://jasonsidabras.com.* Internal posters at MPI-CEC or MCW are not listed.

1. J. W. Sidabras, E. J. Reijerse, C. Sommer, J. Duan, M. Winkler, T. Happe, D. Suter, W. Lubitz (2019) *Technical Advances in Order to Study nano-Liter Volume [FeFe]-Hydrogenase Single Crystals using Electron Paramagnetic Resonance*, 12th International Hydrogenase Conference, Lisbon, Portugal (Poster)
2. J. W. Sidabras, E. J. Reijerse, J. Duan, M. Winkler, T. Happe, A. Schnegg, D. Suter, W. Lubitz (2019) *A Self-Resonant Micro-Helix for Studying nano-Liter Volume [FeFe]-Hydrogenase Single-Crystals using CW and Pulse EPR Techniques*, EUROMAR 2019, ISMAR 2019, and the 41st GDCh FGMR Joint Conference, Berlin, Germany (Poster)
3. J. W. Sidabras, E. J. Reijerse, J. Duan, M. Winkler, T. Happe, A. Schnegg, D. Suter, W. Lubitz (2019) *CW and Pulse EPR Studies of nano-Liter Volume [FeFe]-Hydrogenase Single Crystals Using a Novel Self-Resonant micro-Helix*, EFEPR 2019, Bratislava, Slovakia (Poster)
4. J. W. Sidabras, C. Sommer (2019) *An Order of Magnitude Signal-to-Noise Improvement Using the Segmented-Overlap Fourier-Filtering and Averaging (SOFFA) Approach*, XIth International Workshop on EPR (ESR) in Biology and Medicine, Krakow, Poland (Poster)

B. Finite-element Modeling Signal Calculations

Signal Calculations for Ansys HFSS Assuming an Aqueous Sample

The following lines of code can be placed in a file called "CalculateSignal-Water.cls" and placed in the *PersonalLibs* folder from the Ansys installation. This folder location can be found in Tools▶Options▶General▶Directories. The *cls* file should be loaded in the ***Fields Calculator*** twice, in order to load all expressions.[1]

All codes and Ansys HFSS files can be found at https://github.com/jsidabras/HFSSTutorial/.

Constants

The following constants are defined.

- **ImDieHold**: The imaginary dielectric constant (ϵ'') of the dielectric that holds the resonator. In the case of the PMR, this is the sapphire. In the case of the micro-Helix, this is the PTFE.
- **ImDieSam**: The imaginary dielectric constant (ϵ'') of the sample. In the case of water, the dielectric constant at X-band (9.5 GHz) is $\epsilon_r = 63 - i26.46$. In the case of ICE, the dielectric constant at X-band is $\epsilon_r = 3.2 - i0.00128$
- **Frq**: The real part of the solved frequency.

```
$begin 'Named_Expression'
  Name('ImDieHold')
  Expression('0.0001')
  Scalar_Constant(0.0001)
$end 'Named_Expression'
$begin 'Named_Expression'
  Name('ImDieSam')
  Expression('26.46')
  Scalar_Constant(26.46)
$end 'Named_Expression'
$begin 'Named_Expression'
  Name('Frq')
  Expression('Real(Freq)')
  Output_Variable('Freq', 4)
  Operation('Real')
$end 'Named_Expression'
```

[1] This seems to be a dependency bug.

Power losses

The following power losses are defined

- **Pls**: Losses associated with the sample. Uses *ImDieSam* as ϵ''.
- **Plw**: Requires the user to select all faces of objects that are metal and create *FaceList1* (Modeler→List→Create→Face List).
- **Ple**: Losses associated with the dielectric holder. Uses *ImDieHold* as ϵ''.

```
$begin 'Named_Expression'
  Name('Pls')
  Expression('*(Integrate(Volume(Sample), Real(Dot(<Ex,Ey,Ez>, Conj(<
      Ex,Ey,Ez>)))), *(8.85419E-012, *(3.14159, *(ImDieSam, Frq))))')
  Fundamental_Quantity('E')
  Fundamental_Quantity('E')
  Operation('Conj')
  Operation('Dot')
  Operation('Real')
  EnterVolume('Sample')
  Operation('VolumeValue')
  Operation('Integrate')
  Scalar_Constant(8.85419e-012)
  Scalar_Constant(3.14159)
  NameOfExpression('ImDieSam')
  NameOfExpression('Frq')
  Operation('*')
  Operation('*')
  Operation('*')
  Operation('*')
$end 'Named_Expression'
$begin 'Named_Expression'
  Name('Plw')
  Expression('*(Integrate(Surface(Facelist1), Real(Dot(<Hx,Hy,Hz>,
      Conj(<Hx,Hy,Hz>)))), 1/(*(*(1/(Sqrt(*(*(76.6549, Frq), 3.14159))
      ), 61000000), 2)))')
  NameOfExpression('<Hx,Hy,Hz>')
  NameOfExpression('<Hx,Hy,Hz>')
  Operation('Conj')
  Operation('Dot')
  Operation('Real')
  EnterSurface('Facelist1')
  Operation('SurfaceValue')
  Operation('Integrate')
  Scalar_Constant(76.6549)
  NameOfExpression('Frq')
  Operation('*')
  Scalar_Constant(3.14159)
  Operation('*')
  Operation('Sqrt')
  Operation('1/')
  Scalar_Constant(6.1e+007)
  Operation('*')
  Scalar_Constant(2)
  Operation('*')
  Operation('1/')
  Operation('*')
```

```
45 $end 'Named_Expression'
46 $begin 'Named_Expression'
47   Name('Ple')
48   Expression('*(Integrate(Volume(pol_2), Real(Dot(<Ex,Ey,Ez>, Conj(<
         Ex,Ey,Ez>)))), *(8.85419E-012, *(3.14159, *(ImDieHold, Frq))))')
49   Fundamental_Quantity('E')
50   Fundamental_Quantity('E')
51   Operation('Conj')
52   Operation('Dot')
53   Operation('Real')
54   EnterVolume('pol_2')
55   Operation('VolumeValue')
56   Operation('Integrate')
57   Scalar_Constant(8.85419e-012)
58   Scalar_Constant(3.14159)
59   NameOfExpression('ImDieHold')
60   NameOfExpression('Frq')
61   Operation('*')
62   Operation('*')
63   Operation('*')
64   Operation('*')
65 $end 'Named_Expression'
```

Magnetic Fields

```
$begin 'Named_Expression'
  Name('H1r')
  Expression('*(Sqrt(Real(*(Conj(Dot(<Hx,Hy,Hz>, <(0, 0), (1, 0), (0,
      1)>)), Dot(<Hx,Hy,Hz>, <(0, 0), (1, 0), (0, 1)>)))), 0.5)')
  NameOfExpression('<Hx,Hy,Hz>')
  ComplexVector_Constant(0, 0, 1, 0, 0, 1)
  Operation('Dot')
  Operation('Conj')
  NameOfExpression('<Hx,Hy,Hz>')
  ComplexVector_Constant(0, 0, 1, 0, 0, 1)
  Operation('Dot')
  Operation('*')
  Operation('Real')
  Operation('Sqrt')
  Scalar_Constant(0.5)
  Operation('*')
$end 'Named_Expression'
$begin 'Named_Expression'
  Name('H1rMax')
  Expression('Maximum(Volume(Sample), H1r)')
  NameOfExpression('H1r')
  EnterVolume('Sample')
  Operation('VolumeValue')
  Operation('Maximum')
$end 'Named_Expression'
$begin 'Named_Expression'
  Name('IntH1r2dVs')
  Expression('*(Integrate(Volume(Sample), Real(*(Conj(Dot(<Hx,Hy,Hz>,
      <(0, 0), (1, 0), (0, 1)>)), Dot(<Hx,Hy,Hz>, <(0, 0), (1, 0),
     (0, 1)>)))), 0.25)')
  NameOfExpression('<Hx,Hy,Hz>')
  ComplexVector_Constant(0, 0, 1, 0, 0, 1)
  Operation('Dot')
  Operation('Conj')
  NameOfExpression('<Hx,Hy,Hz>')
  ComplexVector_Constant(0, 0, 1, 0, 0, 1)
  Operation('Dot')
  Operation('*')
  Operation('Real')
  EnterVolume('Sample')
  Operation('VolumeValue')
  Operation('Integrate')
  Scalar_Constant(0.25)
  Operation('*')
$end 'Named_Expression'
```

Signal

```
$begin 'Named_Expression'
  Name('Ss')
  Expression('*(*(*(3.14159, *(2, Frq)), IntH1r2dVs), 1/(*(*(H1rMax,
      10000), Sqrt(+(Ple, +(Pls, Plw))))))')
  Scalar_Constant(3.14159)
  Scalar_Constant(2)
  NameOfExpression('Frq')
  Operation('*')
  Operation('*')
  NameOfExpression('IntH1r2dVs')
  Operation('*')
  NameOfExpression('H1rMax')
  Scalar_Constant(10000)
  Operation('*')
  NameOfExpression('Ple')
  NameOfExpression('Pls')
  NameOfExpression('Plw')
  Operation('+')
  Operation('+')
  Operation('Sqrt')
  Operation('*')
  Operation('1/')
  Operation('*')
$end 'Named_Expression'
$begin 'Named_Expression'
  Name('Su')
  Expression('*(*(IntH1r2dVs, *(*(1.25664E-006, Frq), 6.28319)),
      1/(+(Ple, +(Pls, Plw))))')
  NameOfExpression('IntH1r2dVs')
  Scalar_Constant(1.25664e-006)
  NameOfExpression('Frq')
  Operation('*')
  Scalar_Constant(6.28319)
  Operation('*')
  Operation('*')
  NameOfExpression('Ple')
  NameOfExpression('Pls')
  NameOfExpression('Plw')
  Operation('+')
  Operation('+')
  Operation('1/')
  Operation('*')
$end 'Named_Expression'
```

Resonator Efficiency

```
$begin 'Named_Expression'
  Name('LambdaMax')
  Expression('*(*(H1rMax, 0.0125663706143592), 1/(Sqrt(+(Pls, +(Plw, Ple))))))')
  NameOfExpression('H1rMax')
  Scalar_Constant(0.0125664)
  Operation('*')
  NameOfExpression('Pls')
  NameOfExpression('Plw')
  NameOfExpression('Ple')
  Operation('+')
  Operation('+')
  Operation('Sqrt')
  Operation('1/')
  Operation('*')
$end 'Named_Expression'
$begin 'Named_Expression'
  Name('LambdaAve')
  Expression('*(*(*(Integrate(Volume(Sample), H1r), 0.0125663706143592), 1/(Integrate(Volume(Sample), 1))), 1/(Sqrt(+(Pls, +(Plw, Ple))))))')
  NameOfExpression('H1r')
  EnterVolume('Sample')
  Operation('VolumeValue')
  Operation('Integrate')
  Scalar_Constant(0.0125664)
  Operation('*')
  Scalar_Constant(1)
  EnterVolume('Sample')
  Operation('VolumeValue')
  Operation('Integrate')
  Operation('1/')
  Operation('*')
  NameOfExpression('Pls')
  NameOfExpression('Plw')
  NameOfExpression('Ple')
  Operation('+')
  Operation('+')
  Operation('Sqrt')
  Operation('1/')
  Operation('*')
$end 'Named_Expression'
```

C. Mathematica Code

The following Appendix contains the Wolfram Mathematica notebook file used to generate the data in Chapter 4. This code has been inserted into this document. All code is available at https://github.com/jsidabras/THzCode.

Definitions

The following calculations and processes are performed:

1. Solve the linear equation for the current and voltage relationships.
   - **EqnMatrix**: This matrix is the mesh current relationship defined by the circuit
   - **VVector**: This vector is the voltage relationship defined by the circuit
   - **LinearSolve** and **FullSimplify**: Solve the linear equation $m \cdot X = b$ and plug it into the relationship for $\mathbf{Z_{21}}$ "Open-circuit forward transimpedance"
   - $\mathbf{Z_{21}a}$: Define the "Open-circuit forward transimpedance" as a function with inputs of the transmission line (inductance LL, capacitance CL), resonator (inductance LR, capacitance CR, resistance RR), and coupling coefficients (mutual capacitance kc and mutual inductance kL) at the frequency of Ω.
2. Define the characteristics of the transmission-line circuit, resonator, and "signal".
3. Solve $\mathbf{Z_{21}a}$ over the frequency range of 255 to 700 GHz (8.51 to 23.35 cm^{-1}) and step the resonance shift between 2.0 to 1.0, which corresponds to resonance frequency shift to mimic the shift in static magnetic field.
   - **Coupled Only**: Set the resonance of the bulk transmission-line to zero (gL) and solve for $\mathbf{Z_{21}a}$ if only the resonator is coupled to the spins.
   - **With Transmission**: Solve for $\mathbf{Z_{21}a}$ if with both the transmission-line and the resonator coupled to the spins.
   - **Only Transmission**: Solve for $\mathbf{Z_{21}a}$ if with the transmission-line coupled to the spins and the resonator coupling set to zero (mutual capacitance kkc).
4. Solve and plot the frequency splittings generated for strong (100 time larger gR) and weak coupling regimes.

Lossless T-Line Extension Model

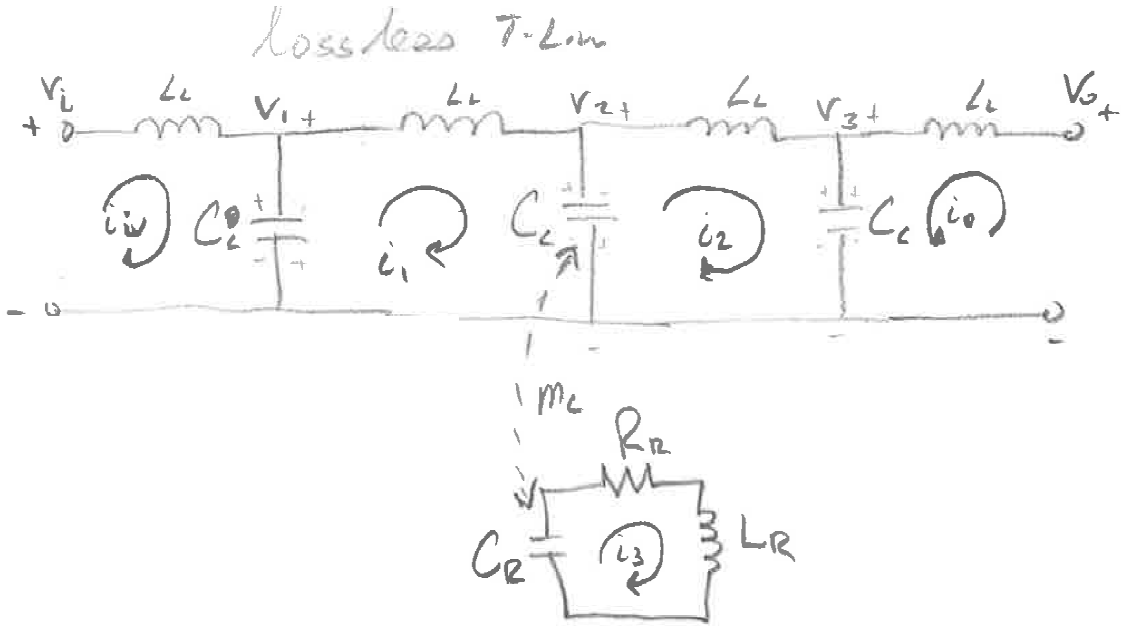

At port 1		At port 2	
Open-circuit input impedance	$z_{11} = \frac{V_1}{I_1}\Big\|_{I_2=0}$	Open-circuit forward transimpedance	$z_{21} = \frac{V_2}{I_1}\Big\|_{I_2=0}$
Open-circuit reverse transimpedance	$z_{12} = \frac{V_1}{I_2}\Big\|_{I_1=0}$	Open-circuit output impedance	$z_{22} = \frac{V_2}{I_2}\Big\|_{I_1=0}$

```
EqnMatrix = {{(i ω LL/2 + 1/(i ω CL)), -1/(i ω CL), 0, 0, 0},
  {-1/(i ω CL), (2/(i ω CL) + i ω LL), -1/(i ω CL), 0, i ω Mc},
  {0, -1/(i ω CL), (2/(i ω CL) + i ω LL), 1/(i ω CL), i ω Mc - i ω ML},
  {0, 0, 1/(i ω CL), (i ω LL/2 + 1/(i ω CL)), 0},
  {0, i ω Mc, -(i ω Mc - i ω ML), 0, (RR + i ω LR + 1/(i ω CR))}};
VVector = {vi, 0, 0, vo, 0};
Ans = FullSimplify[
   LinearSolve[EqnMatrix, VVector] /. {Mc → kc (CR CL)^(1/2), ML → kL (LR LL)^(1/2)}];
FullSimplify[FullSimplify[(i3/(i ω CL) + i4 (i ω LL/2 + 1/(i ω CL)))/i1 /.
    {i1 → Ans[[2]], i2 → 0, i3 → Ans[[3]], i4 → Ans[[4]]} /. {vo → 1, vi → 1}]]
```

$$(-8\,i\,CR\sqrt{CL\,CR}\;kc\,kL\sqrt{LL\,LR}\;\omega^2 - i\,CL^3\,LL^4\,\omega^6\,(-1 + CR\,\omega\,(-i\,RR + (1 + kL^2)\,LR\,\omega)) +$$
$$4\,LL\,(-3\,i + CR\,\omega\,(3\,RR + i\,(3 + kL^2)\,LR\,\omega + 5\,i\,CL\sqrt{CL\,CR}\;kc\,kL\sqrt{LL\,LR}\;\omega^3)) -$$

```
    i CL LL^2 ω^2 (-19 + CR ω (-19 i RR + (19 + 10 kL^2) LR ω + 12 CL √(CL CR) kc kL √(LL LR) ω^3)) +
    2 CL^2 LL^3 ω^4 (-4 i + CR ω (4 RR + i ((4 + 3 kL^2) LR ω + CL √(CL CR) kc kL √(LL LR) ω^3)))) /
  (2 CL ω (2 CR kc (-2 CL CR kc + 3 √(CL CR) kL √(LL LR)) ω^2 +
      CL LL^2 ω^2 (-1 + CR ω (-i RR + (1 + kL^2) LR ω)) +
      LL (3 + CR ω (3 i RR - (3 + 2 kL^2) LR ω + CL kc (2 CL CR kc - 3 √(CL CR) kL √(LL LR)) ω^3))))

Z21a[CL_, LL_, RR_, LR_, CR_, kc_, kL_, ω_] :=
  (-8 i CR √(CL CR) kc kL √(LL LR) ω^2 - i CL^3 LL^4 ω^6 (-1 + CR ω (-i RR + (1 + kL^2) LR ω)) +
    4 LL (-3 i + CR ω (3 RR + i (3 + kL^2) LR ω + 5 i CL √(CL CR) kc kL √(LL LR) ω^3)) -
    i CL LL^2 ω^2 (-19 + CR ω (-19 i RR + (19 + 10 kL^2) LR ω + 12 CL √(CL CR) kc kL √(LL LR) ω^3)) +
    2 CL^2 LL^3 ω^4 (-4 i + CR ω (4 RR + i ((4 + 3 kL^2) LR ω + CL √(CL CR) kc kL √(LL LR) ω^3)))) /
  (2 CL ω (2 CR kc (-2 CL CR kc + 3 √(CL CR) kL √(LL LR)) ω^2 +
      CL LL^2 ω^2 (-1 + CR ω (-i RR + (1 + kL^2) LR ω)) +
      LL (3 + CR ω (3 i RR - (3 + 2 kL^2) LR ω + CL kc (2 CL CR kc - 3 √(CL CR) kL √(LL LR)) ω^3))))

χ[T1_, T2_, ωs0_, ω_, γ_] := (T1 (ωs0 - ω)) / (1 + T2^2 (ωs0 - ω)^2 + γ^2 1 T1 T2) +
  i T1 / (1 + T2^2 (ωs0 - ω)^2 + γ^2 1 T1 T2)

gL = .000025 ;
gR = .007 ;
kkc = 0.01 * 0;
kkL = 0.005 * 0;
Rv = .001;
T1 = 4 * 10^-9;
T2 = .1 * 10^-9;
γ = 2.8 ;
Show[Plot[Re[
    Sum[(1/qqq^-1 + 1/qqq^-2 + 1/qqq^-3) e^-((f-qqq 150 10^9+6 10^9)^2 / 2 (3000000000)^2), {qqq, 1, 3, .01}]
   ], {f, 50 * 10^9, 750 * 10^9},
  PlotRange → All, AspectRatio → 1 / 4, PlotStyle → Automatic],
 Plot[Re[
    Sum[(1/qqq^-1 + 1/qqq^-2 + 1/qqq^-3) e^-((f-qqq 150 10^9)^2 / 2 (3000000000)^2), {qqq, 1, 3, .01}]
   ], {f, 50 * 10^9, 750 * 10^9}, PlotRange → All,
  AspectRatio → 1 / 4, PlotStyle → {Automatic, Red}]
]

LR[T1_, T2_, ωs0_, ω_, γ_, Dr_, dr_, gr_] :=
 4 π 10^-7 (1 + gr χ[T1, T2, ωs0, ω, γ]) Dr/2 (Log[8 Dr / dr] - 2)
```

Coupled Only

```
gL = 0 × 1000 × 10^-8 ;
gR = 4700 × 10^-8 ;
kkc = 0.255 ;
kkL = 0.065 ;
Rv = .0008;
output = Table[2 Re[
    1 - (Z21a[8.854 × 10^-12, 4 π 10^-7 (1 + gL χ[T1, T2, 300 × 10^9 i, f, γ]), Rv, LR[T1, T2,
          300 × 10^9 i, f, γ, 10 × 10^-9, 0.095 × 10^-9, gR], 1.93 × 10^-10, kkc, kkL, f] /
        Z21a[8.854 × 10^-12, 4 π 10^-7 (1 + gL χ[T1, T2, 295 × 10^9 i, f, γ]), Rv, LR[T1,
          T2, 295 × 10^9 i, f, γ, 10 × 10^-9, 0.095 × 10^-9, gR], 1.93 × 10^-10, kkc, kkL, f])
   ], {f, 255 × 10^9, 700 × 10^9, .5 × 10^9}, {i, 2.0, 1.0, -.025}];
Export[C:/Users/sidabras/Desktop/CoupledOnly.CSV, output, CSV]
Clear[output]
```

With Transmission

```
gL = 1000 × 10^-8;
gR = 4700 × 10^-8 ;
kkc = 0.255;
kkL = 0.065;
Rv = .0008;
output = Table[2 Re[
    1 - (Z21a[8.854 × 10^-12, 4 π 10^-7 (1 + gL χ[T1, T2, 300 × 10^9 i, f, γ]), Rv, LR[T1, T2,
          300 × 10^9 i, f, γ, 10 × 10^-9, 0.095 × 10^-9, gR], 1.93 × 10^-10, kkc, kkL, f] /
        Z21a[8.854 × 10^-12, 4 π 10^-7 (1 + gL χ[T1, T2, 295 × 10^9 i, f, γ]), Rv, LR[T1,
          T2, 295 × 10^9 i, f, γ, 10 × 10^-9, 0.095 × 10^-9, gR], 1.93 × 10^-10, kkc, kkL, f])
   ], {f, 255 × 10^9, 700 × 10^9, .5 × 10^9}, {i, 2.0, 1.0, -.025}];
Export[~/Desktop/WithTransmission.CSV, output, CSV]
Clear[output]
```

Only Transmission

```
gL = 1000 × 10^-8;
gR = 4700 × 10^-8 ;
kkc = 0.255 × 0;
kkL = 0.065 ;
Rv = .0008;
output = Table[2 Re[
    1 - (Z21a[8.854 × 10^-12, 4 π 10^-7 (1 + gL χ[T1, T2, 300 × 10^9 i, f, γ]), Rv, LR[T1, T2,
          300 × 10^9 i, f, γ, 10 × 10^-9, 0.095 × 10^-9, gR], 1.93 × 10^-10, kkc, kkL, f] /
        Z21a[8.854 × 10^-12, 4 π 10^-7 (1 + gL χ[T1, T2, 295 × 10^9 i, f, γ]), Rv, LR[T1,
          T2, 295 × 10^9 i, f, γ, 10 × 10^-9, 0.095 × 10^-9, gR], 1.93 × 10^-10, kkc, kkL, f])
   ], {f, 255 × 10^9, 700 × 10^9, .5 × 10^9}, {i, 2.0, 1.0, -.025}];
Export[~/Desktop/OnlyTransmission.CSV, output, CSV]
```

```
Clear[output]
```

Strong and Weak Coupling Studies

```
gL = 0 × 1000 × 10^-8 ;
gR = 100 × 4700 × 10^-8 ;
kkc = 0.255 ;
kkL = 0.065 ;
Rv = .0008 / 5;
Show[Plot[Re[
    Z21a[8.854 × 10^-12, 4 π 10^-7 (1 + gL χ[T1, T2, 300 × 10^9 ⌗, f, γ]), Rv,
     LR[T1, T2, 300 × 10^9 ⌗, f, γ, 10 × 10^-9, 0.095 × 10^-9, gR], 1.93 × 10^-10, kkc, kkL, f]
   ], {f, 255 × 10^9, 700 × 10^9}, PlotRange → All, PlotPoints → 500, MaxRecursion → 0,
  AspectRatio → 1 / 4, PlotStyle → Red] & /@ {1.7`, 1.45`, 1.2`, 1}, PlotRange → All]
tab1 = Table[Re[
    Z21a[8.854 × 10^-12, 4 π 10^-7 (1 + gL χ[T1, T2, 300 × 10^9 ⌗, f, γ]), Rv,
     LR[T1, T2, 300 × 10^9 ⌗, f, γ, 10 × 10^-9, 0.095 × 10^-9, gR], 1.93 × 10^-10, kkc, kkL, f]
   ], {f, 255 × 10^9, 700 × 10^9, .1 × 10^9}] & /@ Table[i, {i, 0.9, 1.9, .05}];
freq1 = {};
freq2 = {};
freq3 = {};
posout = {};
For[i = 1, i ≤ Length[tab1], i++,
 tlist = Table[i, {i, 0.9, 1.9, .05}];
 pos1 = FindPeaks[-tab1[[i]]];
 freq = Table[f, {f, 255 × 10^9, 700 × 10^9, .1 × 10^9}][[pos1[[1, 1]]]];
 AppendTo[freq1, {tlist[[i]], freq}];
 If[Length[pos1] == 2,
  freq = Table[f, {f, 255 × 10^9, 700 × 10^9, .1 × 10^9}][[pos1[[2, 1]]]];
  AppendTo[freq2, {tlist[[i]], freq}];
 ];
 If[Length[pos1] == 3,
  freq = Table[f, {f, 255 × 10^9, 700 × 10^9, .1 × 10^9}][[pos1[[2, 1]]]];
  AppendTo[freq2, {tlist[[i]], freq}];
  freq = Table[f, {f, 255 × 10^9, 700 × 10^9, .1 × 10^9}][[pos1[[3, 1]]]];
  AppendTo[freq3, {tlist[[i]], freq}];
 ];
 If[Length[pos1] == 4,
  Print[you missed!];
 ];
]
Show[ListPlot[freq1],
 ListPlot[freq2, PlotStyle → Red],
 ListPlot[freq3, PlotStyle → Green], PlotRange → All]


gL = 1 × 10^-8 ;
```

```
gR = 4.7 × 10^-8 ;
kkc = 0.255 ;
kkL = 0.065 ;
Rv = .0008;
Show[Plot[Re[
    Z21a[8.854 × 10^-12, 4 π 10^-7 (1 + gL χ[T1, T2, 300 × 10^9 ⌗, f, γ]), Rv,
     LR[T1, T2, 300 × 10^9 ⌗, f, γ, 10 × 10^-9, 0.095 × 10^-9, gR], 1.93 × 10^-10, kkc, kkL, f]
   ], {f, 255 × 10^9, 700 × 10^9}, PlotRange → All, PlotPoints → 500, MaxRecursion → 0,
  AspectRatio → 1 / 4, PlotStyle → Red] & /@ {1.7`, 1.45`, 1.2`, 1}, PlotRange → All]
tab1 = Table[Re[
     Z21a[8.854 × 10^-12, 4 π 10^-7 (1 + gL χ[T1, T2, 300 × 10^9 ⌗, f, γ]), Rv,
      LR[T1, T2, 300 × 10^9 ⌗, f, γ, 10 × 10^-9, 0.095 × 10^-9, gR], 1.93 × 10^-10, kkc, kkL, f]
    ], {f, 255 × 10^9, 700 × 10^9, .1 × 10^9}] & /@ Table[i, {i, 0.9, 1.9, .005}];
freq5 = {};
freq6 = {};
For[i = 1, i ≤ Length[tab1], i++,
 tlist = Table[i, {i, 0.9, 1.9, .005}];
 pos1 = FindPeaks[-tab1[[i]]];
 freq = Table[f, {f, 255 × 10^9, 700 × 10^9, .1 × 10^9}][[pos1[[1, 1]]]];
 AppendTo[freq5, {tlist[[i]], freq}];
 If[Length[pos1] == 2,
  freq = Table[f, {f, 255 × 10^9, 700 × 10^9, .1 × 10^9}][[pos1[[2, 1]]]];
  AppendTo[freq6, {tlist[[i]], freq}];
 ];
]
ListLinePlot[freq5, PlotStyle → Green]
```

D. Matlab Code

The Matlab code presented in this section was used to determine the g-tensor angular dependence for the data obtained in Chapter 6. The *esfit* function in Easyspin takes an array of collected data and compares it to an array of simulated data based on the parameters in the setup. In this dissertation, a custom function for the *esfit* function was written to speed up the simulations by using the parallel toolkit of Matlab. The *esfit* function returns a set of best solved values ("BestVals") with a calculated error function. Finally, the "BestVals" are plotted as a Resonance Roadmap on top of the collected data, per Fig. 6.5.

Generate setup for *esfit* minimization

```
% spectra from single crystal rotation
% solution requires EasySpin 5.2.25
% Written by: Jason W. Sidabras
%==========================================

clear, clf

% Spin parameters

% Experimental parameters
Exp.mwFreq = 9.48075;
Exp.Range = [312.5 362.4756];
Exp.CrystalSymmetry = 'P1211';
Exp.Harmonic = 0;

Sys.g = [2.1 2.04 1.99];

% Values that are solved and used in this work.
vals = [-9.9905 -104.3957 179.1777 -143.6922 -89.5230 139.4536
    -5.1538 -6.9590 -3.3403]; % 0.0652
 BestVals = struct('coria', vals(1),'corib', vals(2),'coric', vals(3)
     ,...
       'gframea1', vals(4),'gframeb1', vals(5),'gframec1', vals(6),...
       'gframea2', vals(7),'gframeb2', vals(8),'gframec2', vals(9));

%%%%%%%%%%%%%%%%%%%%%%%%%%%%%%%%
% Global Fitting
% Use Corrected data
%%%%%%%%%%%%%%%%%%%%%%%%%%%%%%%%
% spc_cont = [];
% files = dir('corrected_*.DTA');
% for i=1:length(files)
%     [B,spc1,Params] = eprload(files(i).name);
%     spc1r = rescale(real(spc1), 'maxabs');
%     spc_cont = [spc_cont(:); spc1r(:)];
% end
%
% spc_cont = rescale(spc_cont, 'maxabs');
% Use gaussians of known width at measured peaks
spc_cont = csvread('PerfectData.csv');
```

```
39
40 % MolFrame calculated from PCB ID: 4XDC
41 R1=[-0.3308 -0.7701 +0.5454;
42      -0.9376 +0.2027 -0.2825;
43      +0.1071 -0.6049 -0.7891];
44
45 R2=[-0.5948 +0.4557 -0.6622;
46      -0.6664 -0.7403 +0.0891;
47      -0.4496 +0.4943 +0.7440];
48 Sys.MolFrameA=eulang(R1);
49 Sys.MolFrameB=eulang(R2);
50
51 % -CN from Adamska-Venkatesh 10.1039/C4CP05426A
52 AN6 = [-1.3 -1.1 6.2]; N6_AFrame = [0 50 90]*pi/180;
53 Sys = nucspinadd(Sys,'14N',AN6,N6_AFrame);
54
55 Sys.coria = BestVals.coria;
56 Sys.corib = BestVals.corib;
57 Sys.coric = BestVals.coric;
58 Vary.coria = 90;
59 Vary.corib = 90;
60 Vary.coric = 90;
61
62 Sys.gframea1 = BestVals.gframea1;
63 Sys.gframeb1 = BestVals.gframeb1;
64 Sys.gframec1 = BestVals.gframec1;
65 Vary.gframea1 = 90;
66 Vary.gframeb1 = 90;
67 Vary.gframec1 = 90;
68
69 Sys.gframea2 =  BestVals.gframea2;
70 Sys.gframeb2 =  BestVals.gframeb2;
71 Sys.gframec2 =  BestVals.gframec2;
72 Vary.gframea2 = 7.5;
73 Vary.gframeb2 = 7.5;
74 Vary.gframec2 = 7.5;
75
76 % used to check the variation of the angle. Not used in published
       work.
77 Sys.pmang = zeros(1,18)
78 % Vary.pmang = ones(1,18)*3.5
79
80 FitOpt.Scaling = 'lsq';
81 FitOpt.Method = 'swarm';      % for the genetic algorithm
82 FitOpt.PopulationSize = 1000;
83 FitOpt.maxGenerations = 500;
84 FitOpt.nParticles = 50000;
85 FitOpt.RandomStart = 1;
86 FitOpt.nTrials = 100;
87 % FitOpt.maxTime = 90;
88 % [BestVals, BestFit] = esfit('findangles',spc_cont,Sys,Vary,Exp,[],
       FitOpt);
89 esfit('findangles',spc_cont,Sys,Vary,Exp,[],FitOpt)
```

Custom function for *esfit* minimization

```
function y = findangles(Sys,Exp,Opt);
    cori0 = [Sys.coria Sys.corib Sys.coric]*pi/180;          % initial crystal orientation
    nL = [1;0;0];                % rotation axis along lab x axis

    Sys.lwpp = 0.7;

    Sys1 = Sys;
    Sys1.gFrame = [Sys.gframea1 Sys.gframeb1 Sys.gframec1]*pi/180;
    Sys2 = Sys;
    Sys2.gFrame = [Sys.gframea1 Sys.gframeb1 Sys.gframec1]*pi/180 + [Sys.gframea2 Sys.gframeb2 Sys.gframec2]*pi/180;

    Exp.nPoints = 2048;
    % needed for total number of for loops
    files = dir('corrected_*.DTA');
    scalething = 2;
    lenme = length(files)/scalething;
    yq = [];
    cori1 = zeros(3,lenme);
    for i=1:lenme
        rho1 = (i-1)*5*scalething*pi/180 + Sys.pmang(i)*pi/180;
        cori1(:,i) = rotatecrystal(cori0,nL,rho1);
    end
    freq = [9.480429 9.480459 9.480461 9.480404 9.480403 9.480412 9.480417...
        9.480404 9.480395 9.480410 9.480410 9.480423 9.480423 9.480373...
        9.480384 9.480400 9.480402 9.479744 9.480625 9.480697 9.481300...
        9.481302 9.481298 9.481241 9.481993 9.481153 9.481152 9.481158...
        9.481160 9.481145 9.481157 9.481126 9.481129 9.481138 9.481142...
        9.481146];

    freq = freq(1:1*scalething:end);
    parfor i=1:lenme
        PExp1 = struct('mwFreq', freq(i),'Range', Exp.Range,'CrystalSymmetry',Exp.CrystalSymmetry,'Harmonic', 0,'MolFrame', Sys.MolFrameA,'nPoints', Exp.nPoints,'CrystalOrientation', cori1(:,i));
        PExp2 = struct('mwFreq', freq(i),'Range', Exp.Range,'CrystalSymmetry',Exp.CrystalSymmetry,'Harmonic', 0,'MolFrame', Sys.MolFrameB,'nPoints', Exp.nPoints,'CrystalOrientation', cori1(:,i));

        [x,y11] = pepper(Sys1,PExp1,Opt);
        [x,y12] = pepper(Sys2,PExp2,Opt);

        y1r(:,i) = rescale(y11 + y12, 'maxabs');
    end
    for i=1:lenme
```

```
41            yq = [yq(:); y1r(:,i)];
42        end
43        y = yq;
44
45    end
```

Generate the Resonance Roadmap using BestVals from *esfit*

```
% spectra from single crystal rotation
%=========================================
clear, clf
% vals = [-9.8897 -97.2763 177.0524 -121.2711 -106.2582 154.1617
    -3.9470 -4.7960 0.0208]; % 0.0754 RMSD
% vals = [-9.4574 -104.6001 179.2189 -145.3516 -88.3269 142.4581
    -2.6790 -9.0206 -8.6355]; % 0.0729 RMSD
vals = [-9.9905 -104.3957 179.1777 -143.6922 -89.5230 139.4536
    -5.1538 -6.9590 -3.3403]; % 0.0652 RMSD
BestVals = struct('coria', vals(1),'corib', vals(2),'coric', vals(3),
    'gframea1', vals(4),'gframeb1', vals(5),'gframec1', vals(6), '
    gframea2', vals(7),'gframeb2', vals(8),'gframec2', vals(9));

% Experimental parameters
Exp.mwFreq = 9.48075;
Exp.Range = [312.5 362.4756];
Exp.CrystalSymmetry = 'P1211'; % from PDB ID: 4XDC
Exp.Harmonic = 0;


% Spin parameters
Sys.g = [2.1 2.04 1.99];
Sys.lwpp = [0.7];

% Both MolFrames are calculated from PDB ID: 4XDC
R1=[-0.3308 -0.7701 +0.5454;
    -0.9376 +0.2027 -0.2825;
    +0.1071 -0.6049 -0.7891];
R2=[-0.5948 +0.4557 -0.6622;
    -0.6664 -0.7403 +0.0891;
    -0.4496 +0.4943 +0.7440];
Sys.MolFrameA=eulang(R1);
Sys.MolFrameB=eulang(R2);

% Generate orientations in a single rotation plane
nL = [1; 0; 0;];
cori0 = [BestVals.coria BestVals.corib BestVals.coric]*pi/180;
rho1 = [0:5:180]*pi/180;
cori1 = rotatecrystal(cori0,nL,rho1);
Exp.CrystalOrientation = cori1;

% Duplicate Exp split for the 2 assymetric units.
Exp1=Exp;
Exp2=Exp;
Exp1.MolFrame = Sys.MolFrameA;
Exp2.MolFrame = Sys.MolFrameB;

% Duplicate Sys split for the 2 assymetric units.
Sys1 = Sys;
Sys1.gFrame = [BestVals.gframea1 BestVals.gframeb1 BestVals.gframec1
    ]*pi/180;
```

```
Sys2 = Sys;
% Assume gFrameA is related to gFrameB by: gFrameA + delta-angle
Sys2.gFrame = [BestVals.gframea1 BestVals.gframeb1 BestVals.gframec1
    ]*pi/180 + [BestVals.gframea2 BestVals.gframeb2 BestVals.gframec2
    ]*pi/180;

% Simulate roadmape
Opt.Output = 'separate';  % make sure spectra are not added up
Bres1 = resfields(Sys1,Exp1,Opt);
Bres2 = resfields(Sys2,Exp2,Opt);

Y1 = [0:5:180]+2;
X1 = Bres1(1,:);
X2 = Bres1(2,:);
X3 = Bres2(1,:);
X4 = Bres2(2,:);

% plotting
figure1 = figure;

YMatrix1 = [];
files = dir('corrected_*.DTA');
for i=1:length(files)
    [B,spc1,Params] = eprload(files(i).name);
    spc1r = rescale(real(spc1), 'maxabs')*5 + 5*(i-1);
    YMatrix1 = [YMatrix1 spc1r];
    X5 = B/10;
end


% Create axes
axes1 = axes('Parent',figure1,'ColorOrder',[0 0 0]);
hold(axes1,'on');

% Create plot
plot(X1,Y1,'LineWidth',3,'LineStyle','--',...
    'Color',[1 0.08 0.65]);

% Create plot
plot(X2,Y1,'LineWidth',3,'LineStyle','--',...
    'Color',[0.47 0.67 0.19]);

% Create plot
plot(X3,Y1,'LineWidth',3,'LineStyle','--','Color',[0 0 1]);

% Create plot
plot(X4,Y1,'LineWidth',3,'LineStyle','--','Color',[1 0 0]);

% Create multiple lines using matrix input to plot
plot(X5,YMatrix1,'LineWidth',2,'Color',[0 0 0],'Parent',axes1);

% Create xlabel
xlabel({'Magnetic Field [mT]'});
ylabel({'Theta [deg]'});
hold off
% Uncomment the following line to preserve the X-limits of the axes
```

```
100 xlim(axes1,[328 342]);
101 ylim(axes1,[-5 185]);
102 box(axes1,'on');
103 % Set the remaining axes properties
104 set(axes1, 'FontSize', 24, 'GridAlpha', 0.25, 'GridLineStyle', '--',
        'LineStyleOrder', {'-'}, 'LineWidth', 2, 'TickDir', 'out', 'XColor
        ', [0 0 0], 'XGrid', 'on', 'XMinorTick', 'on', 'YColor', [0 0 0],'
        DataAspectRatio',[1 10 1]);
```

E. Three-Pulse ^{14}N ESEEM Data of H_{ox} from CpI.

The following three-pulse ESEEM data was taken by following the fusca-colored resonance roadmap of Fig. 6.5A in Chapter 6. Herein, the τ starts at 200 ns, t_1 starts at 300 ns with 256 24 ns steps, and π-pulse is 80 ns at a microwave power of 7 mW. A total of 16 τ values are taken from 200 ns to 424 ns over an 18 minute collection time per trace.

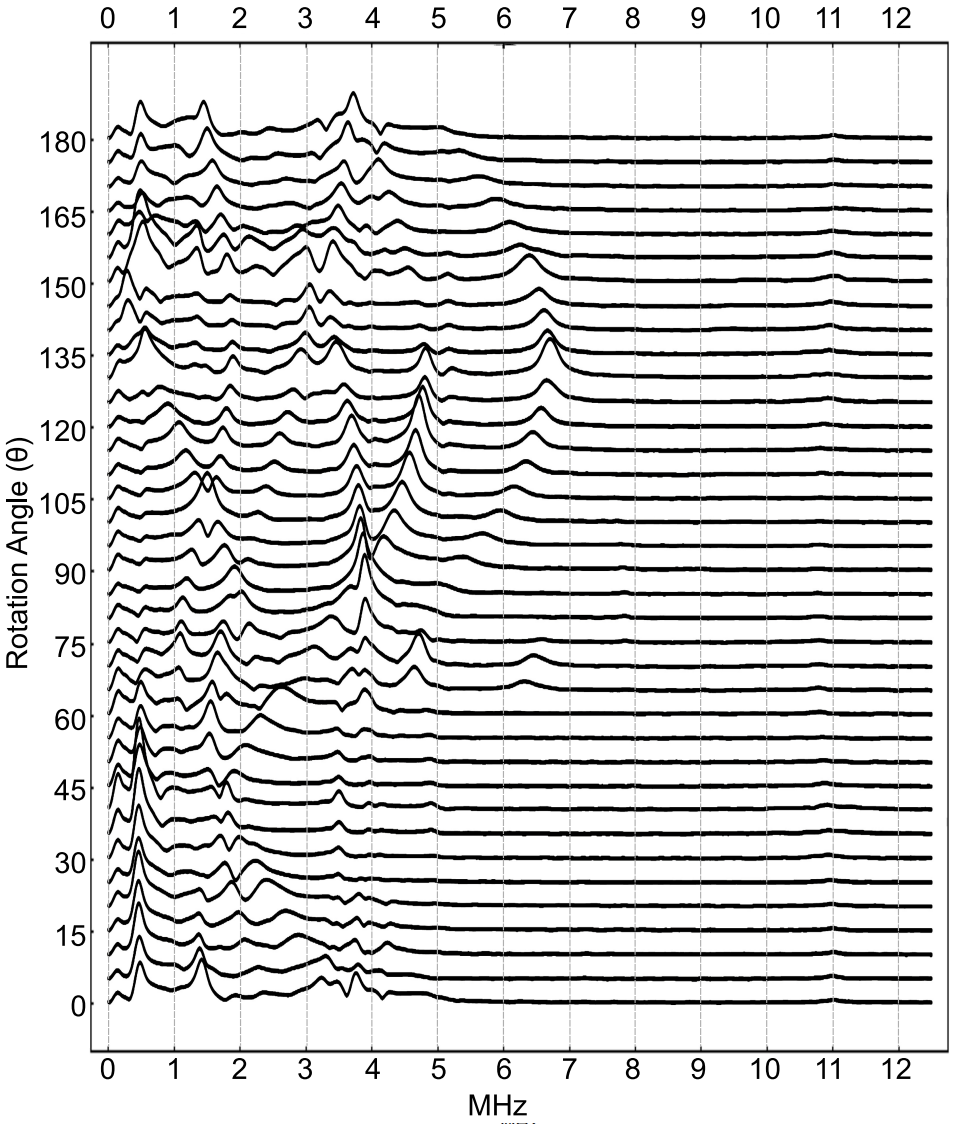

Figure E.1.: Three-pulse ^{14}N ESEEM data from CpI in the H_{ox} stable intermediate.

The data in Fig. E.1 represents the state-of-the-art signal-to-noise ratio for the study of protein single-crystals with volumes less than 3 nl. Further analysis is underway.